The Formation and Evolution of Habitable Worlds

Owen R. Lehmer

A dissertation
submitted in partial fulfillment of the
requirements for the degree of

Doctor of Philosophy

University of Washington

2020

Reading Committee:

David C. Catling, Chair

Victoria Meadows

Jonathan Toner

Program Authorized to Offer Degree:
Earth and Space Sciences & Astrobiology

University of Washington

Abstract

The Formation and Evolution of Habitable Worlds

Owen R. Lehmer

Chair of the Supervisory Committee:
Ph.D. David C. Catling
Earth and Space Sciences

The next generation of ground- and space-based telescopes will probe the atmospheres, and possibly the surfaces, of Earth-sized planets in the habitable zone (HZ). However, observing time will be both expensive and limited making it essential to target only the most promising planet candidates in the hunt for habitable and inhabited worlds. In addition, the measurements of these exoplanets may be noisy and the spectral signals of interest weak, necessitating a robust framework of theoretical and numerical models to guide collection and interpretation of the data, of which the studies presented here are a part.

Conventionally, for a planet or moon to be habitable it must be sufficiently small to not retain abundant nebular gas after formation, but large enough to ensure subsequently outgassed or delivered surface volatiles, such as H_2O, are not rapidly lost to space. In Chapters 2 and 3 we consider these upper and lower bounds by modeling the atmospheric escape of planets and moons around Sun-like stars. We show that rocky planets are unlikely to exist with radii larger than $\sim 1.8\ R_\oplus$ and the smallest habitable planets and habitable zone icy moons may be similar to, or greater in size than Ganymede.

However, size alone does not guarantee exoplanet habitability. Crucially, atmospheric pressure and composition, particularly atmospheric CO_2, must conspire such that surface H_2O does not rapidly evaporate and escape to space or freeze. The Earth has sustained a wide range of atmospheric CO_2 levels over its history, from a few hundred ppmv today to

possibly >70% at 2.7 Ga, which we show from micrometeorite oxidation in Chapter 4. In Chapter 5, from a coupled climate and carbonate-silicate weathering model, we show that similarly broad ranges for atmospheric CO_2 are expected on Earth-like planets in the HZ. Despite this predicted spread in atmospheric CO_2 in the HZ, we show a relationship between CO_2 and incident flux should exist if Earth-like, carbonate-silicate weathering is ubiquitous and so the HZ hypothesis can be tested observationally.

In Chapters 6 and 7 we focus on inhabited exoplanets and model an Earth-like biosphere around other stars, i.e. one dominated by oxygenic photosynthetic organisms. In Chapter 6 we model the optimal pigment absorption profile of photosynthetic organisms and find they may preferentially absorb blue photons around F type stars, red photons around G, K, and early M type stars, and infrared photons around late M type stars. Then in Chapter 7 we show that around the latest M type stars, the lack of high-energy photons available for photosynthesis may limit total biosphere size and detectability.

The chapters in this work provide theoretical and numerical constraints on the properties of habitable and potentially inhabited worlds. We model the plausible size limits on habitable worlds in Chapters 2 and 3, consider CO_2 abundances in habitable atmospheres in Chapters 4 and 5, and predict total biosphere size and absorption properties in Chapters 6 and 7. These findings may aid future detection and characterization of habitable worlds.

TABLE OF CONTENTS

Page

List of Figures . . . iii

List of Tables . . . xiv

Chapter 1: Introduction . . . 1

Chapter 2: Radius limit for rocky planets . . . 4
- 2.1 Abstract . . . 4
- 2.2 Introduction . . . 5
- 2.3 Methods . . . 8
- 2.4 Results . . . 12
- 2.5 Discussion . . . 19

Chapter 3: Icy moons in the habitable zone . . . 20
- 3.1 Abstract . . . 20
- 3.2 Introduction . . . 21
- 3.3 Methods . . . 23
- 3.4 Results . . . 29
- 3.5 Discussion . . . 31
- 3.6 Conclusions . . . 32
- 3.7 Derivation of escape models . . . 33

Chapter 4: Archean carbon dioxide levels from micrometeorite oxidation . . . 43
- 4.1 Abstract . . . 43
- 4.2 Introduction . . . 44
- 4.3 Methods . . . 47
- 4.4 Results . . . 59

4.5 Discussion . . . 63

Chapter 5: Carbon dioxide in the habitable zone . . . 66
5.1 Abstract . . . 66
5.2 Intruduction . . . 67
5.3 Habitable zone climate theory revisited . . . 69
5.4 Methods for numerical carbonate-silicate cycle modeling . . . 75
5.5 Results of habitable zone carbonate-silicate cycling modeling . . . 81
5.6 Discussion . . . 85
5.7 Conclusions . . . 86

Chapter 6: Plant color around other stars . . . 88
6.1 Abstract . . . 88
6.2 Introduction . . . 89
6.3 Methods . . . 90
6.4 Results . . . 94
6.5 Discussion . . . 95
6.6 Conclusion . . . 99
6.7 Supplemental figures . . . 99

Chapter 7: Light-limited biospheres . . . 109
7.1 Abstract . . . 109
7.2 Introduction . . . 110
7.3 Methods . . . 114
7.4 Results . . . 121
7.5 Discussion . . . 123
7.6 Conclusions . . . 127

Chapter 8: Conclusion . . . 129

Bibliography . . . 131

LIST OF FIGURES

Figure Number Page

2.1 Atmospheric loss from planets between 0.5 and 10 Earth masses over 100 Myr with an initial H_2 atmosphere of 3 wt.% at 0.1 AU around a young, Sun-like star. The dashed curve shows the contour of fixed Earth-like density of 5.5 g cm^{-3}. Blue dots representing rocky bodies fall below this line due to compression at high mass. In both plots the model was run with $\tau = 100$ Myr, $R_g = 4157$ J kg^{-1} K^{-1}, $p_{XUV} = 5$ Pa, $F_{XUV} = 55$ W m-2, $\eta = 0.1$, and $\alpha = 0.03$. The planets in plot A had an isothermal atmospheric temperature of $T = 880$ K (corresponding to the effective temperature at 0.1 AU with a Bond albedo of 0), and the temperature was set to $T = 1760$ K in plot B. In both cases, we see a sharp cutoff between rocky and gas-enveloped planets occurring in the 1.2 $R_\oplus$ to 1.6 $R_\oplus$ range. 14

2.2 Ten thousand random parameter combinations were considered using a uniform distribution of the ranges given in Table 2.1 to calculate the cutoff between rocky and gas-enveloped planets. The number of resulting surface radii, R_s, at which the cutoff occurred for each parameter combination is shown in the histogram. The black dot and error bar show the mean cutoff of the distribution at 1.76 ± 0.38 $R_\oplus$ from our model with 2σ uncertainty. The red dot shows the observed $1.62^{+0.67}_{-0.08} R_\oplus$ measurement with 2σ uncertainty from Rogers (2015). 15

2.3 Model run for a 2 $M_\oplus$ planet with isothermal atmospheric temperature set to $T = 880$ K. The planet was assumed to orbit at 0.1 AU around a young, Sun-like star with the initial atmosphere representing 3 wt.%. The model parameters were set as $T = 880$ K, $F_{XUV} = 55$ W m^{-2}, $\alpha = 0.03$, $\eta = 0.1$, $p_{XUV} = 5$ Pa, $R_g = 4157$ J kg^{-1} K^{-1}, and $\tau = 100$ Myr. Plot A shows a snapshot of the planetary radius up to R_{XUV} at times of 0, 6.8, 13.5, 20.3, and 27.1 Myr in the simulation. The blue region shows the relative size of the planetary atmosphere, and the black region shows the size of the rocky core. Plot B shows the remaining atmospheric mass fraction over time. We see that R_{XUV} remains large even after most of the atmosphere has been lost. 16

2.4 The value of R_{XUV}^3 at times $\tau = 0$, 25, 50, 75, and 100 Myr (shown by the blue, orange, green, red, and purple curves, respectively) for planets between 1.75 and 10 $M_\oplus$ around a Sun-like star at 0.1 AU. The model parameters were set to $T = 880$ K, $F_{XUV} = 55$ W m^{-2}, $\alpha = 0.03$, $\eta = 0.1$, $p_{XUV} = 5$ Pa, and $R_g = 4157$ J kg^{-1} K^{-1}. The low mass planets have large R_{XUV}^3 values that cause rapid loss. By ∼6 $M_\oplus$, R_{XUV}^3 has become roughly constant with mass. The approximately flat line at low masses (below ∼2.5 $M_\oplus$ for the purple curve) indicates that, for a given τ, the atmosphere has been entirely lost and R_{XUV}^3 is at the surface of the planet. 17

2.5 The exoplanet data from Fulton et al. (2017) is shown in the black curve (data taken from Fulton et al. (2017) Table 3). Our model predictions are shown by the shaded regions. Using the probability distribution generated in Figure 2.2 the red shaded region shows the probability that a planet is below the rocky planet cutoff, and the blue shaded region shows the probability that a planet is above the rocky planet cutoff. Beyond ∼1.5 $R_\oplus$ planets are unlikely to be rocky while below ∼2 $R_\oplus$ planets are unlikely to be gas-enveloped. Thus, our model predicts a lack of exoplanets with radii between 1.5-2 $R_\oplus$ which is indeed seen in the Fulton et al. (2017) data. Fulton et al. (2017) found that planets below ∼1.8 $R_\oplus$ are likely to be rocky while larger planets are likely to be gas-enveloped, with which our results agree. It should be noted that the vertical axes in this plot are arbitrarily scaled. The important feature, however, is the location of the transition between rocky and gas-enveloped planets and the width of the valley between that transition, which is agnostic of the vertical scaling. 18

3.1 Conceptual visualization of the 1D hydrodynamic escape model. The incoming absorbed stellar flux, given by $1/4(1 - A)F_s$, heats the exomoon surface, for Bond albedo A, and stellar flux F_s. The exomoon will remain in thermal equilibrium by evaporating water vapor, losing mass via hydrodynamic escape, and radiating in the thermal infrared. The thermal infrared radiation is given by σT^4 (σ is the Stefan-Boltzmann constant, T is the surface temperature) in a blackbody approximation. The outward radial flow velocity, u, increases monotonically until it surpasses the isothermal speed of sound, u_c, at the critical radius, r_c, where the gas is still collisional. Beyond the sonic level, u continues to rise and soon surpasses the escape velocity v_{escape}. The exomoon surface is at radius r_s with atmospheric near-surface density ρ_s and outward radial surface velocity u_s. See equation 3.2 for the global energy balance. 23

3.2 For all three plots, the red curve represents the Runaway Flux where the icy moon will be close enough to the star that a runaway greenhouse occurs. The blue curves represent contours of surface water lifetime (plotted in Gyr). The surface temperatures of the moons are shown by the colored background. In plots A and B the surface temperature corresponds to the effective temperature. In plot C the colored background shows the surface temperature, beyond the runaway limit distance, accounting for the effect of the water vapor greenhouse. Comparing the surface temperatures in plot C to those in A and B the water vapor greenhouse is negligible except very close to the runaway limit distance. The rate of hydrodynamic escape depends on both the mass and radius of the exomoon, as such we plot escape velocity vs. distance to incorporate both parameters. Plot A shows the isothermal analytic model (Section 3.3.1) based on equation 3.5. Plot B shows the saturated case where the atmosphere was assumed to follow the Clausius-Clapeyron equation and was saturated from the surface to the critical radius for escape (Section 3.3.2). Plot C shows the isothermal model with the greenhouse effect of water vapor considered (Section 3.3.3). The results shown in all three figures are dependent on the chosen albedo. If the albedo were to be increased from the chosen value of 0.2, the effect would be a linear decrease in absorbed flux. This would shift the runaway limit and the contours of ocean lifetime closer to the host star. For a Ganymede sized moon with a Bond albedo of 0.2 (shown here), 0.4, and 0.8 the runaway limit occurs at 1.05, 0.91, and 0.52 AU respectively. 30

3.3 Contours of surface water lifetime comparing the analytic model given by equation 3.5, shown in red, and the numerical approach where T and u_s are solved for simultaneously, shown in dashed blue contours. Plot A shows the analytic model, which does not consider the greenhouse effect, plotted with the numerical model taking into account the greenhouse effect of water vapor as derived in Section 3.7.3. Both models produce identical results until the runaway limit is approached and the numerical model asymptotes along the limit. Plot B shows the analytic and numerical models as well; however, the greenhouse effect is neglected in the numerical model for this plot. In this case, both methods produce identical results, as expected, for slowly evaporating bodies with surface water lasting more than 1 Gyr. 37

4.1 Single model run for a particle with an entry angle of 45° from zenith run through a 39% CO_2, 61% N_2 atmosphere (50 wt.% CO_2, 50 wt.% N_2). The plots above show: (A) micrometeorite temperature in K, (B) micrometeorite velocity in km s^{-1}, (C) micrometeorite radius in μm, (D) the mass fraction of metallic Fe to oxidized FeO, and (E) the micrometeorite's altitude above the Earth's surface in km. The orange part of each curve indicates the micrometeorite is molten. For plot C, the micrometeorite increases in radius because the oxide layer is growing faster than it is evaporating. The oxidation of high-density Fe to the lower density FeO results in a less dense particle and thus a larger radius. In this simulation, the micrometeorite is molten for 2.6 seconds between 11.9 and 14.5 seconds. The initial radius is 50 μm, the final radius is 54.8 μm, the final Fe fractional mass is 41% (37% by cross-sectional area), and the maximum temperature reached is 2275 K at an altitude of 81.2 km. 54

4.2 Fractional area of unoxidized Fe in simulated sectioned micrometeorites compared to observed modern micrometeorites. The horizontal axis in this plot shows the fractional area of unoxidized Fe in cross-sectioned micrometeorites. The blue histogram shows the simulated unoxidized Fe fractional area from 500 randomly generated micrometeorites entering the modern atmosphere, which were oxidized by O_2, and the orange histogram shows the data inferred from Figure 4 of Genge et al. (2017). The model mean and 2σ confidence interval is shown by the blue dot and error bar, while the mean and 2σ of the data from Genge et al. is shown by the orange dot and error bar. 56

4.3 Comparison of unoxidized Fe area in CO_2-N_2 and CO_2-N_2-O_2 atmospheres with increasing CO_2. The black curve shows the mean model cross-sectional area of unoxidized Fe compared to the total cross-sectional area of the micrometeorite for a CO_2-N_2 atmosphere. It is the same curve as in Figure 4.4. The orange contour shows the same simulated micrometeorites but entering a CO_2-N_2-O_2 atmosphere where the O_2 represents 1% by volume. The addition of 1% O_2 to the atmosphere has little impact on the average Fe fractional area. 60

4.4 Simulated fractional area of unoxidized Fe with increasing atmospheric CO_2. The atmosphere was assumed to be composed of pure N_2 and CO_2. The black curve shows the mean model prediction for the cross-sectional area of unoxidized Fe compared to the total cross-sectional area of the micrometeorite. The simulated micrometeorites were assumed to have spherical, central metal beads so the cross-sectional area of the unoxidized Fe bead is a maximum. The grey shaded area shows the 2σ confidence interval of our model. The orange dot and solid error bar show the mean unoxidized Fe fractional area and 2σ confidence interval from the two Fe-FeO micrometeorites reported by Tomkins et al. (2016). The corresponding uncertainty in atmospheric CO_2 from the Tomkins et al. data is shown by the dashed orange error bars. The Tomkins et al. data point indicates the CO_2 level was at $64^{+36}_{-58}\%$ (2σ). The dashed blue line shows the fraction of modeled micrometeorites that that were fully oxidized in the atmosphere with no remaining metallic Fe. Such particles could lead to magnetite rich micrometeorites and appear in our model once atmospheric CO_2 reaches ~70%. 61

5.1 The relationship between incident flux and atmospheric CO_2 for Earth-like planets regulated by a carbonate-silicate weathering cycle. The horizontal axis shows incident flux, S, normalized to the solar constant ($S_\oplus$) and the corresponding orbital distance in Astronomical Units (AU) above the plot. The vertical axis shows the atmospheric CO_2 partial pressure (pCO_2) in bar. The dotted blue curve labelled '289 K' shows the pCO_2 value required to maintain a 289 K surface temperature for the given incident flux, S. The dotted blue contour labelled '248 K' shows a similar temperature contour but for a 248 K mean surface temperature. The conventional assumption of CO_2 in the HZ stipulates that pCO_2 will adjust to maintain a temperate or even constant surface temperature. Under this assumption, moving the modern Earth (labelled black square) outward in the HZ would have the planet approximately follow the dotted blue 289 K contour. The colored points and gray curves show the modern Earth moving outward in the HZ with a functioning carbonate-silicate weathering cycle, calculated from equation 5.6. We consider two temperature and pCO_2 dependencies for continental weathering in this plot. The strong temperature dependence contour (labelled 'Strong T-dep.'), uses a temperature and pCO_2-dependent weathering factor of $cT_e = 2.3$, which implies a strong temperature feedback on continental weathering compared to the pCO_2 feedback (see equation 5.7). The moderate temperature dependence contour (labelled 'Moderate T-dep.'), uses a temperature and pCO_2-dependent weathering factor of $cT_e = 7.5$. These two values for cT_e result in two different paths the Earth can take as it moves outward in the HZ. The planet color shows the mean surface temperature. Log-linear fits to the colored points of the 'Strong T-dep.' and 'Moderate T-dep.' contours have r^2 values of 0.959 and 0.999, respectively. Thus, even for a strong temperature dependence of continental weathering, our coupled climate and weathering model predicts an approximately log-linear relationship between incident flux and pCO_2 on Earth-like planets in the HZ. 70

5.2 The relative error between our 4^{th}-order polynomial fit and the full 1D radiative-convective climate model. Our polynomial fit is valid between $1.05S_\oplus$ and $0.35S_\oplus$, where $S_\oplus$ is the Solar constant. The polynomial fit is valid for atmospheric CO_2 abundances between 10^{-6} and 10 bar. The surface temperatures predicted by the polynomial fit reproduce the results of the 1D climate model. The maximum error in predicted surface temperature between the polynomial fit and the 1D climate model is $\sim$3%. 80

5.3 The expected distribution of stable, Earth-like exoplanet climates from our habitable zone weathering model. The horizontal axis shows incident flux, S, normalized to the solar constant ($S_\oplus$) and the corresponding orbital distance in Astronomical Units (AU) above the plot. The vertical axis shows the atmospheric CO_2 partial pressure (pCO_2) in bar. Each point represents a climate in steady-state. The black labeled contours show the mean global surface temperature for the given pCO_2 and incident flux. The white region below the 248 K contour is where our model assumption of a liquid ocean is no longer plausible so no planets are shown in that region. Above the 355 K contour Earth-like planets are too hot to retain their liquid oceans for billions of years. Similar to the frozen planets, such hot planets are not considered habitable. The red line shows the line of log-linear best fit through the simulated planets. Modern Earth and Mars are shown by black squares. The blue histogram at the bottom of the figure shows the number of stable planets in each incident flux bin. The color of each simulated planet shows the relative point density in the plot at that location. The color was calculated using a kernel-density estimate with Gaussian kernels and rescaled from 0 to 1. A color value of 0 represents the lowest relative point density, 1 the highest. Our model predicts that atmospheric CO_2 should increase with orbital distance in the HZ. The slope of the best fit line is 3.92 ± 0.24 (95%) with units $-\log_{10}(pCO_2\ [\mathrm{bar}])/[S/S_\oplus]$. 82

5.4 The expected trend of atmospheric CO_2 with incident flux vs the number of observed Earth-like planets. The solid red line shows the mean slope from 10,000 random subsets of the planets in Figure 5.3 with each subset containing the given number of observed planets. The orange and blue error bars show the 1σ and 2σ uncertainties on the expected slope. The solid gray line highlights the zero slope line. The dashed black line shows the point where the expected slope with 2σ confidence is above zero. At the bottom of the figure, the labeled points and error bars show the number of Earth-like exoplanets the next generation of proposed space telescopes are expected to observe (telescope data in Table 5.2). The vertical scaling of the telescope points is arbitrary, only the horizontal position and extent of the error bars is significant. Six Earth-like exoplanets should be observed to be 95% confident that a positive trend between atmospheric CO_2 and decreasing incident flux is detected. . . 83

6.1 Surface flux for a planet with the modern Earth's atmosphere around different stars. The horizontal axis shows photon wavelength in nm, the vertical axis shows the incident photon flux per unit area, per second, per nm. Each colored contour shows the surface photon flux for a different stellar type, as labelled. For each stellar type, the total flux at the top of atmosphere was assumed to be the same as the modern Earth's. 93

6.2 The optimal pigment absorption profile for each stellar type from our pigment optimization model (see Section 6.3). The horizontal axis shows wavelength in nm. The vertical axis shows the predicted absorptance of pigments from the model. Each colored contour represents a different stellar type, as labelled. The shaded gray region and dashed gray line show the absorptance of spinach chloroplasts from Marosvölgyi & van Gorkom (2010), arbitrarily normalized to match the vertical extent of the optimal pigment profile for Earth. The absorption profiles were smoothed by convolution with a 10 nm wide Gaussian function, following Marosvölgyi & van Gorkom (2010). The model predicts the wavelength of peak absorption and the corresponding absorption shape around that peak. The total absorptance of an organism is not reflected by the vertical axis. An organism could produce additional pigments to boost total absorptance, but the optimized absorption peak and shape would remain the same. The position of and shape of chl *a* absorption at ∼680 nm (dashed gray contour) is predicted in both location and shape by the model (green contour). 95

6.3 The optimal pigment absorption profile for each stellar type from Figure 6.2 with stellar spectra shown. The horizontal axis shows wavelength in nm. The vertical axis shows the incident photon flux, taken from Figure 6.1. The predicted pigment absorptance profile for each stellar type is shown in the same color. The vertical scaling of these absorptance profiles from Figure 6.2 is arbitrary as the wavelength of peak absorption and the shape of the absorption peak for each stellar type are the quantities of interest, which are agnostic of the vertical scaling. The dashed gray contour and shading shows the absorption profile of spinach chloroplasts from Marosvölgyi & van Gorkom (2010). The optimal absorption profile predicted by the model shows how pigments should be tuned to avoid atmospheric absorption if they are to maximize growth. Section 6.7.2 has each stellar spectra and corresponding optimal absorption profile shown individually, for clarity. 96

6.4 The optimal pigment absorption profile for different cost parameters around the Sun, a G2V star. The horizontal axis shows wavelength in nm, the vertical axis shows pigment absorptance. Each black curve shows the predicted pigment absorptance for the given cost parameter, C from equation 6.4. The value of C is indicated by the shading where darker shading indicates lower cost. The black shading corresponds to no cost, i.e. $C = 0$, shading approaches white as the cost increases, i.e. $C \to 1$. The predicted absorption profile was smoothed by convolution with a 10 nm wide Gaussian function. This figure recreates the results of Marosvölgyi & van Gorkom (2010), see their Figure 2. 101

6.5 The optimal pigment absorption profile for different cost parameters around an F2V star. See Figure 6.4 for a full description. 102

6.6 The optimal pigment absorption profile for different cost parameters around an K2V star. See Figure 6.4 for a full description. 103

6.7 The optimal pigment absorption profile for different cost parameters around an M1V star. See Figure 6.4 for a full description. 104

6.8 The optimal pigment absorption profile for different cost parameters around an M5V star. See Figure 6.4 for a full description. 105

6.9 The predicted optimal pigment absorption profile for an F2V star from Figure 6.3. 106

6.10 The predicted optimal pigment absorption profile for an G2V star, the Sun, from Figure 6.3. 107

6.11 The predicted optimal pigment absorption profile for an K2V star from Figure 6.3. 107

6.12 The predicted optimal pigment absorption profile for an M1V star from Figure 6.3. 108

6.13 The predicted optimal pigment absorption profile for an M5V star from Figure 6.3. 108

7.1 The inner Solar System in which Mercury, Venus, Earth, Mars, and Jupiter are shown in gray (planet size not to scale). The green circle shows the orbital distance at which the flux of 400-750 nm photons would be insufficient to sustain the current biomass productivity of the Earth's extant terrestrial biosphere. The blue circle shows the orbital distance where the photon flux would no longer be sufficient to sustain the modern Earth's ocean biosphere. The habitable zone for the Sun is shown by the shaded blue band from Kopparapu et al. (2013). As shown by the green and blue circles, with increasing orbital distance, solar energy flux becomes limiting to surface habitability well before it drops below levels required to support Earth's photosynthetic biosphere. Thus, the biospheres of Earth-like planets (with similar albedos and nutrient availability) in the habitable zones of Sun-like stars will not be limited by photon availability. 112

7.2 The optimal pigment absorption wavelength based on stellar temperature following Björn (1976). We assumed an Earth-like planet that orbited its host star at such a distance that the total incident flux is equal to the modern Earth's. 116

7.3 Regions around a star where biomass productivity on an Earth-like planet would be potentially light-limited compared to Earth. Regions are shown for an oxygenic photosynthetic long wavelength limit of $L_\lambda = 750$ nm in plot A, $L_\lambda = 900$ nm in plot B, $L_\lambda = 1100$ nm in plot C, and $L_\lambda = 1500$ nm in plot D. The horizontal axis shows the incident stellar flux, S, normalized by Earth's incident solar flux, $S_\oplus = 1361$ W m−2. The blue shaded regions represent PAR photon fluxes below the terrestrial limit (3.26×10^{20} photons m^{-2} s^{-1}), scaled by the wavelength efficiency factor, ϵ (see text). The red shaded regions represent PAR photon fluxes below the Earth ocean limit (7.35×10^{19} photons m^{-2} s^{-1}), scaled by the wavelength efficiency factor, ϵ. The black lines show the inner and outer limits of the habitable zone from Kopparapu et al. (2013). 122

7.4 The net O_2 produced from organic carbon burial on Earth-like planets. Plots are shown for an oxygenic photosynthetic long wavelength limit of $L_\lambda = 750$ nm in plot A, $L_\lambda = 900$ nm in plot B, $L_\lambda = 1100$ nm in plot C, and $L_\lambda = 1500$ nm in plot D. The horizontal axis shows the incident stellar flux, S, normalized by Earth's incident solar flux, $S_\oplus = 1361$ W m^{-2}. The solid black lines show the inner and outer limits of the habitable zone from Kopparapu et al. (2013). The dashed black line shows the contour where the O_2 flux is equal to the assumed planetary reductant flux that efficiently removes atmospheric O_2 contributed by an organic burial rate of 0.3%. The reductant flux is a kinetically rapid sink for atmospheric O_2, which must be overcome for O_2 to accumulate in the atmosphere (see text). Planets above the dashed contour could build up atmospheric oxygen from oxygenic photosynthesis alone, while planets below the line may be unable to. The dotted black line shows the same as the dashed line, but for a burial rate of 0.23%. 124

LIST OF TABLES

Table Number Page

2.1 The range of values considered for each parameter used to calculate the cutoff between rocky and gas-enveloped worlds for planets orbiting at 0.1 AU around a Sun-like star. The ranges in the table represent a reasonable upper limit for each parameter from the literature. Justification for each range is given in the text. 13

5.1 Parameters are dimensionless unless otherwise described. The fourth column shows how scaling parameters impact the model, where T_s is the surface temperature in K and Q is the internal heat of the planet relative to the modern Earth (see equation 5.9 for Q). The justification for each parameter range can be found in Krissansen-Totton et al. (2018a) unless otherwise noted. *The justification for this parameter is given in Section 5.4. 76

5.2 The number of expected Earth-like exoplanets observed by each platform from the HabEx (2019) and LUVOIR (2019) final reports. 85

7.1 Wavelength limits for OP and the corresponding photon energy scaling parameter. 120

ACKNOWLEDGMENTS

Above all else, I would like to thank my advisor, David Catling. None of the work presented here would have been possible without his insight, guidance, humor, and support. In particular, I would like to thank David for reading and revising the many, many manuscript drafts I've sent him over the years. When you read Chapter 3, the first academic paper I wrote with David, know that I sent him 27 drafts of that manuscript and he provided detailed comments and suggestions on each one. I can only imagine the number of hand cramps and empty red pens from that experience.

I would also like to thank the other members of my dissertation committee, Jonathan Toner, Victoria Meadows, and Roger Buick. Your guidance and support have been invaluable throughout this process. I'm especially grateful to Roger, who opened his lab group to me while David was on sabbatical. In the years since, I have continued to swing by Roger's office to pester him with questions and he has always been approachable, kind, funny, and incredibly knowledgeable.

One of the most rewarding and enjoyable experiences at the University of Washington was my membership in the Astrobiology Program. The program fostered collaborations between disciplines and spawned new ideas that would have been impossible without the open, inquisitive culture of the program. I would like to thank Vikki Meadows (the program's director), the Astrobiology Program steering committee, and my fellow Astrobiology students for making it such a wonderful experience. The research presented here has been strongly influenced by the ideas and work of the Astrobiology Program members.

To the many other students and faculty I've interacted with over the past five years, thank you for your support and companionship. A huge "thank you" to my office-mate, Lauren, who helped me with homework, lab work, administrative issues, and staying sane and upbeat while working in our windowless office. In addition, thank you to all of my friends in Seattle and around the world for encouraging me in this process.

Finally, I would like to thank my family. My parents, Matt and Mary, for their numerous support packages, uplifting phone calls, and visits. My brothers, Franklin, Elliot, and Charlie who were always available for lighthearted virtual hangouts and games. And Hana, whose unwavering support and infectious positivity have made a world of difference over the past five years.

DEDICATION

goes best with coffee

Chapter 1

INTRODUCTION

One of the earliest written stories of life beyond Earth, complete with exotic creatures on Earth's moon, was put down by *Lucian of Somosata* in ∼175 CE (Grewell, 2001). Since then, life beyond Earth has largely remained the realm of science fiction. However, in the near future, we may step beyond science fiction and find signs of life elsewhere in the Universe. In March, 2021 the continually soon-to-launch James Webb Space Telescope (JWST) will, barring further delays from the global pandemic, launch and begin characterizing the atmospheres of potentially habitable planets around cool stars. In the mid 2020s, extremely large ground based telescopes and WFIRST will extend our understanding of habitability. Future missions, such as HabEx and LUVOIR, will provide unprecedented constraints on planetary habitability and may directly image Earth-like planets in the habitable zones (HZ) of Sun-like stars, should they be built (see Schwieterman et al. (2018) for a summary of current and future observing platforms and their capabilities).

Measuring biosignatures with these telescopes could take tens or even hundreds of hours of telescope time per target (e.g. Meadows et al., 2018a). Thus, to avoid wasting valuable observing time, it is critical to determine which of the more than 4,000 currently known exoplanets (plus exoplanets soon to be found) to target in the search for habitable worlds and alien life (see `https://exoplanetarchive.ipac.caltech.edu/docs/counts_detail.html` for the number of currently known exoplanets). To that end, this work models the formation and evolution of habitable worlds and possible spectral features that future telescopes might observe. The six research chapters (Chapters 2, 3, 4, 5, 6, and 7) are each standalone studies to aid in the target selection and characterization of habitable worlds.

In Chapters 2 and 3, the size limits of habitable, terrestrial planets and icy moons are considered. The majority of currently known exoplanets were detected via the transit method (e.g. Batalha, 2014), thus, planetary radius is often one of the few properties determined. It is ideal, then, to approximately constrain planetary habitability from a planet's radius. Chapter 2 shows that rocky planets, a possible prerequisite for habitability, are unlikely to form with radii larger than $\sim 1.8\ R_\oplus$ due to rapid photoevaporation of their protoatmospheres around young stars. From similar atmospheric escape models, Chapter 3 shows that icy moons of Ganymede's size could remain habitable around a Sun-like star for billions of years in the HZ. However, smaller moons of Europa's size are likely too small to hold onto surface water, which will be rapidly lost to space from the small bodies. As a first-order constraint on habitable world target selection, future missions might consider exoplanets with radii between these limits.

We move from the size limitations discussed in Chapters 2 and 3 to the composition of habitable, planetary atmospheres in Chapters 4 and 5. In particular, we focus on atmospheric CO_2. Atmospheric CO_2 plays a critical role in regulating the climate and ocean pH of Earth-like planets (e.g. Krissansen-Totton et al., 2018a), both of which are important to constrain life's origin and evolution on Earth (e.g. Kadoya et al., 2020). In Chapter 4, to constrain atmospheric CO_2 on the Archean Earth (4.0 to 2.5 billion years ago), we model the atmospheric entry and oxidation of iron-rich micrometeorites. Comparing our model results to Archean micrometeorite data we show that at 2.7 Ga the Archean Earth likely had abundant CO_2 in its atmosphere, orders of magnitude more than the few hundred ppmv in the modern Earth's atmosphere.

In Chapter 5, we broaden our focus and consider atmospheric CO_2 on Earth-like planets in the HZ generally. Using a coupled climate and carbonate-silicate weathering model, we show that, if such a silicate weathering feedback is ubiquitous on habitable planets, then a log-linear relationship between atmospheric CO_2 and incident flux may be observable in the HZ. However, if plausible variations in habitable planets are taken into account, abundant scatter is introduced in this relationship between incident flux and atmospheric CO_2. Despite this scatter, a sufficiently large telescope, such as LUVOIR, could characterize enough Earth-like planets to recover our predicted relationship between incident flux and atmospheric CO_2, testing the validity of the HZ hypothesis (e.g. Bean et al., 2017; Turbet, 2019).

This work finishes with studies of photosynthetic organisms in Chapters 6 and 7. Oxygenic photosynthesis is responsible for most of the primary biomass production on the modern Earth (e.g. Field et al., 1998) and may be similarly important on inhabited exoplanets. In Chapter 6, using a numerical model that predicts absorption profiles of extant photosynthetic organisms based on incident photon flux, we predict the absorption profile of similar organisms around other stars. We find that both stellar type and atmospheric composition play an important role in shaping the likely absorption features of photosynthetic organisms. Our results show that around F type stars photosynthetic organisms may preferentially absorb blue photons, while around G, K, and early M type stars they may absorb red photons (or just beyond). For the coolest M type stars, infrared photons are absorbed.

We further investigate photosynthetic biospheres around the coolest M type stars in Chapter 7. Considering the total photon flux available to photosynthetic organisms, we show that biospheres around cool stars, such as TRAPPIST-1, may be growth-limited due to a paucity of high-energy photons. The majority of photons emitted by these cool stars are in the infrared, which could provide sufficient energy to maintain habitability but may be incapable of driving an Earth-like amount of oxygenic photosynthesis. These light-limited biospheres may have smaller total biomass productivity compared to the modern Earth and thus display smaller biosignatures.

Together, this work provides insight into some of the properties habitable worlds may exhibit. Guided by the models in Chapters 2 though 7 and numerous other studies considering habitable worlds, future missions will be prepared to target the most promising candidate planets in the search for habitable worlds and alien life. At the start of each research Chapter, a status is presented indicating whether the chapter has been published, is in review, or is currently being prepared for publication.

Chapter 2

RADIUS LIMIT FOR ROCKY PLANETS

Status

This work was published under the title *Rocky Worlds Limited to ∼1.8 Earth Radii by Atmospheric Escape during a Star's Extreme UV Saturation* by **Owen R. Lehmer and David C. Catling**. It was published in *The Astrophysical Journal* in **2017**. See the reference Lehmer & Catling (2017).

2.1 Abstract

Recent observations and analysis of low mass ($<10\ M_\oplus$) exoplanets have found that rocky planets only have radii up to 1.5-2 $R_\oplus$. Two general hypotheses exist for the cause of the dichotomy between rocky and gas-enveloped planets (or possible water worlds): either low mass planets do not necessarily form thick atmospheres of a few wt. %, or the thick atmospheres on these planets easily escape driven by x-ray and extreme ultraviolet (XUV) emissions from young parent stars. Here we show that a cutoff between rocky and gas-enveloped planets due to hydrodynamic escape is most likely to occur at a mean radius of 1.76 ± 0.38 (2σ) $R_\oplus$ around Sun-like stars. We examine the limit in rocky planet radii predicted by hydrodynamic escape across a wide range of possible model inputs using 10,000 parameter combinations drawn randomly from plausible parameter ranges. We find a cutoff between rocky and gas-enveloped planets that agrees with the observed cutoff. The large cross-section available for XUV absorption in the extremely distended primitive atmospheres of low mass planets results in complete loss of atmospheres during the ∼100 Myr phase of stellar XUV saturation. In contrast, more massive planets have less distended atmospheres and less escape, and so retain thick atmospheres through XUV saturation and then indef-

initely as the XUV and escape fluxes drop over time. The agreement between our model and exoplanet data leads us to conclude that hydrodynamic escape plausibly explains the observed upper limit on rocky planet size and few planets (a "valley") in the 1.5-2 $R_\oplus$ range.

2.2 Introduction

In the past decade, thousands of exoplanet candidates and diverse planetary systems have been found (e.g. Hatzes, 2016). The variety of characteristics observed among these planets has raised many questions about planetary formation and evolution. Of particular interest is how low-mass (defined here as less than $\sim$10 $M_\oplus$), rocky planets form and evolve given their potential to support habitable conditions (e.g. Forget & Leconte, 2014). Central to this question is whether a rocky planet will accrete and retain a massive H_2/He protoatmosphere that represents a non-negligible fraction of the total planetary mass, which may produce uninhabitable surface temperatures, or if such an atmosphere will be lost. These H_2/He protoatmospheres can form on even the smallest planets because once a protoplanet reaches $\sim$0.1 $M_\oplus$ it can accrete H_2/He directly from the stellar disk (Hayashi et al., 1979; Ikoma & Hori, 2012; Lammer et al., 2011).

If low mass planets form after the protoplanetary nebula dissipates they will not accrete H_2/He protoatmospheres (e.g. Massol et al., 2016). However, from planetary formation models, 1-10 $M_\oplus$ planets with periods <100 days may have formed with longer periods when the stellar disk was still present and migrated to their observed locations through interactions with the disk (e.g. Cossou et al., 2013; Raymond & Cossou, 2014). The planets considered in this study have short periods (less than 100 days) and thus may have formed before the stellar disk dissipated. Theoretical calculations suggest that such planets may form with H_2/He protoatmospheres of 1-10 wt. % (Bodenheimer & Lissauer, 2014; Ikoma & Hori, 2012; Inamdar & Schlichting, 2015). Indeed, a number of low mass exoplanets with thick atmospheres have been observed indicating there is likely no barrier for such protoatmospheres to form on low mass planets (Cubillos et al., 2016; Lissauer et al., 2013; Masuda, 2014).

Observations and subsequent analysis of have shown that rocky planets, without thick protoatmospheres, are only found up to 1.5-2 $R_\oplus$ in size (Dressing & Charbonneau, 2015; Marcy et al., 2014; Rogers, 2015; Weiss & Marcy, 2014) with some recent observations indicating that rocky planets can reach $\sim$1.9 $R_\oplus$ in size (Buchhave et al., 2016; Demory et al., 2016). If most close-orbiting planets indeed form with thick protoatmospheres then the least massive planets must have lost their captured H_2 and He (see Lopez & Rice (2016) for a discussion of atmospheric formation vs. atmospheric loss). Thermally driven atmospheric loss in the hydrodynamic escape regime is thought to be able to effectively strip the protoatmospheres from planets up to 5-10 $M_\oplus$ (e.g. Chen & Rogers, 2016; Howe & Burrows, 2015; Jin et al., 2014; Lopez & Fortney, 2013; Lopez et al., 2012; Lopez & Rice, 2016; Owen & Jackson, 2012; Owen & Wu, 2016; Owen & Morton, 2016; Owen & Wu, 2013; Wolfgang & Lopez, 2015).

The rapid loss of the protoatmosphere via hydrodynamic escape is driven by the XUV emissions (where XUV is X-ray plus extreme UV) from the host star, which heats the upper atmosphere of the planet. For young, Sun-like stars, this XUV flux can be orders of magnitude larger than the modern Sun (Johnstone et al., 2015; Lammer et al., 2014). A saturated XUV flux can last for $\sim$100 Myr (Jackson et al., 2012; Lammer et al., 2012; Ribas et al., 2005). The XUV-driven hydrodynamic escape of a protoatmosphere will occur largely during this saturation time after which the XUV flux and XUV driven hydrodynamic escape decrease exponentially. While Sun-like stars can erode atmospheres from closely orbiting planets (0.1 AU for this model), the modern Earth is orbiting at a sufficient distance that its hydrogen-poor atmosphere is not subjected to hydrodynamic escape (see Catling & Kasting (2017, p. 175) for a discussion of the topic). However, evaporation of Earth-like planets may occur at orbital distances similar to the modern Earth for some low mass planets via water vapor photolysis and subsequent hydrogen escape (e.g. Kasting et al., 2015; Luger & Barnes, 2015).

Several recent numerical studies on XUV-driven hydrodynamic escape from low mass planets have results that overlap but differ from each other when simulating the loss of protoatmospheres. Lopez & Fortney (2013), using the model of Lopez et al. (2012), showed that planets less than ∼4 $R_\oplus$ could easily lose their atmospheres from hydrodynamic escape, and follow-on work by Lopez & Fortney (2014) suggested that 1.75 $R_\oplus$ was a likely upper size limit for rocky bodies. Similarly, Wolfgang & Lopez (2015) applied the model from Lopez et al. (2012) to data from the Kepler mission and found planets with radii above 2 $R_\oplus$ should have atmospheres of at least ∼1 wt.% while planets below 2 $R_\oplus$ should have atmospheres less than 1 wt.%. A parameter study of Howe & Burrows (2015) for XUV-driven hydrodynamic escape found that a cutoff between rocky and gas-enveloped planets occurs between 2 and 10 $M_\oplus$ depending on the model orbital distance, which corresponds to a cutoff of 1.26 to 2.16 $R_\oplus$ for an Earth-like density of 5.5 g cm^{-3}.

Other studies have discussed an apparent "valley" in the distribution of exoplanet sizes. Owen & Wu (2013) showed that XUV-driven hydrodynamic escape from low mass planets results in rocky planets less than 1.5 $R_\oplus$, gas-enveloped planets above 2.5 $R_\oplus$, and a lack of planets with intermediate radii. Jin et al. (2014) studied several hydrodynamic escape models and found a valley between 1 and 2.5 $R_\oplus$ depending on the orbital distance chosen for their model, below which planets are rocky and above which planets have thick atmospheres, typically of at least a few wt. %. Similarly, the XUV-driven hydrodynamic escape model of Chen & Rogers (2016) found a valley in the range of 1-2 $R_\oplus$.

In this study, using an XUV-driven hydrodynamic escape model in which only the atmospheric mass changes over time, we look at the likelihood that XUV-driven hydrodynamic escape can reproduce the observed $1.62^{+0.67}_{-0.08}$ $R_\oplus$ cutoff from Rogers (2015) and seek to examine the dominant factors that lie behind the cutoff. We do so by running our model with parameter ranges that describe the most escape-vulnerable planets studied by Rogers (2015). From these escape-vulnerable planets, our model provides an upper limit on the atmospheric loss rate and thus the radii of planets that can lose their entire protoatmospheres and become rocky.

We calculate the cutoff between rocky and gas-enveloped planets with 10,000 different model parameter combinations. We consider only Sun-like stars in this work because the planets used in the study of Rogers (2015) all orbited stars with effective temperatures between 4700 K and 6300 K. The atmospheric loss from XUV-driven hydrodynamic escape around M dwarfs has been considered elsewhere (e.g. Luger et al., 2015; Tian, 2009) and we do not address such systems here.

2.3 Methods

During hydrodynamic escape, a high altitude portion of an atmosphere is heated by XUV flux and flows hydrodynamically outward (Johnstone et al., 2015; Mordasini et al., 2012). However, for thick protoatmospheres that likely represent at least a few wt.% of a planet (Bodenheimer & Lissauer, 2014; Ikoma & Hori, 2012; Inamdar & Schlichting, 2015), the bulk of the lower atmosphere will approximately remain in hydrostatic equilibrium. As such, we assume for this model that above the XUV absorption level, R_{XUV}, where the optical depth for the XUV is near unity, the atmosphere is in the hydrodynamic regime and below R_{XUV} the atmosphere is in approximate hydrostatic equilibrium.

The energy-limited rate of XUV-driven hydrodynamic escape from a planet can be approximated by a first-order equation, as follows

$$\frac{dM}{dt} = \frac{\eta \pi F_{XUV} R_{XUV}^3}{G M_p} \tag{2.1}$$

where dM/dt is the rate of hydrodynamic escape in kg s^{-1} (Watson et al., 1981). The parameter η in equation 2.1 is an efficiency factor that is typically taken to be $0.1 < \eta < 0.6$ (e.g. Bolmont et al., 2017; Koskinen et al., 2014; Lammer et al., 2013; Owen & Wu, 2013). The XUV flux incident on the planet in W m^{-2} is given by F_{XUV}, R_{XUV} is the radial distance from the planetary center at which the optical depth for broadband XUV radiation is unity, G is the gravitational constant, and M_p is the mass of the planet. For the range of F_{XUV} values considered in this study, the rate of hydrodynamic escape may border on the recombination-limited regime described by Murray-Clay et al. (2009). In the recombination-limited regime, for large XUV fluxes (greater than ~10 W m^{-2}), the protoatmospheres could lose energy via recombination of ionized gas slowing the hydrodynamic loss rate. In this recombination-limited regime $dM/dt \propto F_{XUV}^{1/2}$, while $dM/dt \propto F_{XUV}$ in the energy-limited regime. However, on small planets the rate of hydrodynamic escape is dominated by the R_{XUV} term in equation 2.1 so the difference between the recombination-limited and energy-limited regimes is likely small. As such, we consider only the energy-limited case in this study. To find dM/dt we need only determine the XUV flux and R_{XUV}.

The XUV flux from young FGK stars is largest for the first 100 ± 20 Myr after formation (Jackson et al., 2012; Lammer et al., 2012; Ribas et al., 2005). Emissions of XUV are saturated during that time and remain approximately constant. Afterwards, the XUV flux diminishes exponentially and the hydrodynamic loss rate of a planetary atmosphere drops with it. During the saturated regime, for a Sun-like star, the XUV flux can reach ~0.1% of the bolometric luminosity (Jackson et al., 2012; Lammer et al., 2014). Given the uncertainty of stellar evolution, a Sun-like star could generate 43-172 W m^{-2} in the XUV at 0.1 AU following Pizzolato et al. (2003). For comparison, at 1 AU the present Earth receives an XUV flux of only ~5 mW m^{-2} (Lammer et al., 2014).

Around Sun-like stars, the protoatmospheres of some low mass planets orbiting interior to 0.1 AU will likely extend beyond the planet's Roche lobe and be rapidly lost (Ginzburg & Sari, 2017; Owen & Wu, 2013). Not only would the atmosphere be rapidly removed from the high flux and gravitational effects of the host star interior to 0.1 AU, but the rocky core could begin to evaporate as well (Perez-Becker & Chiang, 2013). The planets used in the Rogers (2015) work fall mostly outside this limit with only four planets, Kepler-10b, Kepler-21b, Kepler-98b, and Kepler-407b, receiving a flux greater than the 0.1 AU equivalent around a Sun-like star. Kepler-10b, Kepler-21b, and Kepler-407b are less than ~1.6 in radii. In contrast, Kepler-98b has a radius of $1.99 \pm 0.22 R_{\oplus}$, with a density of 2.18 ± 1.21 g cm^{-3} so it is not a rocky planet (Marcy et al., 2014). Of the three rocky planets none exceed the radius limit described by Rogers (2015). Thus, we use an orbital distance of 0.1 AU as the inner bound for rocky planets in our model.

We assume that absorption of XUV occurs downward through an upper atmosphere and is fully absorbed by the base of a thermosphere. The problem of finding R_{XUV} then becomes a matter of finding the radial distance to the base of the thermosphere. For a neutral H_2 atmospheric column, the broadband XUV flux is typically absorbed within a column of density 10^{26} m^{-2} (e.g. Cecchi-Pestellini et al., 2006; Ercolano et al., 2009; Glassgold et al., 2004; Owen & Jackson, 2012). For an Earth mass planet, gravity assumed constant, this corresponds to a pressure at the base of the thermosphere of $p_{XUV} = 3.3$ Pa and $p_{XUV} = 7.1$ Pa for a planet of 10 $M_{\oplus}$. However, on the modern Earth the base of the thermosphere can occur at pressures as low as $p_{XUV} = 0.1$ Pa (Catling & Kasting, 2017, p. 4) so we will consider a range of pressures from $0.1 \leq p_{XUV} \leq 10$ Pa. Once p_{XUV} is known, it remains fairly constant over a planet's lifetime even if the surface pressure changes by orders of magnitude (Erkaev et al., 2013). Thus, as rocky planets lose their substantial protoatmospheres, p_{XUV} does not change but rather moves closer to the planetary surface as surface pressure drops.

The protoatmosphere of a young planet will be in approximate hydrostatic equilibrium from the surface to the base of the thermosphere. The radial distance to the base of the thermosphere, R_{XUV}, can then be found via the hydrostatic equation, which can be written as

$$-R_g T \frac{1}{p} dp = g_s \left(\frac{R_s}{R} \right)^2 dR \tag{2.2}$$

for specific gas constant R_g, pressure p, isothermal temperature T, surface radius of the rocky core R_s, and surface gravity g_s. In equation 2.2 we have approximated the gravity term of the hydrostatic equation as $g(R) = g_s(R_s/R)^2$ (see Catling & Kasting (2017, p. 11) for a discussion of the topic). In this study, we assume all rocky planets form with an Earth-like structure and relate mass to radius via

$$R_s = 1.3 M_p^{0.27} \tag{2.3}$$

which provides a good approximation for the rocky cores of planets in our model. Equation 2.3 is derived from the relation $R_s \propto M_p^{0.27}$ given by Zeng et al. (2016). To make this relationship hold when using SI units for the mass (5.9742×10^{24} kg) and radius (6.371×10^{6} m) of the Earth a scalar value of 1.3 must be used, as seen in equation 2.3. Integrating equation 2.2 from the surface to p_{XUV} and solving for R we find

$$R_{XUV} = \frac{R_s^2}{H \ln(p_{XUV}/p_s) + R_s} \tag{2.4}$$

with scale height $H = R_g T/g_s$. Surface pressure, p_s, can be defined as

$$p_s(M) = \frac{g_s(\alpha M_p - M)}{4\pi R_s^2} \tag{2.5}$$

where α is the initial protoatmospheric mass fraction, and M is the integrated mass loss from equation 2.1. We assume an initial α for our model, leaving only the scale height H unknown.

The atmospheric scale height depends on the temperature profile and atmospheric composition. We are interested in the upper limit on rocky planet radii so, as an upper limit, the atmospheric composition was assumed to be pure H_2 with $R_g = 4157$ J kg^{-1} K^{-1}. This provides an upper bound on H and thus on the loss rate and the radii limit. The atmospheres of Uranus and Neptune have specific gas constants of $R_g \approx 3600$ J kg^{-1} K^{-1} (Lunine, 1993) and may represent a composition similar to the protoatmospheres we are modeling so we consider the range $3600 \leq R_g \leq 4157$ J kg^{-1} K^{-1}. To calculate the scale height with R_g we use an isothermal atmospheric temperature.

For the protoatmospheres in this study, that represent up to a few wt. % of the total planetary mass, a reasonable upper limit on surface temperature, and thus the isothermal upper atmospheric temperature, is ∼3000 K based on temperature profiles from more complex calculations (Jin et al., 2014; Mordasini et al., 2012). In addition, on larger planets with H_2 dominated atmospheres, cooling from gas expansion and Lyman-alpha radiation in the upper atmosphere likely result in temperatures of ∼3000 K in the thermosphere (Murray-Clay et al., 2009). We expect similar processes to occur in the protoatmospheres of low mass planets. With 3000 K being a reasonable upper limit at both the planetary surface and the base of the thermosphere, we set the upper limit for the isothermal atmospheric temperature in our model to 3000 K. For a lower bound we set the isothermal atmospheric temperature equal to the effective temperature at 0.1 AU. For a Bond albedo of 0 this distance corresponds to an effective temperature of 880 K around a Sun-like star.

The atmospheric loss rate is easily calculated from equation 2.1. First, an orbital distance is chosen (0.1 AU in this model) and a planetary mass. To calculate the atmospheric loss rate and thus the cutoff between rocky and gas-enveloped planets, 7 additional model parameters must be specified. These parameters are: isothermal atmospheric temperature, T; XUV flux at the given orbital distance, F_{XUV}; escape efficiency, η; initial atmospheric mass fraction, α; pressure at the base of the thermosphere, p_{XUV}; specific gas constant of the atmosphere, R_g; and XUV saturation time, τ. We consider 10,000 combinations of these 7 parameters, which were selected randomly from a uniform distribution from the values in Table 2.1. The result for the radius cut-off and its uncertainty is insensitive to the exact number of parameter combinations, whether 10,000 or 20,000 or 5,000 based on sensitivity tests. For each parameter combination, we calculate the cutoff between rocky and gas-enveloped planets using a time step of 10,000 years, which runs quickly and is as accurate as smaller step sizes. Figures 2.1A and 2.1B show an example of a model run where the cutoff occurs in the 1.2-1.6 $R_\oplus$ range for the given parameters.

2.4 Results

We examined the protoatmospheric loss from planets between 0.5 and 10 $M_\oplus$. The results can be seen in Figure 2.2, which shows the counts of the calculated cutoff radii, R_s, between rocky and gas-enveloped planets for the 10,000 random parameter combinations. The red dot shows the observed cutoff radius for rocky planets from Rogers (2015) with a 2σ uncertainty. The black dot and error bar shows the model mean and 2σ uncertainty. The distribution in Figure 2.2 aligns well with the observed rocky planet limit with both the mean and mode falling within the 95% confidence interval of the observed rocky planet limit. While the mean of our model is 1.76 ± 0.38 (2σ) $R_\oplus$, the mode falls closer to ∼1.9 $R_\oplus$, which is where

Parameter	Range	Units
Initial atmospheric temperature	$880 \leq T \leq 3000$	K
XUV flux	$43 \leq F_{XUV} \leq 172$	W m^{-2}
Initial atmospheric mass fraction	$0.01 \leq \alpha \leq 0.1$	Dimensionless
Escape efficiency	$0.1 \leq \eta \leq 0.6$	Dimensionless
Pressure at the base of the thermosphere	$0.1 \leq p_{XUV} \leq 10$	Pa
Specific gas constant	$3600 \leq R_g \leq 4157$	J kg^{-1} K^{-1}
XUV saturation time	$80 \leq \tau \leq 120$	Myr

Table 2.1: The range of values considered for each parameter used to calculate the cutoff between rocky and gas-enveloped worlds for planets orbiting at 0.1 AU around a Sun-like star. The ranges in the table represent a reasonable upper limit for each parameter from the literature. Justification for each range is given in the text.

the largest rocky planets have been found. Our model predicts that beyond ~1.9 $R_\oplus$, there is a fairly sharp drop off in the likelihood that hydrodynamic escape can erode a planet. This agrees with recent observations that the largest rocky planets are found up to ~1.9 $R_\oplus$ (Buchhave et al., 2016; Demory et al., 2016). The largest cutoffs predicted in our model are due to parameter combinations with high isothermal atmospheric temperatures and large specific gas constants. In addition to planetary mass, these two parameters control the R_{XUV} term in equation 2.1, which dominates the loss rate, as discussed below.

Upon close examination, we find that a key aspect of the cutoff between gas-enveloped and rocky planets is that the atmosphere remains very distended, up to several planetary radii in size, and available for XUV absorption on low mass bodies even as atmospheric mass is lost. That protoatmospheres remain puffy, even at low mass, is a result of the logarithmic term in equation 2.4 generating large values for R_{XUV} until the atmosphere is completely removed. This is seen in Figure 2.3 where we show R_{XUV} of a 2 $M_\oplus$ planet over time. Even when less than 20% of the original protoatmosphere remains at 20.3 Myr, the radius R_{XUV} is roughly twice the radius of the core. The large radius is caused by the lower gravity on low mass planets coupled to high temperatures (up to several thousand Kelvin), and light atmospheric compositions of H_2/He that lead to substantial scale heights and R_{XUV} values

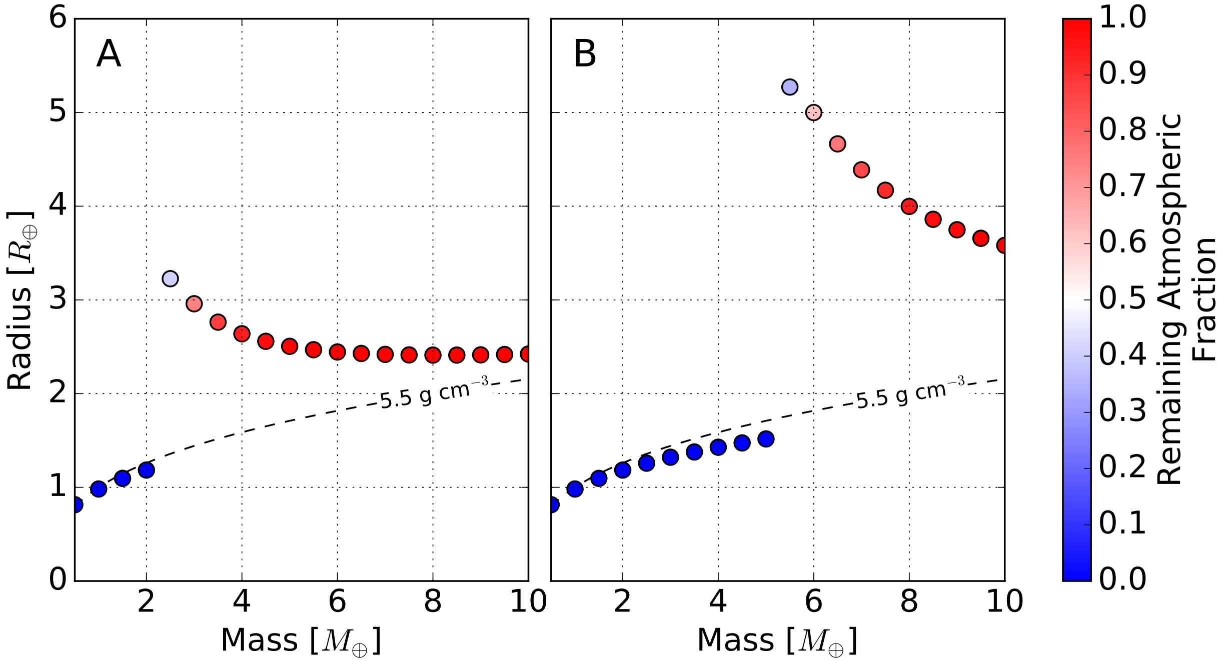

Figure 2.1: Atmospheric loss from planets between 0.5 and 10 Earth masses over 100 Myr with an initial H_2 atmosphere of 3 wt.% at 0.1 AU around a young, Sun-like star. The dashed curve shows the contour of fixed Earth-like density of 5.5 g cm^{-3}. Blue dots representing rocky bodies fall below this line due to compression at high mass. In both plots the model was run with $\tau = 100$ Myr, $R_g = 4157$ J kg^{-1} K^{-1}, $p_{XUV} = 5$ Pa, $F_{XUV} = 55$ W m-2, $\eta = 0.1$, and $\alpha = 0.03$. The planets in plot A had an isothermal atmospheric temperature of $T = 880$ K (corresponding to the effective temperature at 0.1 AU with a Bond albedo of 0), and the temperature was set to $T = 1760$ K in plot B. In both cases, we see a sharp cutoff between rocky and gas-enveloped planets occurring in the 1.2 $R_\oplus$ to 1.6 $R_\oplus$ range.

that increase rapidly with decreasing mass. In equation 2.1 we see that the R_{XUV} term is cubed, and it is the only term that changes greatly as mass is lost (for a 3 wt.% atmosphere M_p will only change by at most 3%). Thus, any change in the loss rate will be dominated by the R^3_{XUV} term.

In Figure 2.4, we see how, for planets with mass $< 2.5 M_\oplus$, R^3_{XUV} is orders of magnitude larger than $R_\oplus$ while the protoatmosphere remains, but for planets with mass 6-7 $M_\oplus$, R^3_{XUV}

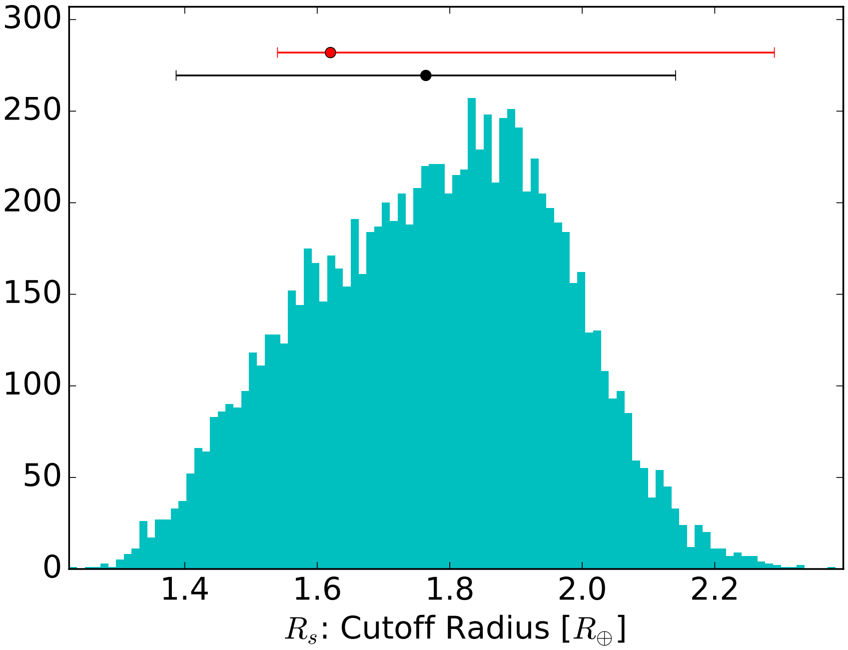

Figure 2.2: Ten thousand random parameter combinations were considered using a uniform distribution of the ranges given in Table 2.1 to calculate the cutoff between rocky and gas-enveloped planets. The number of resulting surface radii, R_s, at which the cutoff occurred for each parameter combination is shown in the histogram. The black dot and error bar show the mean cutoff of the distribution at 1.76 ± 0.38 $R_\oplus$ from our model with 2σ uncertainty. The red dot shows the observed $1.62^{+0.67}_{-0.08} R_\oplus$ measurement with 2σ uncertainty from Rogers (2015).

levels off to ∼15 $R_\oplus$. Not only do low mass planets have much larger loss rates due to this exponential increase in R_{XUV}, but they also have less overall atmospheric mass to lose. The strong nonlinearity of the hydrostatic equation shows us that there will exist a critical planet size below which R_{XUV} increases rapidly leading to substantial hydrodynamic escape. This non-linear dependence on R_{XUV} has been noted in previous work (e.g. Chen & Kipping, 2016; Lopez & Fortney, 2013) and, on average in our model, results in planets with cores larger than 1.76 ± 0.38 (2σ) $R_\oplus$ retaining a significant portion of their protoatmospheres. The largest planets that can lose their entire protoatmosphere are thus planets with rocky

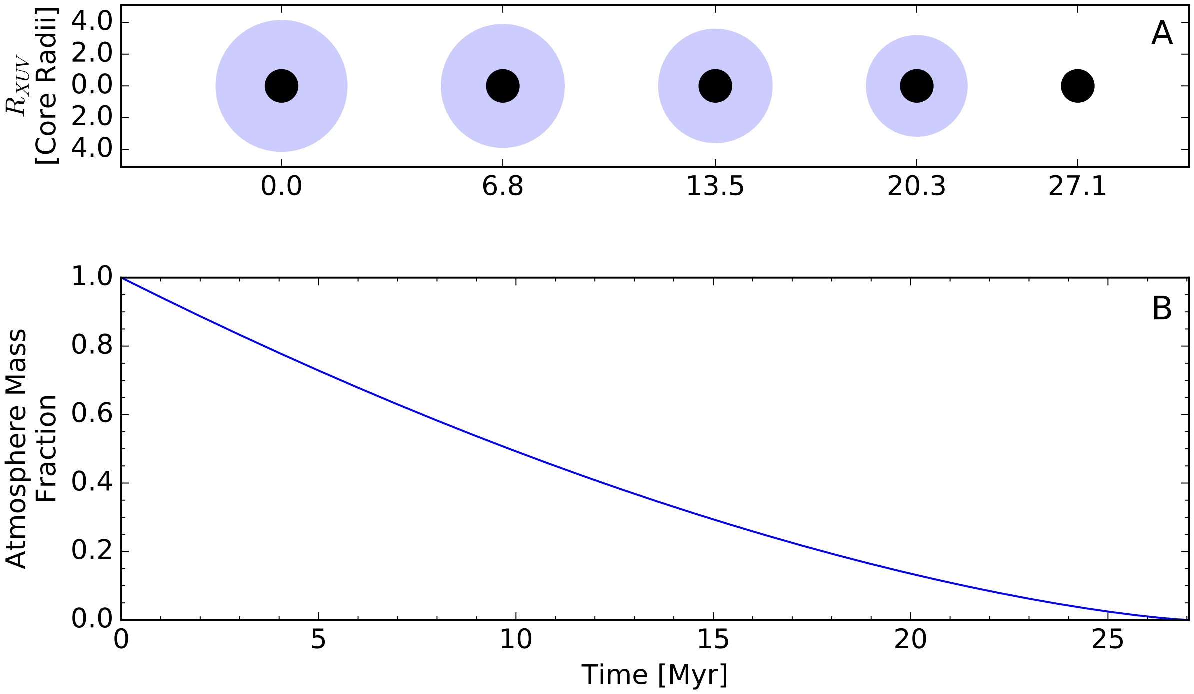

Figure 2.3: Model run for a 2 $M_\oplus$ planet with isothermal atmospheric temperature set to $T = 880$ K. The planet was assumed to orbit at 0.1 AU around a young, Sun-like star with the initial atmosphere representing 3 wt.%. The model parameters were set as $T = 880$ K, $F_{XUV} = 55$ W m^{-2}, $\alpha = 0.03$, $\eta = 0.1$, $p_{XUV} = 5$ Pa, $R_g = 4157$ J kg^{-1} K^{-1}, and $\tau = 100$ Myr. Plot A shows a snapshot of the planetary radius up to R_{XUV} at times of 0, 6.8, 13.5, 20.3, and 27.1 Myr in the simulation. The blue region shows the relative size of the planetary atmosphere, and the black region shows the size of the rocky core. Plot B shows the remaining atmospheric mass fraction over time. We see that R_{XUV} remains large even after most of the atmosphere has been lost.

cores less ~1.8 $R_\oplus$.

In addition to the predicted cutoff at 1.8 $R_\oplus$, our model shows that there should be a lack of planets with radii immediately larger and smaller than the cutoff radius. This is seen in Figure 2.1 where the abrupt jump from rocky to gas-enveloped planets may result in a void where planets are unlikely to exist. This agrees with a number of previous studies (see

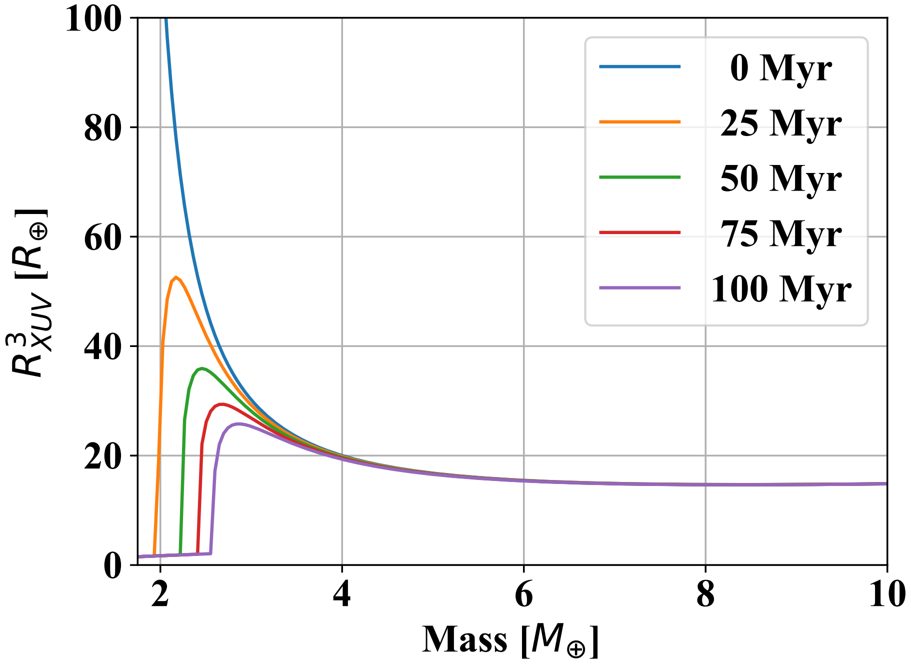

Figure 2.4: The value of R^3_{XUV} at times $\tau = 0$, 25, 50, 75, and 100 Myr (shown by the blue, orange, green, red, and purple curves, respectively) for planets between 1.75 and 10 $M_\oplus$ around a Sun-like star at 0.1 AU. The model parameters were set to $T = 880$ K, $F_{XUV} = 55$ W m^{-2}, $\alpha = 0.03$, $\eta = 0.1$, $p_{XUV} = 5$ Pa, and $R_g = 4157$ J kg^{-1} K^{-1}. The low mass planets have large R^3_{XUV} values that cause rapid loss. By ∼6 $M_\oplus$, R^3_{XUV} has become roughly constant with mass. The approximately flat line at low masses (below ∼2.5 $M_\oplus$ for the purple curve) indicates that, for a given τ, the atmosphere has been entirely lost and R^3_{XUV} is at the surface of the planet.

Section 2.2) and the recent work by Fulton et al. (2017) which found that such a deficit is indeed present in the current exoplanet data.

The exoplanet data from Fulton et al. (2017) is shown in Figure 2.5 with our model predictions. Our model indicates that for radii below ∼2 $R_\oplus$ planets are less likely to be gas-enveloped (the blue region in Figure 2.5), and for radii above ∼1.5 $R_\oplus$ planets are less likely to be rocky (the red region in Figure 2.5). The paucity of 1.5-2 $R_\oplus$ planets predicted by our model is seen in the Fulton et al. (2017) data. The missing planets fall into the evaporation

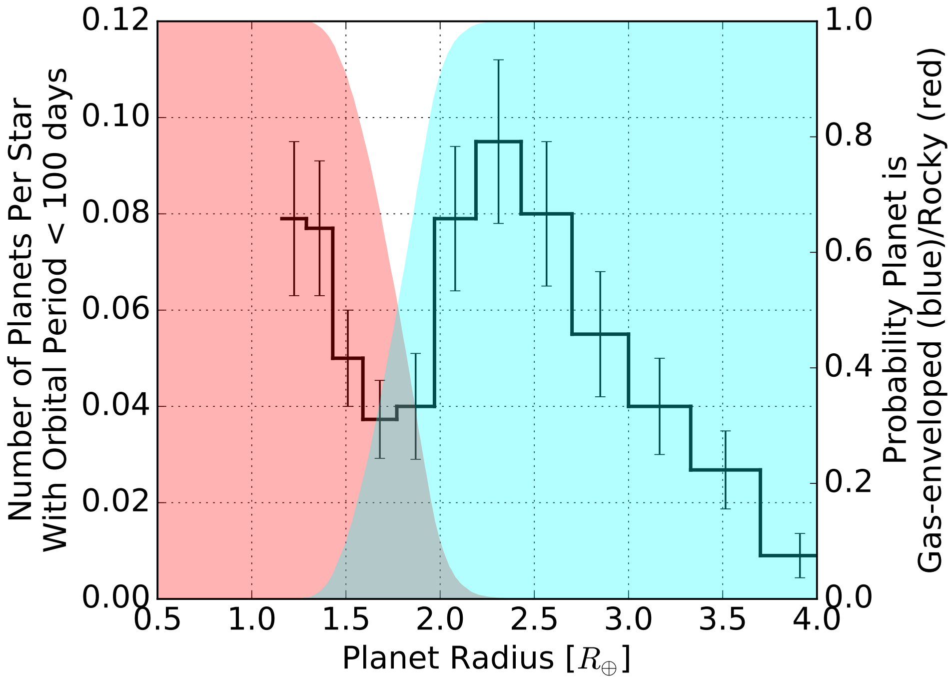

Figure 2.5: The exoplanet data from Fulton et al. (2017) is shown in the black curve (data taken from Fulton et al. (2017) Table 3). Our model predictions are shown by the shaded regions. Using the probability distribution generated in Figure 2.2 the red shaded region shows the probability that a planet is below the rocky planet cutoff, and the blue shaded region shows the probability that a planet is above the rocky planet cutoff. Beyond $\sim$1.5 $R_\oplus$ planets are unlikely to be rocky while below $\sim$2 $R_\oplus$ planets are unlikely to be gas-enveloped. Thus, our model predicts a lack of exoplanets with radii between 1.5-2 $R_\oplus$ which is indeed seen in the Fulton et al. (2017) data. Fulton et al. (2017) found that planets below $\sim$1.8 $R_\oplus$ are likely to be rocky while larger planets are likely to be gas-enveloped, with which our results agree. It should be noted that the vertical axes in this plot are arbitrarily scaled. The important feature, however, is the location of the transition between rocky and gas-enveloped planets and the width of the valley between that transition, which is agnostic of the vertical scaling.

valley described by previous XUV-driven hydrodynamic escape studies (see Section 2.2) and show that XUV-driven hydrodynamic escape is able to reproduce the major characteristics of the observed, low mass exoplanet population.

2.5 Discussion

The transition from rocky to gas-enveloped planets occurs where XUV-driven hydrodynamic escape predicts such a transition should occur (see Figure 2.5). That the transition has been predicted across numerous studies with models of varying complexity (see Section 2.2) and agrees with current exoplanet data leads us to conclude that hydrodynamic escape is plausibly the cause of the observed limit in rocky planet radii. The closely orbiting exoplanets (periods less than ∼100 days) modeled in this study comprise the majority of known, low mass exoplanets (e.g. Batalha, 2014). That XUV-driven hydrodynamic atmospheric escape is important for these planets is not surprising given the large XUV fluxes present at such short orbital periods.

As additional, longer period rocky planets are discovered the average cutoff in rocky planet size may decrease with increasing orbital period, as noted by Lopez & Rice (2016). However, at large orbital distances where the XUV flux is small and XUV-driven hydrodynamic escape becomes negligible other processes may limit the size of rocky planets. Indeed, Zeng et al. (2017) found a bimodal distribution in the current exoplanet data similar to Fulton et al. (2017) but note that it could be explained by formation scenarios rather than evolutionary ones (i.e. XUV-driven hydrodynamic escape). The radius limit for closely orbiting rocky planets appears to be set at $\sim 1.8\ R_\oplus$ by XUV-driven hydrodynamic escape, but to address the limit in rocky planet size for longer period planets, additional studies on rocky planet formation should be conducted.

Chapter 3

ICY MOONS IN THE HABITABLE ZONE

Status

This work was published under the title *The Longevity of Water Ice on Ganymedes and Europas around Migrated Giant Planets* by **Owen R. Lehmer, David C. Catling, and Kevin J. Zahnle**. It was published in *The Astrophysical Journal* in **2017**. See the reference Lehmer et al. (2017).

3.1 Abstract

The gas giant planets in the Solar System have a retinue of icy moons, and we expect giant exoplanets to have similar satellite systems. If a Jupiter-like planet were to migrate toward its parent star the icy moons orbiting it would evaporate, creating atmospheres and possible habitable surface oceans. Here, we examine how long the surface ice and possible oceans would last before being hydrodynamically lost to space. The hydrodynamic loss rate from the moons is determined, in large part, by the stellar flux available for absorption, which increases as the giant planet and icy moons migrate closer to the star. At some planet-star distance the stellar flux incident on the icy moons becomes so great that they enter a runaway greenhouse state. This runaway greenhouse state rapidly transfers all available surface water to the atmosphere as vapor, where it is easily lost from the small moons. However, for icy moons of Ganymede's size around a Sun-like star we found that surface water (either ice or liquid) can persist indefinitely outside the runaway greenhouse orbital distance. In contrast, the surface water on smaller moons of Europa's size will only persist on timescales greater than 1 Gyr at distances ranging 1.49 to 0.74 AU around a Sun-like star for Bond albedos of 0.2 and 0.8, where the lower albedo becomes relevant if ice melts. Consequently, small

moons can lose their icy shells, which would create a torus of H atoms around their host planet that might be detectable in future observations.

3.2 Introduction

One of the major results of exoplanet discoveries is that giant planets migrate (Chambers, 2009). This was first deduced from hot Jupiters, and although these are found around 0.5-1% of Sun-like stars (Howard, 2013), hot Jupiters are not the only planets to migrate and giant planet migration is likely widespread. Indeed, such migration probably occurred in the early solar system (Tsiganis et al., 2005).

All the giant planets in the solar system have a collection of icy moons. We expect that similar exomoons orbit giant exoplanets and that these moons would likely migrate along with their host planet. If a giant exoplanet were to migrate toward its parent star, icy moons could vaporize, similar to comets approaching the Sun, and develop atmospheres. In addition, they could melt and maintain liquid surfaces as they migrate inwards, which could be potentially habitable environments. Such a moon would have an atmosphere primarily controlled by the vapor equilibrium set by the surface temperature and the rate of hydrodynamic escape to space. As such, the longevity of the water shell and atmosphere will depend primarily on the distance to the host star and the exomoon radius and mass.

Several such bodies exist in the solar system, where the atmospheric thickness is determined by vapor equilibrium with a condensed phase, i.e. the Clausius-Clapeyron relation for the relevant volatile. Let us call such atmospheres Clausius-Clapeyron (C-C) atmospheres. The N_2 atmospheres on both Triton and Pluto are examples of C-C atmospheres, where the surface vapor pressure is in equilibrium with the N_2 surface ice at the prevailing temperature for each body. The present Martian atmosphere is another C-C atmosphere since the polar CO_2 ice caps at ∼148 K buffer the atmosphere to ∼600 Pa surface pressure (Leighton & Murray, 1966) (see (Kahn, 1985) for an explanation over geologic timescales).

For an icy exomoon migrating toward its parent star, the atmospheric water vapor will be controlled by the availability of surface water and temperature. Very deep ice and ice-covered oceans are possible on these moons given that water can account for ~5-40% of the bulk mass of icy moons in the solar system (Schubert et al., 2004). However, the small mass of exomoons and relatively high stellar flux as the exomoon migrates toward the star makes water vapor susceptible to escape. Assuming exomoons are of comparable size to the moons found in the solar system, this study looks at the end-member case of how rapidly a pure water vapor atmosphere will be lost hydrodynamically.

Hydrodynamic escape is a form of pressure-driven thermal escape where the upper levels of an atmosphere become heated and expand rapidly, accelerate through the speed of sound, and escape to space en masse (Hunten, 1990). An important process in atmospheric evolution, hydrodynamic escape likely occurred during the formation of the terrestrial atmospheres (Kramers & Tolstikhin, 2006; Kuramoto et al., 2013; Pepin, 1997; Tolstikhin & O'Nions, 1994). Moreover, hydrodynamic escape has been observed on exoplanets such as the gas giant HD 209458b, which orbits a Sun-like star at 0.05 AU and has hot H atoms beyond its Roche lobe, presumably deposited there by hydrodynamic escape (Linsky et al., 2010; Vidal-Madjar et al., 2004). The closer a body is to its parent star, the more effective the hydrodynamic escape, and the smaller the body, the more easily an atmosphere is lost (e.g. Zahnle & Catling, 2017).

The longevity of an atmosphere and icy shell will depend primarily on temperature, set in large part by the stellar flux available for absorption. As an ice covered exomoon moves towards its parent star, heating will cause more water vapor to enter the atmosphere, hastening the loss rate. In addition, this water vapor will provide a greenhouse effect, further warming the moon. At a certain exomoon-star distance the water vapor atmosphere will impose a runaway greenhouse limit on the outgoing thermal infrared (IR) flux from the exomoon. If the absorbed stellar flux exceeds this limit, the exomoon surface will heat rapidly until all available water is in the atmosphere as vapor. This limit represents the distance at which all surface water will be transferred to the atmosphere where it will be rapidly lost.

3.3 Methods

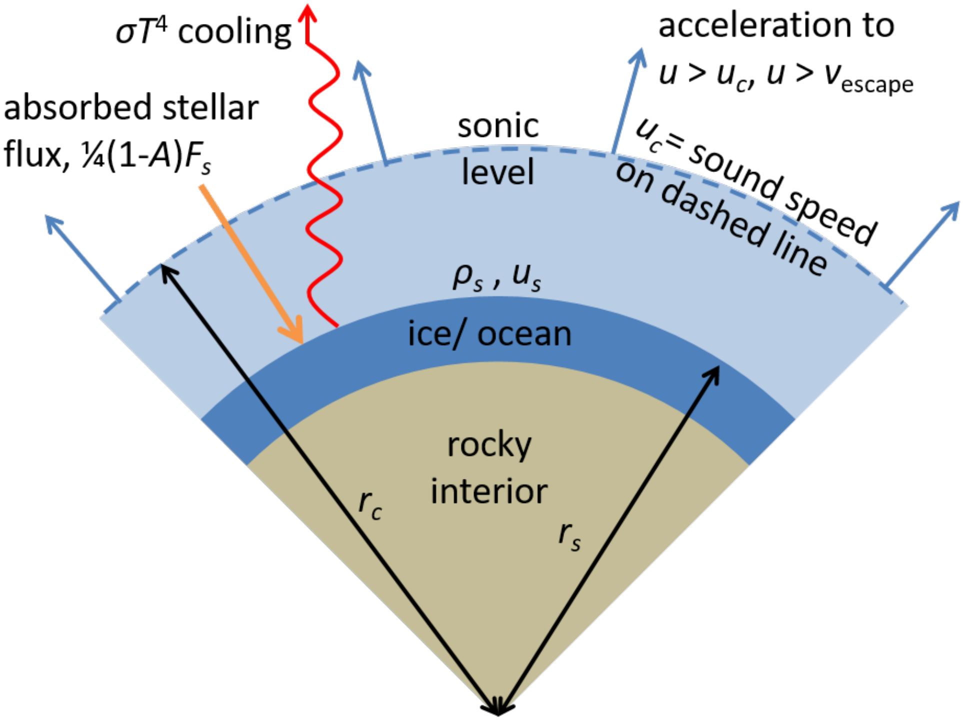

Figure 3.1: Conceptual visualization of the 1D hydrodynamic escape model. The incoming absorbed stellar flux, given by $1/4(1-A)F_s$, heats the exomoon surface, for Bond albedo A, and stellar flux F_s. The exomoon will remain in thermal equilibrium by evaporating water vapor, losing mass via hydrodynamic escape, and radiating in the thermal infrared. The thermal infrared radiation is given by σT^4 (σ is the Stefan-Boltzmann constant, T is the surface temperature) in a blackbody approximation. The outward radial flow velocity, u, increases monotonically until it surpasses the isothermal speed of sound, u_c, at the critical radius, r_c, where the gas is still collisional. Beyond the sonic level, u continues to rise and soon surpasses the escape velocity v_{escape}. The exomoon surface is at radius r_s with atmospheric near-surface density ρ_s and outward radial surface velocity u_s. See equation 3.2 for the global energy balance.

We consider three cases of hydrodynamic escape: (Section 3.3.1) an isothermal atmosphere where the atmospheric temperature is set by incoming stellar flux and equal to the effective temperature; (Section 3.3.2) a vapor saturated atmosphere where the temperature and humidity profiles of the entire atmosphere are dictated by the C-C relation; and (Section 3.3.3) an isothermal atmosphere similar to Section 3.3.1 but the surface temperature, and the isothermal atmospheric temperature, are increased from the effective temperature by the total greenhouse warming of the water vapor atmosphere. We chose the isothermal and C-C cases because they present upper and lower limits on the rates of hydrodynamic escape, respectively, as described below. Figure 3.1 provides a conceptual picture of the model.

For a pure water vapor atmosphere around a Sun-like star, an isothermal atmosphere at the effective temperature represents the greatest possible temperature at the top of atmosphere to drive hydrodynamic escape. Water vapor radiates in the IR more efficiently than it absorbs sunlight, so the radiative-convective temperature for a pure water vapor atmosphere will be less (Pierrehumbert, 2010; Robinson & Catling, 2012). As such, the isothermal atmospheric approximation provides an upper bound on the atmospheric loss rate. In contrast, the lowest possible temperature to drive hydrodynamic escape is the saturated case, where the temperature and pressure at all heights are set by the C-C relation, which is defined by

$$T(P) = \frac{T_0}{1 - \ln(P/P_0)/(RT_0/L_v)} \tag{3.1}$$

for reference temperature T_0 at reference pressure P_0, where R is the universal molar gas constant, and L_v is the latent heat of vaporization for water (e.g. Pierrehumbert, 2010, p. 100). The surface temperature is assumed to be in equilibrium with the incoming stellar flux, cooling associated with mass loss via hydrodynamic escape, and latent heat of evaporation. If the temperature were to decrease with altitude faster than the C-C relationship, the water vapor would condense out resulting in a C-C curve that, when extrapolated, would result in a surface temperature no longer in equilibrium with incoming stellar flux and escape. Therefore, the hydrodynamic loss rate of a pure water vapor atmosphere is bounded by the isothermal and saturated cases, which we will now consider in turn.

3.3.1 Isothermal case

In the blackbody approximation, radiative cooling is given by σT^4 at isothermal temperature T, allowing a straightforward formulation of escape versus radiative cooling. As such, the first order global energy balance for an icy exomoon is between incoming stellar flux versus the energy flux lost to vaporizing the water, lifting molecules out of the gravity well, and radiative cooling, i.e.,

$$\underbrace{\frac{1}{4}(1-A)F_s}_{\text{absorbed stellar flux}} = \underbrace{\left(\frac{GM}{r_s} + L_v\right)\rho_s u_s}_{\text{mass loss flux}} + \underbrace{\sigma T^4}_{\text{radiative cooling}} . \tag{3.2}$$

Here F_s is the incoming solar flux available for absorption, A is the Bond albedo, σ is the Stefan-Boltzmann constant, r_s is the surface radius where the atmospheric density is ρ_s, such that $\rho_s u_s$ is the mass flux given an outward radial flow velocity at the surface u_s, G is the gravitational constant, and M is the mass of the exomoon.

In addition to the C-C relationship (equation 3.1), three equations are needed to derive the steady state, hydrodynamic atmospheric loss in the isothermal approximation (e.g. Catling & Kasting, 2017, Ch. 5). The first is steady state mass continuity, given by

$$\frac{\partial}{\partial r}\left(r^2 \rho u\right) = 0 \tag{3.3}$$

where r is the radial distance from the planet's center, u is the outward radial flow velocity, and ρ is the atmospheric density. Steady state momentum conservation is expressed as

$$u\frac{\partial u}{\partial r} + \frac{1}{\rho}\frac{\partial p}{\partial r} = g \tag{3.4}$$

with gravity g and pressure p. Finally, the equation for energy balance is given by equation 3.2. Combining equations 3.1, 3.2, 3.3, and 3.4 an analytic expression for the isothermal atmospheric mass loss rate in kg s^{-1} is given by (see Section 3.7.1 for the derivation):

$$\dot{M} = \pi \rho_s \frac{G^2}{u_0^3} M^3 \exp\left[\frac{3}{2} - \frac{G}{u_0^2}\left(\frac{3}{4\pi\rho_m}\right)^{-1/3} M^{2/3}\right] \tag{3.5}$$

where u_0 is the isothermal sound speed given by $u_0^2 = kT/m$ with Boltzmann constant k and mean molecular weight m, and ρ_m is the mean density of the exomoon (assumed 2 g cm^{-3}). The atmospheric surface density, ρ_s, is set the by C-C equation for the saturation vapor pressure of water at the prevailing temperature. For time averaged mass loss rate, $\overline{\dot{M}}$, the lifetime of the exomoon surface water is given by

$$\tau_{water} = \frac{M_{water}}{\overline{\dot{M}}} \tag{3.6}$$

For an upper limit, we assume the total mass of water present on the exomoon surface, M_{water}, is 40% of the bulk mass. However, even if 5% water were used (the lower limit for Europa (Schubert et al., 2004)) from equation 3.6 we can see that it would translate to a change in τ_{water} by a factor of 8, compared to 40% water. From equation 3.5 we see that $\dot{M}$, and hence τ_{water}, has an exponential dependence on mass, so we would anticipate that the difference between 5% and 40% water is not the major factor determining τ_{water}, which is borne out by our results. In addition, if substantial water vapor is lost the bulk density of the moon, ρ_m, may increase over time. However, from equation 3.5 we see that the exponential term scales like $-\rho_m^{1/3} M^{2/3}$ with $M^{2/3}$ largely determining the loss rate so the sensitivity to ρ_m is small.

It is important to note that in equation 3.5 we have assumed the mass loss rate, $\dot{M}$, is sufficiently small that energy balance is dominated by radiative loss. This is indeed the case for exomoons of interest in this paper, where the low temperature water vapor atmospheres last for more than 1 Gyr. The surface pressures are well below ~500 Pa until the runaway greenhouse limit is reached. For bodies with rapid hydrodynamic escape the numerical approach defined in Section 3.7.1 is appropriate.

3.3.2 Saturated temperature profile case

The saturated case is derived from the same equations as the isothermal case (equations 3.1, 3.2, 3.3, and 3.4) but temperature is allowed to change with altitude. The temperature at the critical point at radius r_c in Figure 3.1 (where the isothermal sound speed u_0 equals the radial escape speed) is set such that numerically integrating equations 3.1, 3.2, 3.3, and 3.4 from the critical point to the surface will result in a surface temperature equivalent to that in equilibrium with incoming solar flux taking into account the evaporative cooling (see Section 3.7.2 for details). Once the critical temperature is known the radial outflow velocity is readily calculated and thus the mass loss rate.

3.3.3 Isothermal case with greenhouse effect considered

In Section 3.3.1 we let the isothermal atmospheric temperature be set by just the incoming stellar flux and thus be equal to the effective temperature. However, for a thick water vapor atmosphere the surface will be heated by the greenhouse effect of the overlying atmosphere. In this case, we still used an isothermal atmosphere approximation but increased the atmospheric temperature by the total greenhouse warming of the atmosphere at the surface. The larger isothermal atmospheric temperature under this regime will increase the hydrodynamic loss rate compared to Section 3.3.1.

To account for the atmospheric greenhouse effect, we used a gray, radiative, plane-parallel approximation where the total gray atmospheric optical depth in the thermal infrared at the surface is given by

$$\tau = \frac{\kappa_{ref} P^2}{2 g P_{ref}} \tag{3.7}$$

for mass absorption coefficient κ_{ref} at pressure P_{ref} and surface pressure P where pressure broadening causes the P^2 dependency of the optical depth (Catling & Kasting, 2017, p. 381). Here we used $\kappa_{ref} = 0.05$ m^2 kg^{-1} and $P_{ref} = 10^4$ Pa (Catling & Kasting, 2017, Ch. 13). Having $\tau \propto P^2$ in equation 3.7 is appropriate for thick atmospheres, which is the case when the runway greenhouse limit is approached. For thin atmospheres $\tau \propto P$ is appropriate (Catling & Kasting, 2017, p. 382). In this study, the surface pressures are in the low-pressure regime (less than ∼500 Pa) until the runaway limit is reached. However, the difference between $\tau \propto P^2$ and $\tau \propto P$ in equation 3.7 is small at such low pressures where the total greenhouse warming is less than a few K until the runaway limit is reached. Setting $\tau \propto P$ for such low-pressure moons in equation 3.7 has negligible impact on the calculated mass loss rate so we approximate the optical depth of all atmospheres in this study with $\tau \propto P^2$. Once the total optical depth of the atmosphere is known from equation 3.7, the first order global energy balance is given by (see Section 3.7.3 for derivation)

$$\frac{1}{4}(1-A)F_s\left(1+\frac{\tau}{2}\right) = \left(\frac{GM}{r_s}+L_v\right)\rho_s u_s + \sigma T_s^4 \tag{3.8}$$

and from equations 3.3 and 3.4 we derived an expression for $\rho_s u_s$ (see Section 3.7.1)

$$\rho_s u_s = \rho_s u_0 \left(\frac{r_c}{r_s}\right)^2 \exp\left[-\frac{1}{2}+\frac{GM}{u_0^2}\left(\frac{1}{r_c}-\frac{1}{r_s}\right)\right] \tag{3.9}$$

Equations 3.1, 3.7, 3.8, and 3.9 were solved simultaneously to find T and u_s, with ρ_s being given by the ideal gas law. The mass loss rate is then calculated by

$$\dot{M} = 4\pi\rho_s u_s r_s^2 \tag{3.10}$$

Using equation 3.10 the time averaged loss rate is calculated and surface water lifetime is then obtained via equation 3.6.

It is possible that no physically meaningful solution exists to equations 3.1, 3.7, 3.8, and 3.9. When the initial surface temperature, and therefore surface pressure, is large (above ∼260 K for this model), the optical depth given by equation 3.7 will be significant. This will cause an increase in surface temperature further increasing the surface pressure and thus the optical depth of the atmosphere. The positive feedback between temperature, pressure, and optical depth will cause equations 3.1, 3.7, 3.8, and 3.9 to have no valid solution if the initial surface temperature, set by the incoming stellar flux, is large. The exomoon-star distance where this positive feedback results in no solution is the runaway greenhouse limit, and it is akin the runaway limit found by Ingersoll (1969).

For all three model scenarios, we considered a pure water vapor atmosphere above a surface water reservoir. We looked at icy exomoons with masses ranging from 0.005 to 0.04 Earth masses between 0.9 and 2.0 AU from a Sun-like star. This mass range includes bodies slightly smaller than Europa (0.008 $\mathrm{M_{Earth}}$), and slightly larger than Ganymede (0.025 $\mathrm{M_{Earth}}$). We set the Bond albedo to 0.2 for each run. We chose a Bond albedo of 0.2 for two reasons, the first is that it approximately represents the lower bound for icy moon Bond albedos in the solar system (Buratti, 1991; Howett et al., 2010). In addition, a Bond albedo of 0.2 approximates the albedo of open ocean with partial cloud cover (Goldblatt, 2015; Leconte et al., 2013). Should an icy moon form surface oceans, the 0.2 Bond albedo gives us the best representation when calculating water longevity.

3.4 Results

For each body in the range of masses and distances considered, we calculated the time averaged mass loss rate, $\overline{M}$, using a time step of 10^4 years. With the water content of each world assumed to be 40% of the bulk mass, the water lifetime, τ_{water}, was then calculated via equation 3.6. The results of these calculations are shown in Figure 3.2.

Figure 3.2 shows contours of τ_{water} as a function of stellar distance and escape velocity, which is defined as

$$v_{esc} = \left(\frac{2GM}{r_s}\right)^{1/2}. \tag{3.11}$$

The runaway greenhouse star-exomoon distance is shown with red contours on each plot in Figure 3.2. From Figure 3.2A we can see that, in the analytic model, water on a Ganymede-like exomoon (with an escape velocity of ~2.74 km $\mathrm{s^{-1}}$) would persist indefinitely at a distance beyond the runaway limit. However, the ice on a Europa sized moon would only survive for timescales greater than 1 Gyr beyond ~1.5 AU. Given that the isothermal and saturated cases represent the upper and lower bounds on escape rate, the true solution is likely somewhere between the two plots (Figures 3.2A and 3.2B).

In Figure 3.2C, the impact of the water vapor greenhouse effect was considered. Under the radiative model, the greenhouse effect of a pure water vapor atmosphere contributes a

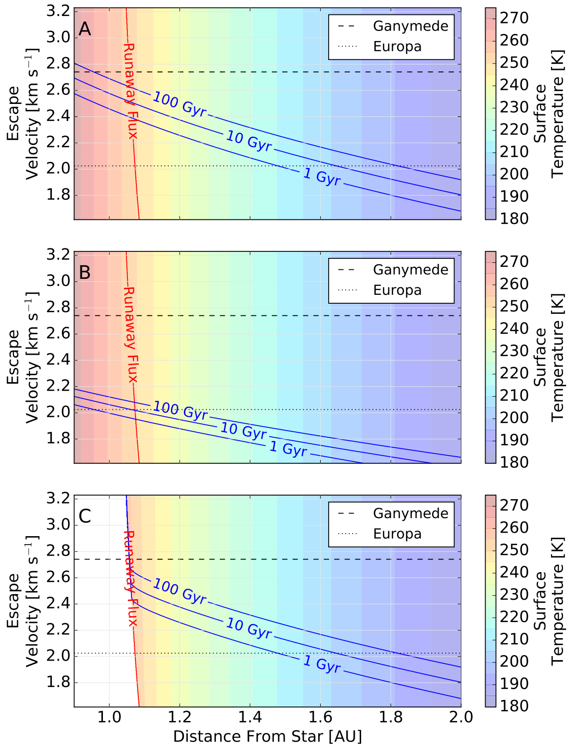

Figure 3.2: For all three plots, the red curve represents the Runaway Flux where the icy moon will be close enough to the star that a runaway greenhouse occurs. The blue curves represent contours of surface water lifetime (plotted in Gyr). The surface temperatures of the moons are shown by the colored background. In plots A and B the surface temperature corresponds to the effective temperature. In plot C the colored background shows the surface temperature, beyond the runaway limit distance, accounting for the effect of the water vapor greenhouse. Comparing the surface temperatures in plot C to those in A and B the water vapor greenhouse is negligible except very close to the runaway limit distance. The rate of hydrodynamic escape depends on both the mass and radius of the exomoon, as such we plot escape velocity vs. distance to incorporate both parameters. Plot A shows the isothermal analytic model (Section 3.3.1) based on equation 3.5. Plot B shows the saturated case where the atmosphere was assumed to follow the Clausius-Clapeyron equation and was saturated from the surface to the critical radius for escape (Section 3.3.2). Plot C shows the isothermal model with the greenhouse effect of water vapor considered (Section 3.3.3). The results shown in all three figures are dependent on the chosen albedo. If the albedo were to be increased from the chosen value of 0.2, the effect would be a linear decrease in absorbed flux. This would shift the runaway limit and the contours of ocean lifetime closer to the host star. For a Ganymede sized moon with a Bond albedo of 0.2 (shown here), 0.4, and 0.8 the runaway limit occurs at 1.05, 0.91, and 0.52 AU respectively.

few degrees K of warming. However, if the body receives sufficient stellar warming a runaway occurs. With a pure water vapor atmosphere the surface never rises above the freezing point of water without entering a runaway greenhouse. But if clouds were to increase the albedo, a world with a liquid water surface may exist with a marginally stable surface temperature up to 275 K (Goldblatt et al., 2013). However, such a world may be transient and easily swing to either a snowball via the ice-albedo feedback, or a runaway greenhouse state (Goldblatt et al., 2013).

3.5 Discussion

The closely packed lifetime lines in Figure 3.2 result from a strong dependence on escape velocity and therefore on mass. From equation 3.5 and 3.6, with all the constants stripped away, we see that there is an exponential relationship between ocean lifetime and mass, if the mean density of the moon is held constant, given by

$$\tau_{water} \propto \frac{1}{M} \exp\left(M^{2/3}\right) \tag{3.12}$$

For constant density, $\overline{\rho}$, the escape velocity from equation 3.11 is $v_{esc} = (8/3\pi G r_s^2 \overline{\rho})^{1/2} \propto r_s$, so implicit in equation 3.12, $M \propto v_{esc}^3$ so $\tau_{water} \propto v_{esc}^{-3} \exp\left(v_{esc}^2\right)$. This strong exponential dependence on v_{esc}^2 can be seen in Figure 3.2 in both the isothermal and saturated cases. There is a threshold mass region below which surface water is transient, while moons with masses above this region will last for billions of years. Ganymede sized moons will persist indefinitely beyond the star-exomoon distance of the runaway limit.

If a gas giant planet possessed rapidly evaporating icy moons future observations may be able to detect them. The escaped H from water would form a torus in the orbit of the moon that may produce detectable scattering in the Lyman-α. However, for young, migrating planets this H torus may be indistinguishable from captured nebular H before it dissipates. This degeneracy could be addressed by observing aging gas giant planets that are just entering the habitable zone as the host star brightens over time. As a Jupiter-like planet enters the habitable zone around an aging star, hydrogen is unlikely to escape from the planet. Indeed, if we assume a Jupiter-like planet at 0.9 AU around a Sun-like star has an exobase temperature of 1500 K then, following Sanchez-Lavega (2011, p. 88), the thermal loss of hydrogen via Jeans' escape from such a planet will be $\sim 10^{-37}$ kg s^{-1}. This is ∼40 orders of magnitude less than the loss rate from icy moons at the same orbital distance so any observed H torus may be an indication of evaporating moons. Icy moons around such a planet are of particular interest because they may provide habitable surface conditions for hundreds of millions to billions of years, depending on the stellar type (Ramirez & Kaltenegger, 2016). As the host star brightens the smallest icy moons in the habitable zone would rapidly evaporate, producing the H torus, while more massive moons could retain their surface water for billions of years.

A similar torus-producing process occurs for Io, where a plasma torus around Jupiter contains sulfur and oxygen lost by the moon that are trapped by Jupiter's magnetic field lines (Yoshioka et al., 2011). Also, O atoms may linger around the icy exomoons, analogous to the O_2-rich collisional atmosphere of Callisto (Cunningham et al., 2015) and could possibly escape the moon to form a torus similar to the escaped H. A second, heavier component in the exomoon's atmosphere, such as oxygen, would generally act to lower the rate of escape and water loss. However, a more sophisticated model than presented here is required to study escape from a multicomponent atmosphere.

3.6 Conclusions

Planetary migration is likely a common phenomenon throughout planetary systems (Tsiganis et al., 2005). In addition, all the large planets in the solar system have a retinue of icy moons and gas giant exoplanets may have similar icy moons. Inward migration by a gas giant would subject its icy moons to increased stellar heating. Like a comet entering the inner solar system, the moons could evaporate and create atmospheres.

The longevity of such an atmosphere depends strongly on the distance from the host star, and the mass and radius of the exomoon. The smaller the star-exomoon distance, the warmer the icy exomoon will become. As an icy exomoon approaches a distance of ∼1.1

AU around a Sun-like star it will enter a runaway greenhouse state when the surface melts. However, this cutoff is dependent on the albedo of the moon, which was set to 0.2 in this paper. Increasing the albedo will allow stable surface conditions at closer orbital distances before the runaway state is achieved. The high temperatures from a runaway state will drive rapid hydrodynamic escape and erode the water from the exomoon on very short timescales.

If the exomoon sits beyond this runaway limit the surface water may persist much longer. Beyond the star-exomoon distance of the runaway limit, there is an exponential relationship between mass and water longevity. For an icy moon of Ganymede's size around a Sun-like star, surface waters will likely persist indefinitely. Large moons of this size will maintain their atmospheres for long periods in the habitable zone and could potentially maintain a liquid surface for timescales greater than 1 Gyr. Thus, such moons could be habitable. However, an icy moon of Europa's size would evaporate rapidly at ∼1.1 AU around a Sun-like star, and only beyond ∼1.5 AU would surface water (as ice) on a Europa sized moon last for more than 1 Gyr.

3.7 Derivation of escape models

3.7.1 Isothermal model

The three key equations for hydrodynamic escape – continuity, momentum, and energy – can be written generally (e.g., multiple species, etc. (Koskinen et al., 2013)) but we will use a simplified spherically symmetric model with constant mean molecular mass (see (Catling & Kasting, 2017, Ch. 5) for a more complete discussion of the topic). We assume the atmospheric density and atmospheric flow velocity only change in the radial direction. As such, the derivatives for mass continuity and momentum conservation are complete. Under these assumptions, the time-dependent and steady-state continuity and mass conservation equations are as follows. Continuity is given by:

$$\frac{\partial \rho}{\partial t} = -\frac{1}{r^2}\frac{d}{dr}(r^2\rho u), \text{ steady state: } \frac{d}{dr}(r^2\rho u) = 0 \tag{3.13}$$

where ρ is the mass density, r is the radial distance from the planet's center, and u is the atmospheric flow velocity. Momentum conservation is given by:

$$\frac{\partial(\rho u)}{\partial t} = -\rho u \frac{du}{dr} - \frac{dp}{dr} + \rho g, \text{ steady state: } u\frac{du}{dr} + \frac{1}{\rho}\frac{dp}{dr} = g \tag{3.14}$$

where p is pressure, and g is gravity.

If we assume an isothermal atmosphere, we can relate pressure and density with the isothermal sound speed

$$u_0^2 = \frac{kT}{m} \tag{3.15}$$

where k is the Bolztmann constant, T is the isothermal temperature, and m is the mean molecular mass of the atmosphere. From the ideal gas law

$$p = \rho u_0^2 \tag{3.16}$$

Integrating equation 3.13 in the steady state, we get the mass escape rate per steradian of $r^2\rho u$, which, when combined with equations 3.13 and 3.14, gives an expression for the isothermal planetary wind from a body with mass M:

$$(u^2 - u_0^2)\frac{1}{u}\frac{du}{dr} = \frac{2u_0^2}{r} + g, \text{ or } (u^2 - u_0^2)\frac{1}{u}\frac{du}{dr} = \frac{2u_0^2}{r} - \frac{GM}{r^2}. \tag{3.17}$$

Equation 3.17 is analogous to Parker's solar wind equation. For a strongly bound atmosphere at some critical distance from the planet's surface, the right hand side of equation 3.17 reaches zero, indicating that either the flow reaches the speed of sound or $(du/dr)_c = 0$. The subsonic solution, $(du/dr)_c = 0$, requires a finite background pressure that inhibits escape so we will focus on the transonic solution where $u^2 = u_0^2$. The transonic solution has $du/dr > 0$ at all times and is consistent with a strongly bound atmosphere at the surface and zero pressure at infinity.

The critical distance r_c occurs in equation 3.17 when $u^2 = u_0^2$ which gives us:

$$0 = \frac{2u_0^2}{r_c} - \frac{GM}{r_c^2} \tag{3.18}$$

Solving for r_c in equation 3.18 we find

$$r_c = \frac{GM}{2u_0^2}. \tag{3.19}$$

If we integrate equation 3.17 from the surface radius r_s to r_c and ignore the u^2 term near the surface, where it is negligible for bodies of interest in this study, we get the equation:

$$\rho_s u_s = \rho_s u_0 \left(\frac{r_c}{r_s}\right)^2 \exp\left[-\frac{1}{2} + \frac{GM}{u_0^2}\left(\frac{1}{r_c} - \frac{1}{r_s}\right)\right]. \tag{3.20}$$

As the radial distance from the moon increases the mass flux, ρu (in kg m^{-2} s^{-1}), decreases. The steady state continuity given by equation 3.13, when integrated gives $4\pi r^2 \rho u = C$ where the constant of integration C is just the total rate of mass loss (in kg s^{-1}) through a spherical surface. As r goes to infinity ρu goes to 0 since $\rho u \propto 1/r^2$. Therefore, the outflowing wind loses kinetic energy as $r \to \infty$. Thus, the energy flux required to drive the escaping mass flux is given by the energy required to remove the mass flux from the gravity well of the moon, $\rho_s u_s GM/r_s$.

A first-order global energy balance between insolation and cooling via mass loss is then given by:

$$\frac{1}{4}(1-A)F_s = \left(\frac{GM}{r_s} + L_v\right)\rho_s u_s + \sigma T^4 \tag{3.21}$$

where A is the Bond albedo, F_s is the incident stellar flux, and σ is the Stefan-Boltzmann constant. The escape flux is given by $\rho_s u_s$ and is multiplied by the energy required for that flux to escape the planet. The energy includes a gravitational potential energy term, and the latent heat of vaporization L_v (for this model $L_v = 2.5 \times 10^6$ J kg^{-1}). In equation 3.21 we assume the atmosphere is transparent to both shortwave and infrared radiation.

Equations 3.20, and 3.21 can be solved simultaneously for the two unknowns u_s and T. Once solved, we can calculate the total escaping mass rate by:

$$\dot{M} = 4\pi \rho_s u_s r_s^2 \tag{3.22}$$

with ρ_s being calculated from $\rho_s = P_s/u_0^2$ with surface pressure P_s. We calculate surface pressure with equation 3.1 for a C-C atmosphere given the surface temperature of water, where reference parameters are at the triple point: $P_0 = 611.73$ Pa, $T_0 = 273.16$ K. For our model, we only consider water worlds with pure H_2O atmospheres so estimating the surface density from the saturation vapor pressure is valid (Adams et al., 2008). We refer to this approach, where 3.20 and 3.21 are solved numerically, as the **Numerical Model**.

For the slowly evaporating moons of interest in this study, those with surface water lasting more than 1 Gyr, the escape is so slow it does not appreciably cool the moon. Thus an analytic model can be derived by neglecting the mass loss flux cooling term in equation 3.21. With the simplified equation 3.21 our isothermal temperature is simply calculated from incoming stellar flux. And, from our assumption that the exomoons have an average bulk density of 2 g cm^{-3}, we can calculate the surface radius $r_s = (3M/(4\pi\rho_{exomoon}))^{1/3}$. Substituting these two equations into equation 3.20 we find that

$$u_s = u_0 \frac{r_c^2}{r_s^2} \exp\left[\frac{3}{2} - \frac{G}{u_0^2}\left(\frac{3}{4\pi\rho_{exomoon}}\right)^{-1/3} M^{2/3}\right] \tag{3.23}$$

By plugging equation 3.23 into equation 3.22, we get the analytic expression for the mass loss due to hydrodynamic escape given in equation 3.5.

Calculating u_s in this manner assumes the temperature in our energy balance equation is a constant and set solely by the incoming stellar flux and the emitted thermal flux from the surface. For the low temperature bodies (< 273 K) we are interested in for this study, equation 3.23 gives identical results as the previously defined numerical model until the runaway limit is approached. See Figure 3.3 for a comparison.

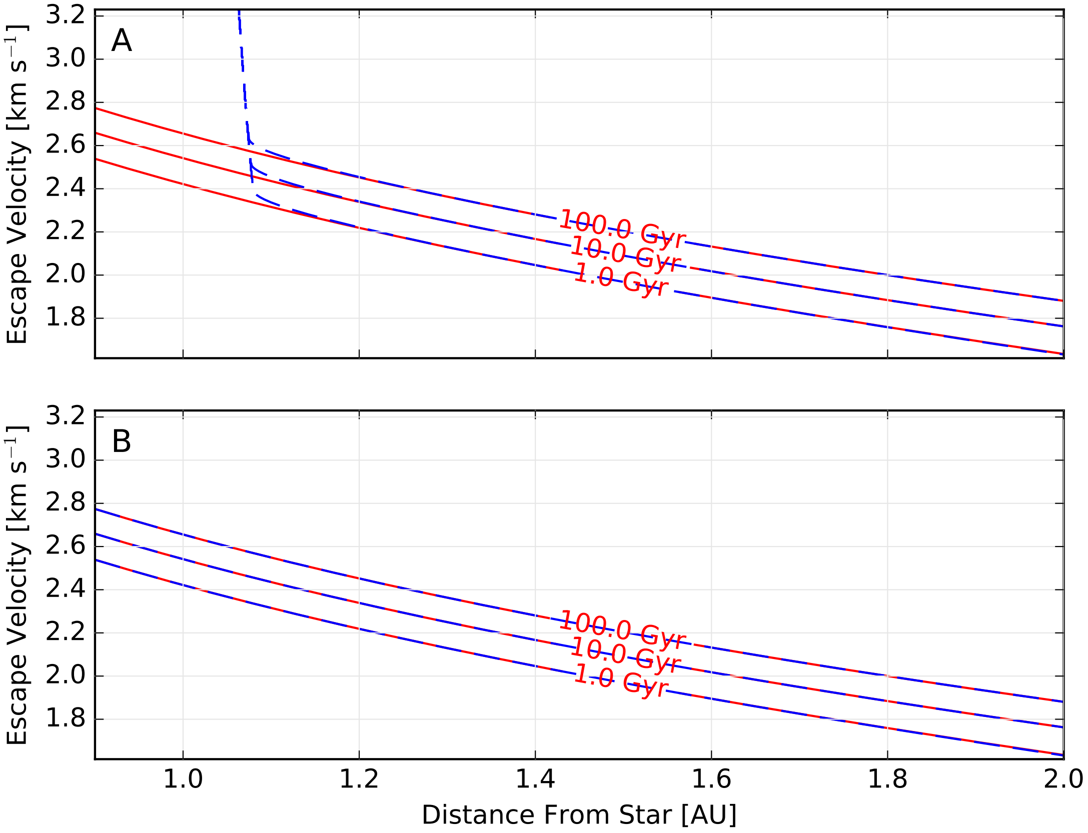

Figure 3.3: Contours of surface water lifetime comparing the analytic model given by equation 3.5, shown in red, and the numerical approach where T and u_s are solved for simultaneously, shown in dashed blue contours. Plot A shows the analytic model, which does not consider the greenhouse effect, plotted with the numerical model taking into account the greenhouse effect of water vapor as derived in Section 3.7.3. Both models produce identical results until the runaway limit is approached and the numerical model asymptotes along the limit. Plot B shows the analytic and numerical models as well; however, the greenhouse effect is neglected in the numerical model for this plot. In this case, both methods produce identical results, as expected, for slowly evaporating bodies with surface water lasting more than 1 Gyr.

3.7.2 Saturated model

We also modeled hydrodynamic escape from a non-isothermal atmosphere, the saturated case. To model escape in the saturated case we start with equations 3.13, 3.14, 3.15, and 3.16. Instead of using equation 3.1 to relate temperature and pressure, we will approximate the Clausius-Clapeyron relation with an expression similar to Tentens' formula, given by

$$p = p_w \exp\left(-T_w/T\right) \tag{3.24}$$

for reference temperature T_w and pressure p_w. A reasonable approximation for $250 < T < 400$ K over water takes $T_w = 5200$ K and $p_w = 1.13 \times 10^6$ bar. A very good approximation for $150 < T < 273$ K over ice takes $T_w = 6140$ K and $p_w = 3.53 \times 10^7$ bar. From Wexler (1977), whose expression we've approximated, the simple exponential fit is likely good to within a few percent for the temperatures in our model. This simplified expression is desirable because we want to work with an analytic expression for dT/dr.

We can eliminate p from equation 3.14 using equations 3.15 and 3.16, giving us

$$u\frac{du}{dr} + \frac{u_0}{\rho}\frac{d\rho}{dr} + \frac{u_0^2}{T}\frac{dT}{dr} = -\frac{GM}{r^2}. \tag{3.25}$$

We use equation 3.24 to express dT/dr in terms of $d\rho/dr$

$$\frac{u_0^2}{\rho}\frac{d\rho}{dr} = \left(\frac{T_w - T}{T}\right)\frac{u_0^2}{T}\frac{dT}{dr} \tag{3.26}$$

and equation 3.13 eliminates $d\rho/dr$ in terms of du/dr giving us our saturated wind equation

$$\left(u - \frac{u_0^2}{u}\left(\frac{T_w}{T_w - T}\right)\right)\frac{du}{dr} = \frac{2u_0^2}{r}\left(\frac{T_w}{T_w - T}\right) - \frac{GM}{r^2} \tag{3.27}$$

or equivalently as an expression for du/dr

$$\frac{1}{u}\frac{du}{dr} = \frac{N}{D} = \frac{(2u_0^2/r)(T_w/(T_w - T)) - GM/r^2}{u^2 - u_0^2(T_w/(T_w - T))} \tag{3.28}$$

where the numerator $N(r, T)$ is

$$N = \frac{2u_0^2}{r}\left(\frac{T_w}{T_w - T}\right) - \frac{GM}{r^2} \tag{3.29}$$

and the denominator $D(r, T, u)$ is

$$D = u^2 - u_0^2\frac{T_w}{T_w - T} \tag{3.30}$$

Equation 3.28 is the form we will use to numerically integrate $u(r)$. Equation 3.27 can be written equivalently as

$$D\frac{1}{u}\frac{du}{dr} = N. \tag{3.31}$$

Recall from the isothermal case that, for hydrodynamic escape from a strongly bound atmosphere, $du/dr > 0$. Near the surface of the moon the numerator, $N(r, T)$, will be negative as the gravity term will dominate given that our atmosphere is strongly bound. At some distance r_c the $2u_0^2/r$ term will equal the force of gravity, so $N(r, T) = 0$ at r_c. Since $N(r, T) = 0$ and $du/dr > 0$, from equation 3.31, $D(r, T, u) = 0$ at r_c as well. At the critical point, $N_c = 0$ provides a simple relation between T_c and r_c

$$r_c = \frac{GMm(T_w - T_c)}{2kT_cT_w}. \tag{3.32}$$

Similarly, $D_c = 0$ relates u_c and T_c by

$$u_c^2 = (u_0^2)_c\frac{T_w}{T_w - T_c} = \frac{GM}{2r_c^3}. \tag{3.33}$$

The transonic solution is obtained by numerically integrating equation 3.28 from the critical point to the surface. The first step is to solve for $(du/dr)_c$ at the critical point. This is obtained from equation 3.28 by using L'Hopital's rule.

$$\frac{1}{u_c}\left(\frac{du}{dr}\right)_c = \frac{N_c}{D_c} = \frac{0}{0} = \frac{(dN/dr)_c}{(dD/dr)_c}. \tag{3.34}$$

The numerator becomes

$$\left(\frac{dN}{dr}\right)_c = \frac{GM}{r_c^3} - \frac{4(u_0^2)_c}{r_c^2}\frac{T_w^2 T_c}{(T_w - T_c)^3} - \frac{2(u_0^2)_c}{r_c}\frac{T_w^2 T_c}{(T_w - T_c)^3}\frac{1}{u_c}\left(\frac{du}{dr}\right)_c \tag{3.35}$$

and the denominator becomes

$$\left(\frac{dD}{dr}\right)_c = \left(2 + \frac{T_w T_c}{(T_w - T_c)^2}\right) u_c \frac{du}{dr} + \frac{2u_c^2}{r_c^2}\frac{T_w T_c}{(T_w - T_c)^2}. \tag{3.36}$$

If we let $x \equiv u_c^{-1}(du/dr)_c$, simplify equation 3.35 to replace GM/r_c with equation 3.33, and divide out the common factor u_c^2, then equation 3.34 can be written as the quadratic equation

$$\left(2 + \frac{T_w T_c}{(T_w - T_c)^2}\right) x^2 + \frac{4}{r_c}\frac{T_w T_c}{(T_w - T_c)^2} x + \frac{4}{r_c^2}\frac{T_w T_c}{(T_w - T_c)^2} - \frac{2}{r_c^2} = 0. \tag{3.37}$$

The positive root of this equation corresponds to the accelerating flow at the critical point.

To find the mass flux loss, the first step is to guess an initial temperature at the critical point, T_c. Given T_c, we know u_0^2, p_c is given from equation 3.24, and ρ_c is given by the ideal gas law. From equations 3.32 and 3.33, we get r_c and u_c respectively, which allows us to solve equation 3.37 for the critical slope $(du/dr)_c$. Density can then be found at the new point from continuity, $\rho u r^2 = \rho_c u_c r_c^2$. Given ρ, we can solve for T and p from equation 3.24 with the help of the ideal gas equation. This integration proceeds to the surface. The guess for T_c is adjusted numerically until the desired surface temperature (in balance with incoming stellar flux and mass loss given by equation 3.21) is achieved. Once the correct values are found, equation 3.22 will give the mass loss rate.

For both isothermal and non-isothermal models, the surface temperature is assumed to be set by the incident solar flux averaged over time and hemisphere, which is given by equation 3.2 for a rapidly rotating body. The isothermal case represents the warmest possible atmosphere neglecting greenhouse effects under the case of hydrodynamic escape. The non-isothermal case represents a minimum possible temperature for a water vapor atmosphere at r_c since it is saturated at all points based on the surface temperature set from the solar flux. These two models represent the extremes of atmospheric temperature profiles for a water vapor atmosphere, with the real solution likely somewhere between them.

3.7.3 Isothermal model with greenhouse

We would like to calculate the total surface warming due to the greenhouse effect of a water vapor atmosphere considering the energy absorbed to drive atmospheric expansion and escape throughout the atmosphere. We start with the greenhouse effect of a hydrostatic atmosphere, then adapt the equation for a hydrodynamic atmosphere. We assume the atmosphere is transparent to shortwave radiation. From Catling & Kasting (2017, p. 55), for a moon with a gray, radiative, hydrostatic atmosphere the energy balance at the surface is given by

$$\sigma T_s^4 = F_{net}(1 + \tau/2) \tag{3.38}$$

where τ is the total thermal infrared optical depth of the atmosphere at the surface, σ is the Stefan-Boltzmann constant, and T_s is the surface temperature. The time-averaged, hemispherically-averaged flux incident on the moon is given by $F_{net} = (1 - A)F_s/4$ for Bond albedo A, and incident stellar flux F_s.

In our model, we are concerned with moons in the hydrodynamic regime where water vapor is lifted from the surface of the moon and accelerates upward until it escapes to space. The total energy required to remove a mass flux of water vapor from the moon's surface is given by

$$\frac{GM}{r_s}\rho_s u_s \tag{3.39}$$

for surface radius r_s. In equation 3.39, M is the mass of the moon, G is the gravitational constant, u_s is the radial outflow velocity of the atmosphere at the surface, and ρ_s is the atmospheric density at the surface, such that $\rho_s u_s$ is the mass flux in kg m^{-}2 s^{-1}.

In the hydrodynamic atmospheres of interest in this study, the energy flux needed to remove the atmosphere, given by equation 3.39, must come from the stellar radiation and the thermal IR flux. That is, it must come from the $F_{net}(1 + \tau/2)$ energy input term in equation 3.38. As such, the energy balance at the surface will then be given by

$$\sigma T_s^4 = F_{net}(1 + \tau/2) - \frac{GM}{r_s}\rho_s u_s \tag{3.40}$$

in the hydrodynamic regime. We also account for the energy required to vaporize the water mass flux at the surface, given by $L_v \rho_s u_s$ for latent heat of vaporization L_v. Subtracting $L_v \rho_s u_s$ from the right-hand side of equation 3.40 and reorganizing the terms we find the following energy balance of input and output:

$$\frac{1}{4}(1 - A)F_s\left(1 + \frac{\tau}{2}\right) = \left(\frac{GM}{r_s} + L_v\right)\rho_s u_s + \sigma T_s^4. \tag{3.41}$$

Equation 3.41 is the global energy balance at the surface for an icy moon with the greenhouse effect considered under the hydrodynamic regime. It can be compared with equation 3.2 in the main text where we assumed an atmosphere that was optically thin in the thermal infrared.

Chapter 4

ARCHEAN CARBON DIOXIDE LEVELS FROM MICROMETEORITE OXIDATION

Status

This work was published under the title *Atmospheric CO_2 levels from 2.7 billion years ago inferred from micrometeorite oxidation* by **Owen R. Lehmer, David C. Catling, Roger Buick, Donald E. Brownlee, and Sarah Newport**. It was published in *Science Advances* in **2020**. See the reference Lehmer et al. (2020).

4.1 Abstract

Earth's atmospheric composition during the Archean eon of 4 to 2.5 billion years ago has few constraints. However, the geochemistry of recently discovered iron-rich micrometeorites from 2.7 billion-year-old limestones could serve as a proxy for ancient gas concentrations. When micrometeorites entered the atmosphere, they melted and so preserved a record of atmospheric interaction. We model the motion, evaporation, and kinetic oxidation by CO_2 of micrometeorites entering a CO_2-rich atmosphere. We consider a CO_2-rich, rather than O_2-rich atmosphere, as considered previously, because this better represents likely atmospheric conditions in the anoxic Archean. Our model results reproduce the observed oxidation state of micrometeorites at 2.7 Ga for an estimated atmospheric CO_2 concentration of >70% by volume. Even if the early atmosphere was thinner than today, the elevated CO_2 level indicated by our mean model result would help resolve how the late Archean Earth remained warm when the young Sun was ~20% fainter.

4.2 Introduction

The atmospheric CO_2 concentration of the Archean Earth is highly uncertain. In the Archean, the Sun was 20-30% less luminous and CO_2 levels would have needed to be much higher than modern to maintain a climate suitable for liquid water, perhaps by a factor of 10^2 to 10^3, depending on the concentration of other greenhouse gases, such as CH_4 (e.g. Kasting, 1993; Krissansen-Totton et al., 2018a). In addition to atmospheric models, Archean paleosols and other proxies have been examined to constrain atmospheric CO_2 levels. Estimates from these studies range between $\sim 3 \times 10^{-3}$ bar and $\sim$0.75 bar of CO_2 during the Archean (see (Sec. 11.4.3 in Catling & Kasting, 2017) for a review). Thus, the estimated atmospheric CO_2 level in the Archean spans $\sim$3 orders of magnitude.

The spread in Archean atmospheric CO_2 concentrations is part of a debate about the climate of the early Earth. Isotopic analyses of phosphates (Blake et al., 2010) and deuterium (Hren et al., 2009) suggest that the Archean surface temperature was temperate and $<$40 °C. In addition, the presence of Archean glacial deposits (e.g. Wit & Furnes, 2016) indicate the early Earth was at least periodically cool. However, a high-temperature Archean with surface temperatures of 70 ± 15 °C has been proposed based on measurements of oxygen isotopes in Archean cherts (Knauth & Lowe, 2003). The possible presence of a low viscosity Archean ocean (Fralick & Carter, 2011) and the thermostability of resurrected Archean proteins (Gaucher et al., 2008) are also used for claiming a high-temperature Archean. Additional CO_2 estimates for the Archean atmosphere could help resolve this temperature uncertainty and provide insight into the conditions for life on the early Earth.

It was recently proposed that Archean, spherical, iron-rich (type I) micrometeorites could have been oxidized by modern levels of O_2 in the upper atmosphere (Tomkins et al., 2016; Rimmer et al., 2019). However, very low levels of O_2 in the Archean atmosphere inferred from a large variety of proxies (e.g. Farquhar et al., 2014) motivate considering oxidation by CO_2 as an alternative (Zahnle & Buick, 2016). Thus, the micrometeorites could provide a new constraint on Archean CO_2 levels.

When FeNi metal micrometeoroids enter the atmosphere at hypervelocity they can melt, and while molten, react readily with the surrounding atmosphere (Genge Matthew J., 2016). During this reaction, iron micrometeorites exposed to O_2 or CO_2 can oxidize some or all of the metal to species such as wüstite ($Fe_{(1\text{-}x)}O$) and magnetite (Fe_3O_4) (Genge et al., 2017). Depending on size, entry speed, and entry angle, the micrometeorites melt and oxidize in the upper atmosphere for only a few seconds at approximately 65 to 90 km above the surface for the modern Earth and solidify well before reaching the lower atmosphere. After solidifying in the upper atmosphere, iron-rich micrometeorites become largely inert and can preserve their oxidation state through geologic time (Tomkins et al., 2016).

The possibility that Archean micrometeorites could provide a proxy for atmospheric composition was first proposed by Tomkins et al. (2016). They found 59 iron-rich micrometeorites in a 2.7 billion-year-old limestone from the Pilbara region of northwestern Australia that contained magnetite, wüstite, and metallic iron. Tomkins et al. concluded that micrometeorite oxidation most likely occurred in the Earth's atmosphere and suggested that ~20% atmospheric oxygen in the upper atmosphere was responsible. They discounted CO_2 in favor of oxidation from atmospheric O_2 because of slow kinetics in low-temperature (1100 K), high-pressure (1 bar) lab measurements of oxidation of solid (and not molten) Fe by CO_2 and their equilibrium-based calculations, which implied that small, iron-rich micrometeorites would not be oxidized in a low-CO_2 atmosphere (<10% by volume). They also note that a CO_2-rich atmosphere could contain some CO, a reductant. However, such an atmosphere should also produce O_2 and O_3 (e.g. Harman et al., 2015), which could mitigate the reducing capacity of CO. In addition, Fe-rich micrometeorites melt for only a few seconds during entry and may not reach equilibrium during this time (Tomkins et al., 2016) making it premature to rule out CO_2 as a plausible oxidant.

While an oxygen rich atmosphere is certainly capable of oxidizing iron micrometeorites, an upper atmosphere of ~20% O_2 is difficult to reconcile with evidence for an anoxic atmosphere in the Archean where O_2 was likely less than 10^{-4} bar at altitude (Krull-Davatzes et al., 2010) and less than 1 ppmv at ground level (Farquhar et al., 2014, 2000; Pavlov & Kasting, 2002;

Zahnle et al., 2006). In addition to proxy data showing low atmospheric O_2 in the Archean, current understanding of atmospheric mixing does not support an O_2-rich Archean upper atmosphere with anoxic lower atmosphere. Turbulent mixing, particularly from breaking gravity waves (which physics dictates increase in amplitude with altitude) mixes the major constituents of the atmosphere up to the homopause at ∼100 km altitude on the modern Earth. Such waves are shed from airflow over surface topography, jets, and thermal tides, which are all processes that would have occurred on the ancient Earth.

The homopause is the pressure, or altitude, below which the major atmospheric constituents are well mixed due to turbulence, and on the modern Earth is well above the melting altitude for micrometeorites between roughly 65 and 90 km. It is tempting to speculate that the homopause may have occurred at a higher pressure on the Archean Earth, and thus at a lower altitude, more consistent with the melting of micrometeorites. However, a high-pressure homopause in the Archean would be physically unusual compared to all other known terrestrial atmospheres. In the Solar System, rocky bodies have homopause pressures of $\sim 10^{-2}$ Pa on Earth, $\sim 10^{-2}$ to $\sim 10^{-5}$ Pa on Mars (depending on season) (Slipski et al., 2018), $\sim 10^{-3}$ Pa on Venus, and $\sim 10^{-4}$ Pa on Titan (Catling & Kasting, 2017, p. 6). Thus, a high-pressure homopause on the Archean Earth may be counter to current understanding of atmospheric mixing and available data (see §4.3 and §4.4 of Catling & Kasting (2017) for a detailed discussion of atmospheric mixing). Even if the ground-level atmospheric pressure in the Archean were lower than modern (Som et al., 2012, 2016), the upper atmosphere would still be in approximate hydrostatic equilibrium. So, a lower ground-level pressure would not alter the absolute pressure aloft at which micrometeorites melt (Tomkins et al., 2016). An Archean model with constant vertical eddy mixing coefficient of 10^5 cm^2 s^{-1} (Rimmer et al., 2019) produces high O_2 at altitude, but the assumed eddy mixing is an order to orders of magnitude lower than that determined empirically for the upper atmosphere of the modern Earth ($\sim 10^6$ cm^2 s^{-1}) (Massie & Hunten, 1981) or required to model the thin atmosphere of Mars (e.g., 10^6 cm^2 s^{-1} at 20 km to 4×10^7 cm^2 s^{-1} at 80 km altitude) (Smith et al., 2014).

For all the above reasons, we propose a CO_2 rich atmosphere capable of oxidizing Fe micrometeorites may have been present at 2.7 Ga. A CO_2 rich atmosphere is consistent with geochemical analyses of the acid-weathering of Archean soils that became paleosols (e.g. Kanzaki & Murakami, 2015), and agrees with current models of the Archean carbon cycle and climate (Krissansen-Totton et al., 2018a), and demands no peculiar set of circumstances to create high upper atmosphere O_2 in an anoxic Archean. Furthermore, it has long been demonstrated in the metallurgy industry that CO_2 can oxidize metallic Fe under various atmospheric conditions and temperatures (e.g. Abuluwefa et al., 1997).

By modeling the motion, heating, and evaporation of micrometeorites during atmospheric entry, and using a rate constant for Fe oxidation via CO_2 from lab measurements (Smirnov, 2008) (see Section 4.3 for details), we investigate what atmospheric CO_2 levels could explain the reported oxidation of Archean micrometeorites . In this way, we seek to provide a new constraint on atmospheric CO_2 levels during the Archean.

4.3 Methods

4.3.1 Model description

This work follows the models developed by Love & Brownlee (1991) (hereafter LB) and Genge Matthew J. (2016) (hereafter MG). The LB model describes the entry and evaporation of silicate micrometeorites on the modern Earth. The MG model expands the model of LB to include Fe-rich micrometeorites and their oxidation during atmospheric entry. Below we describe our model, which is an implementation of the MG model but for oxidation of Fe by CO_2.

Following MG and LB, our model describes the motion, heating, evaporation, and oxidation of iron micrometeorites. We assume an initial velocity, v (m s^{-1}), an initial mass, m (kg), and an initial entry angle from zenith θ with $\theta = 90°$ being tangential to the Earth's surface and $\theta = 0°$ indicating the particle is moving directly toward the Earth's surface. The motion of the particle in two dimensions, accounting for atmospheric drag, can be calculated via

$$\frac{dv}{dt} = g - \frac{3\rho_a v^2}{4\rho r}\hat{v} \tag{4.1}$$

where g is gravity (m s^{-2}), v is velocity in m s^{-1}, t is time (s), ρ_a is the atmospheric density in kg m^{-3}, ρ is the density of the micrometeorite (kg m^{-3}), and r is the particle radius in m. The altitude, a, of the particle was assumed to start at 190 km above the Earth's surface, following LB, and tracked throughout the model. For a given altitude, g is easily calculated from $g = GM_{\oplus}/r_{alt}^2$ for gravitational constant $G = 6.67 \times 10^{-11}$ N m^2 kg^{-2} and Earth mass $M_{\oplus} = 5.97 \times 10^{24}$ kg; here r_{alt} is the radial distance from the center of the Earth to altitude, a. The MSIS-E-90 Atmosphere Model (available here: `https://ccmc.gsfc.nasa.gov/modelweb/models/msis_vitmo.php`) was used to generate an atmospheric density profile for the modern Earth, which we used for both the modern and Archean atmospheres following (Cnossen et al., 2007). Even if the atmospheric pressure in the Archean were lower than modern (Som et al., 2016) the density profile of the upper atmosphere generated by the MSIS-E-90 model would likely remain similar and produce similar model results, as noted by Tomkins et al. (2016).

We use the MSIS-E-90 model to generate atmospheric densities, ρ_a, and total atmospheric oxygen densities (both O and O_2) at 1 km intervals from the Earth's surface to 190 km. We linearly interpolated between each data point to find the atmospheric density for a given altitude. When calculating atmospheric CO_2 abundance in the model, we specify a CO_2 wt. %, then multiply the wt. % by ρ_a. This was done to make conversions from the MSIS-E-90 density data to CO_2 abundances a simple conversion. For example, if the model is run with 30 wt. % CO_2, the atmospheric CO_2 density will be found via $0.3\rho_a$, with ρ_a coming directly from the MSIS-E-90 data. When modelling CO_2 atmospheres, we assume the remainder of the atmosphere is N2.

With the velocity of the micrometeorite known, the heat flux of the particle, dq/dt, in W can be described by

$$\frac{dq}{dt} = \frac{\pi r^2 \rho_a v^3}{2} - L_v \frac{dm_{evap}}{dt} - 4\pi r^2 \sigma T^4 + \Delta H_{ox} \frac{dm_{ox}}{dt} \tag{4.2}$$

following equations 3 and 14 from MG. The first term on the right hand side of equation 4.2 describes the heat flux due to collisions with air, which incorporates the ram pressure, $\rho_a v^2$, experienced by the micrometeorite. The second term describes the heat flux due to evaporative mass loss with the latent heat of vaporization for both FeO and Fe given by $L_v = 6 \times 10^6$ J kg^{-1} and the mass loss given by dm_{evap}/dt in kg s^{-1}. The third term accounts for radiative heat loss with Stefan-Boltzmann constant $\sigma = 5.67 \times 10^{-8}$ W m^{-2} K^{-4} and micrometeorite temperature T in K. We assume a blackbody emissivity of unity for the radiative term, following MG. The final term describes the heat of oxidation of an Fe particle with dm_{ox}/dt being the mass growth of the oxide layer in kg s^{-1}. From MG, Fe oxidation by oxygen is exothermic with an oxidation enthalpy of $\Delta H_{ox} = 3.716 \times 10^6$ J kg^{-1}. Oxidation by CO_2 is endothermic and has an oxidation enthalpy of $\Delta H_{ox} = -4.65 \times 10^5$ J kg^{-1}.

Following MG, the ΔH_{ox} for CO_2 is approximated from the standard enthalpies of formation at standard temperature and pressure. It is estimated for the reactants and products in

$$\text{Fe} + \text{CO}_2 \rightarrow \text{FeO} + \text{CO} \tag{4.3}$$

where the energies for Fe, CO_2, FeO, and CO are 0 kJ mol^{-1}, -393.5 kJ mol^{-1} (Cox et al., 1984), -249.5 kJ mol^{-1} (Chase, 1998), and -110.5 kJ mol^{-1} (Chase, 1998) respectively. Putting these values into equation 4.3 we see that 33.5 kJ mol^{-1} are consumed in the reaction, or 4.65×10^5 J kg^{-1} of FeO. The heat of oxidation has only minor impact on the model results, so we neglect the temperature dependence of ΔH_{ox}, following MG. The ΔH_{ox} for CO_2 is an order of magnitude smaller than for O_2 in absolute value so this assumption is especially reasonable for the CO_2-rich atmosphere modelled here. It has been argued that the reaction described in equation 4.3 is the only plausible pathway of oxidation of Fe by

CO_2 under the conditions considered in this work, so we do not consider other Fe + CO_2 products (Smirnov, 2008).

The heat flux can be related to the specific heat capacity, and to temperature via

$$\frac{dq}{dt} = mc_{sp} \text{ and } \frac{dT}{dt} = \frac{dq}{dt} \cdot \frac{dT}{dq} \tag{4.4}$$

for mass m and specific heat of wüstite $c_{sp} = 400$ [J kg^{-1} K^{-1}], which coats the molten Fe micrometeorite upon entry (Stolen et al., 2015). As shown in MG, equations 4.2 and 4.4 give an equation for rate of temperature change,

$$\frac{dT}{dt} = \frac{1}{rc_{sp}\rho}\left(\frac{3\rho_a v^3}{8} - \frac{3L_v}{4\pi r^2}\frac{dm_{evap}}{dt} - 3\sigma T^4 + \frac{3\Delta H_{ox}}{4\pi r^2}\frac{dm_{ox}}{dt}\right) \tag{4.5}$$

Equation 4.5 is the same as equation 6 of MG but with the heat of oxidation term included. We note that MG is missing a 3 in the $3\sigma T^4$ term, likely due to a typesetting error.

In our model we assume that Fe is only oxidized to FeO, and do not consider further oxidation, following MG, as the process of oxidation past FeO is uncertain. As such, we only consider the ratio of unoxidized Fe to oxidized Fe in micrometeorites that are not fully oxidized in our model results. Following MG, we assume that any liquid oxide that forms during melting is immiscible with the molten Fe core and coats the exterior of the micrometeorite. Thus, we can calculate the evaporative mass loss rate, dm_{evap}/dt, by considering the rate of FeO (or Fe) evaporation using the Langmuir approximation, which is given by

$$\frac{dm_{evap}}{dt} = -4\pi r^2 p_v \sqrt{\frac{M}{2\pi R_{gas} T}} \tag{4.6}$$

where $R_{gas} = 8.314$ J mol^{-1} K^{-1} is the ideal gas constant, M is the molar mass (0.0718 kg mol^{-1} for FeO or 0.0558 kg mol^{-1} for Fe), and p_v is the vapor pressure of the evaporating FeO or Fe in Pa. The vapor pressure was determined experimentally by Wang et al. (1994) and from MG is given by

$$\log(p_v) = 10.3 - 20126/T \tag{4.7}$$

for FeO (note that equation 4.7 is the same as MG equation 13 but for units of Pa rather than dynes cm^{-2}).

In addition to evaporation of the liquid oxide layer, our model allows the unoxidized Fe to evaporate as well. This is necessary because we consider low CO_2 atmospheres where the formation of a liquid oxide layer surrounding the micrometeorite can be slower than the rate of evaporation. To handle this in our model, at each time step we calculate the oxide mass loss rate via equation 4.6 and if it exceeds the total oxide mass remaining in the particle we evaporate liquid Fe for the remainder of the time step. The liquid Fe evaporation is calculated from equation 4.6 as well, but p_v is defined by

$$\log(p_v) = 11.51 - 1963/T \tag{4.8}$$

from the data in Wang et al. (1994). Thus, the total evaporation can be given by

$$\frac{dm_{evap}}{dt} = \frac{dm_{evap\_m}}{dt} + \frac{dm_{evap\_ox}}{dt} \tag{4.9}$$

where dm_{evap_m}/dt is the metallic Fe evaporated and dm_{evap_ox}/dt is the Fe oxide evaporated via equation 4.6.

The final step is to track the mass of Fe metal, and FeO oxide in the micrometeorite. In an oxygen rich atmosphere, we assume the total oxygen accumulated by the micrometeorite is given by

$$\frac{dO}{dt} = \gamma \rho_O \pi r^2 v \tag{4.10}$$

where ρ_O is the total density of oxygen (both O and O_2) encountered in kg m^{-3}, following MG. The γ term is a dimensionless factor between 0 and 1 that determines what fraction of the encountered oxidant is used to oxidize Fe ($\gamma = 1$ in this work, see MG for a discussion of γ and O_2).

For oxidation by CO_2 we calculate the reaction rate of Fe and CO_2 from

$$r_{CO_2} = k[\mathrm{Fe}][\mathrm{CO_2}] \tag{4.11}$$

for rate constant $k = 2.9 \times 10^8 \exp(-15155/T)$ m^3 mol^{-1} s^{-1} from Smirnov (2008) with r_{CO_2} in mol m^{-3} s^{-1}. The Fe concentration is given by

$$[\mathrm{Fe}] = \frac{m_{Fe}}{V} \tag{4.12}$$

where m_{Fe} is the mass of Fe in the micrometeorite in mol, and V is the volume of the micrometeorite in m^3. The CO_2 concentration per unit volume is given by the total CO_2 encountered per second multiplied by the timestep, Δt, i.e.

$$[\mathrm{CO}]_2 = \frac{\gamma \rho_{CO_2} \pi r^2 v}{V} \Delta t \tag{4.13}$$

where ρ_{CO_2} is in mol m^{-3}. We compare the rate in equation 4.11 to the total CO_2 encountered per unit volume per time step and take the lesser of the two as the amount of oxygen accumulated by the Fe. We assume $\gamma = 1$ in equation 4.13 so the oxidation from CO_2 calculated with this model should be considered an upper bound. From equation 4.3, each CO_2 that reacts with the micrometeorite will add one O to the particle as FeO so

$$\frac{dO}{dt} = V \cdot \min\left(\frac{[\mathrm{CO_2}]}{\Delta t}, r_{CO_2}\right). \tag{4.14}$$

When calculating dO/dt for CO_2 we first calculate in mol s^{-1}, then convert to kg s^{-1} for ease of use in the model.

It is important to note that the reaction rate for Fe oxidation via CO_2 used in this model was derived from lab measurements of gas-phase interactions of Fe and CO_2 (Smirnov, 2008). This likely represents an upper bound on Fe oxidation via CO_2 and may overestimate the oxidation of liquid Fe in a CO_2-rich atmosphere, where diffusion of the oxidant through the liquid Fe oxide could be the rate limiting step. However, the kinetics of the reaction for the pressures and temperatures considered in this model are uncertain (noting that temperatures often exceed ~2000 K). As such, the model presented here should be considered an upper bound on the oxidation rate by CO_2. Future lab measurements are desirable to constrain the reaction rate described by equation 4.11.

Following MG, our model only allows oxidation while unoxidized Fe remains in the micrometeorites. Thus, one Fe atom will be removed from the metallic Fe mass for each O atom accumulated. The total metallic Fe in the particle at each time step is then calculated by the amount of Fe converted to Fe oxide, minus evaporated Fe, giving an equation for the mass of metallic Fe in the particle

$$\frac{dm_m}{dt} = -\frac{M_{Fe}}{M_O}\frac{dO}{dt} - \frac{dm_{evap\_m}}{dt} \tag{4.15}$$

for Fe molar mass $M_{Fe} = 0.0558$ kg mol^{-1} and atomic O molar mass $M_O = 0.0160$ kg mol^{-1}. Similarly, the mass of oxide will grow for each O atom encountered, minus the evaporated FeO, which can be described by

$$\frac{dm_{ox}}{dt} = \frac{M_{FeO}}{M_O}\frac{dO}{dt} - \frac{dm_{evap\_ox}}{dt}. \tag{4.16}$$

With initial altitude, velocity, and mass known, equations 4.1, 4.5, 4.9, 4.15, and 4.16 can be solved numerically to simulate the entry of an Fe micrometeorite. We assume all particles start as pure Fe and use a simple Euler approximation to numerically integrate the equations. We set the maximum timestep to 0.01 seconds for our integration but allow the timestep to adjust dynamically such that the maximum change in temperature of the particle never exceeds 0.1%. Following MG, we assume that no oxidation occurs until the micrometeorite melts at 1809 K for Fe and oxidation shuts off when the micrometeorite solidifies at 1720 K (the FeO melting temperature). We assume the liquid FeO has a density of 4400 kg m^{-3}, and Fe has a density of 7000 kg m^{-3}, from MG. In addition, for Fe we use a specific heat of 400 J K^{-1} kg^{-1}. Figure 4.1 shows an example model run for a single 50 μm particle entering a 50 wt.% CO_2, 50 wt.% N_2 atmosphere at 12 km s^{-1} and an entry angle of 45° from the Zenith.

Of interest in our model is the fractional area of unoxidized Fe compared to the total

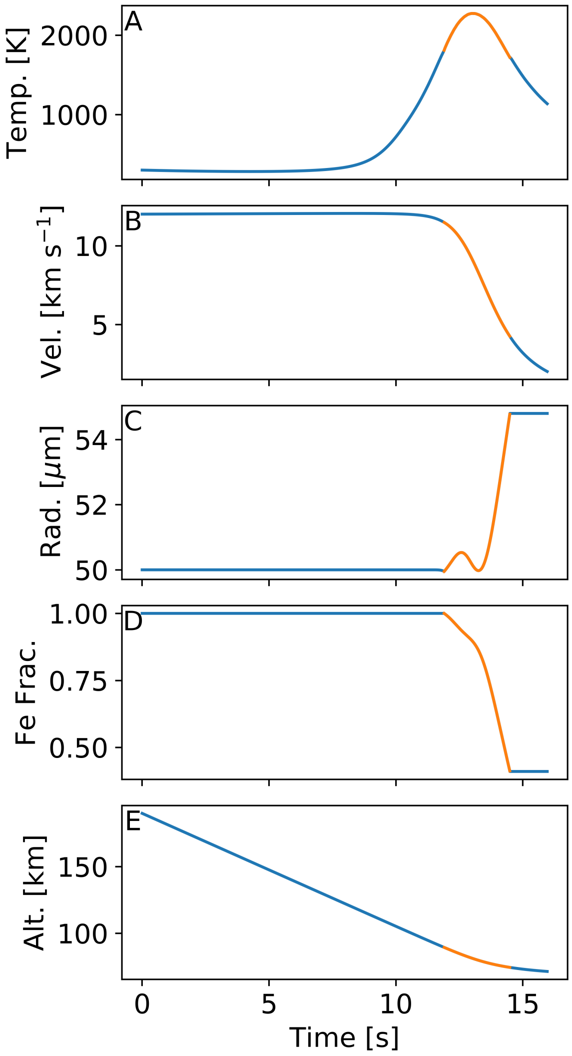

Figure 4.1: Single model run for a particle with an entry angle of 45° from zenith run through a 39% CO_2, 61% N_2 atmosphere (50 wt.% CO_2, 50 wt.% N_2). The plots above show: (A) micrometeorite temperature in K, (B) micrometeorite velocity in km s^{-1}, (C) micrometeorite radius in μm, (D) the mass fraction of metallic Fe to oxidized FeO, and (E) the micrometeorite's altitude above the Earth's surface in km. The orange part of each curve indicates the micrometeorite is molten. For plot C, the micrometeorite increases in radius because the oxide layer is growing faster than it is evaporating. The oxidation of high-density Fe to the lower density FeO results in a less dense particle and thus a larger radius. In this simulation, the micrometeorite is molten for 2.6 seconds between 11.9 and 14.5 seconds. The initial radius is 50 μm, the final radius is 54.8 μm, the final Fe fractional mass is 41% (37% by cross-sectional area), and the maximum temperature reached is 2275 K at an altitude of 81.2 km.

cross-sectional area of the micrometeorite (i.e. unoxidized Fe plus oxidized Fe) after they solidify. For a given micrometeorite, we assume that the unoxidized Fe forms a spherical bead at the center of the particle and is evenly surrounded by any produced oxide (FeO). We then "section" the simulated micrometeorites at the midpoint and compare the total surface area of exposed metallic Fe to the total area of the sectioned micrometeorite. This quantity can be easily compared to measurements like those in Figure 4 of Genge et al. (2017), which reports Fe phase abundance in sectioned micrometeorites. Our assumption that the metallic Fe is centered in the micrometeorite means we assume an upper bound on the sectioned area, as an uncentered bead may not measure Fe at the widest point. Despite this assumption, our model is able to accurately reproduce the data reported in Figure 4 of Genge et al. (2017), which shows the ratio of metallic Fe to oxidized Fe for 34 modern micrometeorites collected from Antarctica (we consider both FeO and Fe_3O_4 as oxides here and do not differentiate between them). Note, in Genge et al. (2017) the captions of Figures 4 and 5 are switched so the interested reader should look at the data presented in Figure 4, but apply the caption of Figure 5 to avoid confusion. Figure 4.2 in this paper shows our model prediction of Fe fractional area compared to the data inferred from Figure 4 of Genge et al. (2017). The agreement between our simulated data (blue) and the modern micrometeorite collected data (orange) is clearly shown in the figure.

Following MG, we do not consider magnetite formation in our model because the process by which magnetite forms during entry is uncertain. The liquid Fe oxide that forms while the micrometeorite is molten could crystalize as Fe_3O_4 if enough oxygen is accumulated while molten. However, magnetite may also form after solidification due to decomposition of FeO to Fe_3O_4 or possibly from further oxidation at low temperatures. In addition, the central Fe bead could separate from the molten micrometeorite during entry leading to a highly oxidized melt as a remainder, which could solidify as magnetite (see MG for a discussion of Fe_3O_4 formation). Thus, we only consider micrometeorites that still retain unoxidized Fe in both our model results and collected data and do not differentiate between the phases of oxidized Fe.

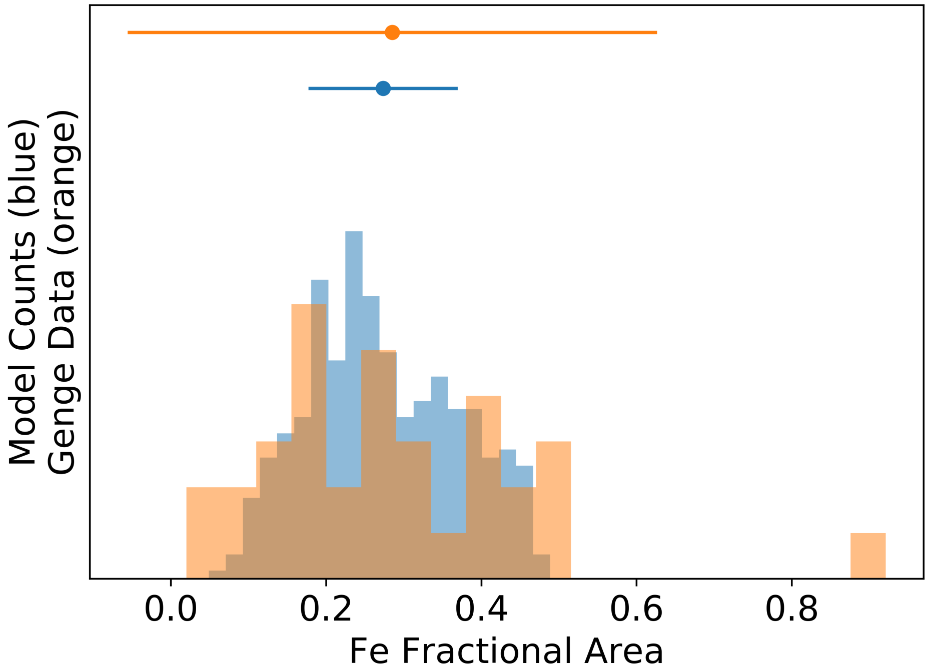

Figure 4.2: Fractional area of unoxidized Fe in simulated sectioned micrometeorites compared to observed modern micrometeorites. The horizontal axis in this plot shows the fractional area of unoxidized Fe in cross-sectioned micrometeorites. The blue histogram shows the simulated unoxidized Fe fractional area from 500 randomly generated micrometeorites entering the modern atmosphere, which were oxidized by O_2, and the orange histogram shows the data inferred from Figure 4 of Genge et al. (2017). The model mean and 2σ confidence interval is shown by the blue dot and error bar, while the mean and 2σ of the data from Genge et al. is shown by the orange dot and error bar.

When calculating our simulated micrometeorite areas, we impose several conditions on the final particle. First, we do not consider simulated particles that are smaller than 2 μm in final radius. Despite the abundance of such small particles, they are not easily found when extracting micrometeorites from sedimentary rocks given their small size, so we do not consider them to better represent collected data. Indeed, the smallest micrometeorite found by Tomkins et al. was $\sim$4 μm in radius. And second, we do not consider fully oxidized or unoxidized micrometeorites (i.e. pure FeO or pure Fe). This is done as pure Fe micrometeorites only exist in our model because they enter the atmosphere slow enough, or with a shallow enough angle that they do not reach the Fe melting temperature. These unmelted micrometeorites represent a fixed feature in the model data that cannot inform of atmospheric composition. Pure FeO micrometeorites represent the limit of our model calculations so, aside from showing their production is expected from the model, are not considered when calculating the mean Fe fractional area (black/orange lines in Figure 4.3 and Figure 4.4). Neglecting these edge cases does not hinder our ability to reproduce modern micrometeorite data (Figure 4.2) since we exclude fully oxidized micrometeorites from the collected data as well, ensuring our data sets are comparable.

To validate our model for the modern Earth, we simulated 500 micrometeorites entering the modern Earth's O_2-rich atmosphere. We compare the fractional unoxidized metallic Fe area of modeled micrometeorites to that of micrometeorites collected from Antarctica (Genge et al., 2017). The results of this comparison are shown in Figure 4.2, with our simulated micrometeorites shown in blue and the modern micrometeorite data shown in orange. Our model is only defined while metallic Fe remains in the micrometeorites, so we compare only partially oxidized micrometeorites from both the data and our model. The agreement of the model mean and the data mean from Genge et al. (2017) (Figure 4.2) indicates that our model can predict the Fe fractional area in modern micrometeorites entering Earth's O_2-rich atmosphere.

4.3.2 Initial micrometeorite distributions

Using the model described above, we randomly generated micrometeorites from initial mass, velocity, and impact angle distributions. These distributions are described in detail in Love & Brownlee (1991) and summarized below. For the initial impact angle, values between 0° and 90° are valid. The fraction of particles with impact angle θ between θ_1 and θ_2 is given by $n(\theta_1, \theta_2) = \sin^2 \theta_2 - \sin^2 \theta_1$. The equivalent probability density function for θ is given by

$$P(\theta) = \sin(2\theta),\ 0^\circ < \theta < 90^\circ \tag{4.17}$$

which we use to randomly sample initial impact angles in this work. In our simulations, micrometeorites with initial impact angles greater than ~83° could "skip" off the top of the atmosphere. We stopped the simulation on such particles as soon as they began moving away from the Earth to avoid long computation times. Only particles that continued into the atmosphere upon contact were calculated. Micrometeorites with initial angles greater than 83° represent less than 1.5% of the distribution, so the impact of neglecting such particles is likely small.

The initial velocity distribution is defined by $\lambda(\nu, \nu + d\nu) = 1.791 \times 10^5 v^{-5.394} dv$ for velocity, v, in km s^{-1}. The probability density function for v is then given by

$$P(v) = 1.791 \times 10^5 v^{-5.394} \tag{4.18}$$

for $v > 11.2$ km s^{-1}. In this work we only consider initial velocities up to 20 km s^{-1}. Initial velocities between 11.2 and 20 km s^{-1} represent over 92% of the distribution and is similar to the velocity limits used by both MG and LB. Micrometeorites entering the atmosphere faster than 20 km s^{-1} require an increasingly small timestep to avoid numerical errors, which is detrimental to the overall runtime of the simulation. As such, we neglect unusual micrometeorites with velocities greater than 20 km s^{-1} and expect it should have little bearing on our final results.

The initial mass distribution of the cumulative number of particles of mass greater than m per square meter per second is defined by

$$F(m) = (2.2 \times 10^3 m^{0.306} + 15)^{-4.38} + 1.3 \times 10^{-9}(m + 10^{11}m^2 + 10^{27}m^4)^{-0.36}. \tag{4.19}$$

This function is defined at 1 AU for particles greater than ~10^{-14} g. We only consider masses between 2.346×10^{-9} g and 2.932×10^{-2} g, which corresponds to initial Fe particle radii of 2 μm, and 1000 μm, respectively. The collected micrometeorites we compare to were all greater than 2 μm in radius, which is how we set the lower limit. Our model assumes that the micrometeorite radius is less than its mean free path in the upper atmosphere, which is only true for small particles. At 1000 μm radius, this assumption becomes less reasonable and such large particles could develop a bow shock, which we do not consider. As such, our simulation of the largest particles ($\geq$1000 μm radius) is uncertain. Fortunately, over 95% of the mass distribution results in particles with radii under 500 μm. Following Love & Brownlee (1991), we normalize the above mass distribution between the mass range of interest to find the probability density function

$$P(m) = \frac{(2.2 \times 10^3 m^{0.306} + 15)^{-4.38} + 1.3 \times 10^{-9}(m + 10^{11} m^2 + 10^{27} m^4)^{-0.36}}{4.59811 \times 10^{-13}} \tag{4.20}$$

for mass m in grams.

4.4 Results

We model 15,000 randomly generated micrometeorites entering a 1 bar N_2-CO_2 atmosphere with CO_2 concentrations between ~2% and ~85% by volume (3 wt. % to 90 wt. %). We assume that all particles start as pure Fe upon entry. Our model tracks the motion, oxidation, and evaporation of each particle along with its composition throughout its descent in the atmosphere. We look at the cross section of each simulated micrometeorite and compare the total area of unoxidized Fe to the total cross-sectional area of the particle (i.e. oxidized Fe area plus unoxidized Fe area). We chose to measure cross-sectional area to make empirical micrometeorite data readily comparable to our model results. Figure 4.1 shows an example of our model for a single micrometeorite entering a 39% CO_2, 61% N_2 atmosphere.

The atmosphere of the Archean was O_2-poor (e.g. Lyons et al., 2014). However, photochemical models of Earth-like planets around Sun-like stars indicate that minor atmospheric O_2 could be sustained photochemically in the upper atmosphere via CO_2 photolysis. From such models, the O_2 level in the upper atmosphere could reach ~1% by volume in a high

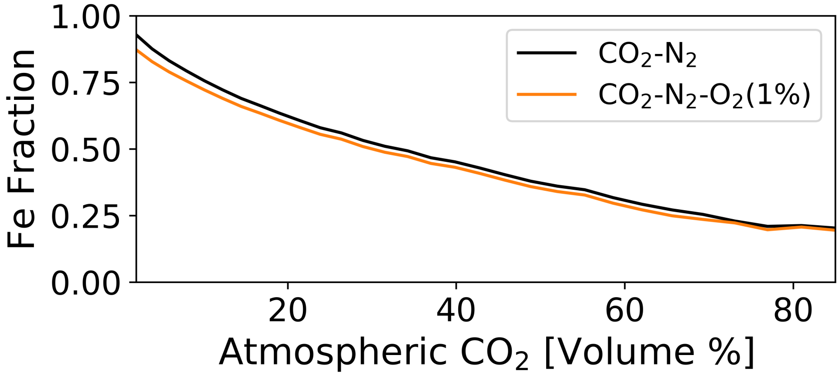

Figure 4.3: Comparison of unoxidized Fe area in CO_2-N_2 and CO_2-N_2-O_2 atmospheres with increasing CO_2. The black curve shows the mean model cross-sectional area of unoxidized Fe compared to the total cross-sectional area of the micrometeorite for a CO_2-N_2 atmosphere. It is the same curve as in Figure 4.4. The orange contour shows the same simulated micrometeorites but entering a CO_2-N_2-O_2 atmosphere where the O_2 represents 1% by volume. The addition of 1% O_2 to the atmosphere has little impact on the average Fe fractional area.

(90% by volume) CO_2 atmosphere, while remaining a trace gas at the planetary surface (Harman et al., 2015). This O_2 concentration is well below the modern levels required to explain the oxidation of Archean micrometeorites (Tomkins et al., 2016).

To address the possibility of oxidation by major CO_2 and minor O_2 in the Archean we ran our model with a CO_2-N_2-O_2 atmosphere. Each of the 15,000 modeled micrometeorites were simulated entering both a CO_2-N_2 only atmosphere and a CO_2-N_2-O_2(1%) atmosphere. As an upper bound, the atmospheric O_2 was fixed at 1% and did not decrease with altitude in the altitude range for micrometeorite melting. The results of both runs are shown in Figure 4.3. The black curve in Figure 4.3 shows the mean unoxidized Fe fractional area in our modeled micrometeorites as atmospheric CO_2 increases for the CO_2-N_2 atmosphere while the orange curve shows the same for micrometeorites entering the CO_2-N_2-O_2(1%) atmosphere. The difference in final Fe fractional area between the two atmospheres is negligible, especially at high CO_2 concentrations, showing that CO_2 dominates as the oxidant when O_2 is ∼1% or

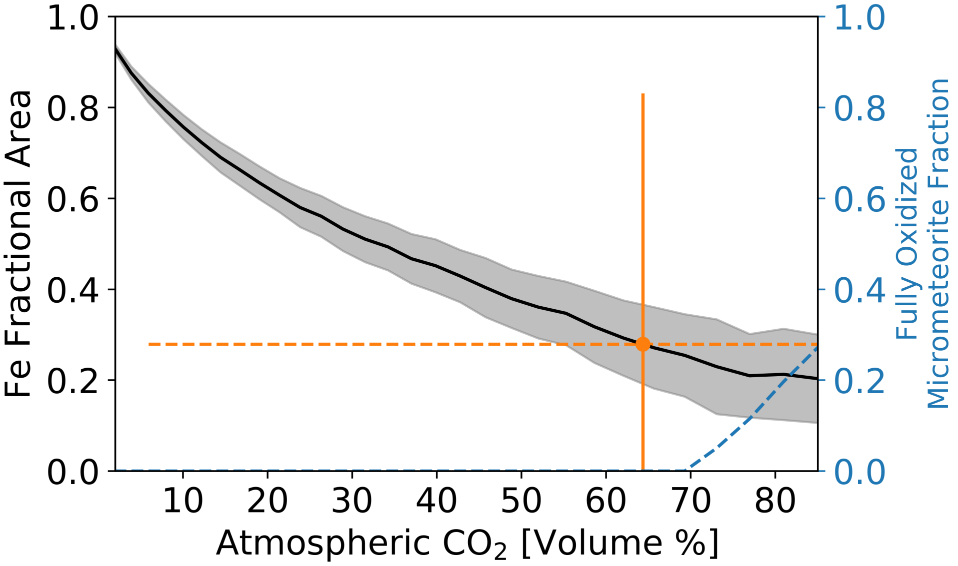

Figure 4.4: Simulated fractional area of unoxidized Fe with increasing atmospheric CO_2. The atmosphere was assumed to be composed of pure N_2 and CO_2. The black curve shows the mean model prediction for the cross-sectional area of unoxidized Fe compared to the total cross-sectional area of the micrometeorite. The simulated micrometeorites were assumed to have spherical, central metal beads so the cross-sectional area of the unoxidized Fe bead is a maximum. The grey shaded area shows the 2σ confidence interval of our model. The orange dot and solid error bar show the mean unoxidized Fe fractional area and 2σ confidence interval from the two Fe-FeO micrometeorites reported by Tomkins et al. (2016). The corresponding uncertainty in atmospheric CO_2 from the Tomkins et al. data is shown by the dashed orange error bars. The Tomkins et al. data point indicates the CO_2 level was at $64^{+36}_{-58}\%$ (2σ). The dashed blue line shows the fraction of modeled micrometeorites that that were fully oxidized in the atmosphere with no remaining metallic Fe. Such particles could lead to magnetite rich micrometeorites and appear in our model once atmospheric CO_2 reaches $\sim$70%.

lower.

The Archean CO_2 estimates from the modeling are shown in Figure 4.4 (the black line of Figure 4.4 is the same as in Figure 4.3). On average, we find that the unoxidized Fe fractional area of sectioned micrometeorites decreases monotonically as atmospheric CO_2 concentrations increase. The solid black curve in Figure 4.4 shows the mean unoxidized Fe area in our modelled micrometeorites as atmospheric CO_2 increases. The grey shaded region is the model 2σ uncertainty arising from uncertainties in initial mass, velocity, and impact angle (see Section 4.3.2). The orange dot and error bar show the mean fractional Fe area measured by Tomkins et al.

From the black curve in Figure 4.4, we estimate an Archean CO_2 volume mixing ratio of $64^{+36}_{-58}\%$ (2σ) given the data from Tomkins et al. (orange dot and error bar in Figure 4.4). The uncertainty is large because of the paucity of Archean micrometeorite data: only two data points are available with metallic Fe fractional areas of 0.555 and 0.003 respectively (inferred from Tomkins et al. Figure 1e and 1f).

Some fully oxidized micrometeorites collected by Tomkins et al. indicate high CO_2 levels were likely present during entry. Our model predicts that fully oxidized micrometeorites will only form when atmospheric CO_2 concentrations exceed ∼70% by volume, as indicated by the dashed blue curve in Figure 4.4. As such, while our CO_2 estimate spans 6% to 100% (2σ), the CO_2 concentration likely falls above ∼70% given the presence of some fully oxidized micrometeorites in the Tomkins et al. data. This agrees with Archean paleosols and climate models of the Archean Earth, which suggest CO_2 levels on the Archean were substantially higher than modern. If the Archean Earth had a 1 bar atmosphere, our estimate of $>70\%$ CO_2 by volume indicates the partial pressure of CO_2 would be >0.7 bar in the Archean. However, surface pressure may have been much lower during the Archean, perhaps just 0.23 ± 0.23 bar (2σ) (Som et al., 2016). With a mean surface pressure of 0.23 ± 0.23 bar, our model predicts a CO_2 partial pressure of $> 0.16 \pm 0.16$ bar (2σ). Provided some methane were present, such as 0.5% (Zahnle et al., 2019), this thin, CO_2-rich atmosphere could provide enough greenhouse warming to sustain liquid water under a faint young Sun (e.g. Stüeken et al., 2016). Atmospheric methane would warm the surface during the Archean as a greenhouse gas but is not expected to interact with molten, Fe-rich micrometeorites (Tomkins et al., 2016) and thus should not alter their oxidation state.

In our model, the oxidation of micrometeorites in the upper atmosphere is not impacted by the atmospheric surface pressure. Reducing the surface pressure would move the altitude at which micrometeorites oxidize closer to the surface (slightly altering the gravitational acceleration experienced by melting micrometeorites), but the overall pressures at which melting occurs do not appreciably change nor do our results. The difference in model results between a 1 bar atmosphere and 0.23 bar atmosphere is negligible, which agrees with the findings of Tomkins et al.

4.5 Discussion

Our model shows that 2.7 billion-year-old micrometeorites (Tomkins et al., 2016) could have been oxidized by CO_2 in a CO_2-rich atmosphere. While our estimated CO_2 abundance of $64^{+36}_{-58}\%$ (2σ) has large uncertainties, collection and analysis of additional Archean micrometeorites could greatly reduce the spread in this estimate. Using the parameterized climate model described in (Krissansen-Totton et al., 2018a), ∼70% CO_2 for the Archean atmosphere, and an upper bound on Archean surface pressure of ∼0.5 bar (Som et al., 2016), the global mean surface temperature in the Archean would be ∼30 °C (or lower for lower total pressure), indicating a temperate Archean climate. An improved Archean CO_2 measurement would allow more robust climate models to further refine the surface temperature of the Archean Earth and the conditions, including pH of surface waters, in which early life evolved. Not only would this help address the hot vs. temperate Archean debate, but it could also inform our understanding of Earth-like exoplanets and their potential habitability (e.g. Arney et al., 2016).

The uncertainty in our model output (grey shaded region in Figure 4.4) is more difficult to reduce. This uncertainty stems from the random sampling of our initial parameter distributions for mass, velocity, and entry angle, which have some inherent uncertainty on the modern Earth (see Section 4.3.2). Despite such uncertainties, our model can reasonably predict the Fe fractional area in modern micrometeorites entering an O_2-rich atmosphere (e.g. Figure 4.2).

The conclusion that a CO_2-rich atmosphere can oxidize Fe micrometeorites is a reasonable alternative to oxidation via the O_2-rich Archean atmospheres considered previously

(Tomkins et al., 2016; Rimmer et al., 2019). As demonstrated by the metallurgy industry (e.g. Abuluwefa et al., 1997) and other lab measurements (Smirnov, 2008), CO_2 can readily oxidize Fe, albeit less efficiently than O_2. While we do not model oxidation past FeO, further oxidation is not precluded by our model as the oxide that forms during entry is a liquid Fe melt with dissolved oxygen (see Genge Matthew J. (2016) for a discussion). If the melt acquires more O than Fe it could solidify as Fe_3O_4 rather than FeO. However, additional lab measurements of molten Fe beads quenching in simulated CO_2-rich atmospheres are necessary to understand how CO_2 oxidizes Fe liquids at high temperatures.

Our model results in Figure 4.4 show that a >70% by volume CO_2 atmosphere could fully oxidize micrometeorites and possibly produce magnetite. This is seen by the dashed blue line in Figure 4.4, which shows the fraction of the total simulated micrometeorites that are fully oxidized after entry as a function of atmospheric CO_2 abundance. Our simulation stops when a micrometeorite has no remaining unoxidized Fe, but such a micrometeorite encountering additional CO_2 could continue to oxidize past FeO, possibly to Fe_3O_4 (see Section 4.3).

In addition to showing that atmospheric CO_2 could explain the observed, oxidized Archean micrometeorites, our model predicts that the average unoxidized Fe remaining in collected micrometeorites should decrease with increasing atmospheric CO_2. From this relationship, it may be possible to constrain atmospheric CO_2 concentrations not only in the Archean, but in the Proterozoic as well when atmospheric oxygen was scarce. Indeed, our CO_2-N_2-O_2 atmosphere with 1% O_2 in the upper atmosphere could be representative of the Proterozoic atmosphere (Lyons et al., 2014) in which micrometeorite oxidation would still be dominated by CO_2, as seen in Figure 4.3 (orange curve). Numerous iron-rich micrometeorites have been found in Proterozoic rocks (Tianrui et al., 2007) and measuring the fractional area of unoxidized Fe in such samples could readily be done. Such measurements might provide a constraint on atmospheric CO_2 at that time.

The CO_2 concentration of the atmosphere is thought to have decreased over Earth's history (e.g. Krissansen-Totton et al., 2018a) from a major atmospheric constituent in the Archean to a few hundred parts per million today. If we compare that trend to the black curve in Figure 4.4, we see that our model predicts the fractional area of unoxidized Fe in collected micrometeorites should increase with time – if the trend depends just on CO_2 oxidation – from the Archean until the end of the Neoproterozoic, albeit with some uncertainty due to a possible O_2 overshoot during the Great Oxidation Event. Oxidation by O_2 might remain minor during the Proterozoic because the ground-level atmospheric O_2 may have been $\sim$0.2% absolute concentration or less (Lyons et al., 2014) so the trend could hold (Figure 4.3, orange curve). To verify this hypothesis, additional micrometeorites should be collected and analyzed.

Chapter 5

CARBON DIOXIDE IN THE HABITABLE ZONE

Status

This work is currently in review at *Nature Communications* under the title *Climate on Earth-like Exoplanets around Sun-like Stars: How Carbonate-Silicate Cycle Predictions Modify the Habitable Zone Hypothesis and Allow for its Testing* by **Owen R. Lehmer, David C. Catling, and Joshua Krissansen-Totton**.

5.1 Abstract

In the conventional habitable zone (HZ) concept, a CO_2-H_2O greenhouse effect maintains surface liquid water. Through the water-mediated carbonate-silicate weathering cycle, atmospheric CO_2 partial pressure (pCO_2) adjusts in response to changes in surface temperature, stabilizing the climate over geologic timescales. This weathering feedback has been assumed to maintain temperate, or even constant surface temperatures for Earth-like planets within the HZ. Here we show that if Earth-like, carbonate-silicate weathering feedbacks moderate climate, then a temperate or constant temperature across the HZ may be a misconception. Instead, temperature decreases with orbital distance for a fixed volcanic outgassing. A power law dependence on pCO_2 in the weathering sink of carbon can balance outgassing at lower surface temperatures in the outer HZ. Also, we predict a log-linear relationship between pCO_2 and incident flux for Earth-like planets within the HZ in contrast to a temperate or constant temperature assumption. However, this trend of pCO_2 with incident flux has scatter because geophysical and physicochemical parameters can vary, such as land area for weathering, rock dissolution rates, and CO_2 outgassing fluxes. Using a coupled climate and carbonate-silicate weathering model, we quantify the likely spread of pCO_2 with orbital dis-

tance in the HZ. Given this dispersion, future observations would need to characterize at least 6 Earth-like exoplanet atmospheres in the HZ to achieve 95% confidence in detecting a positive relationship between decreasing incident flux and pCO_2. Such observations would test the validity of our revised HZ hypothesis.

5.2 *Intruduction*

Newton first alluded to the concept of a stellar habitable zone (HZ) in his 1687 *Principia* by noting that Earth's liquid water would vaporize or freeze at the orbits of Mercury and Saturn, respectively (see the translation Cohen et al., 1999, p. 814). Later, Whewell (1853, p.196) noted that "the Earth's orbit is in the temperate zone of the Solar System". Since then, the definition of the stellar HZ has been refined, reaching its modern incarnation based on climate models (Kasting, 1993) (see Catling & Kasting (2017) §15.1.2 for further review of the HZ).

Current HZ calculations find that around a Sun-like star, an Earth-like planet could remain habitable between 0.97 and 1.70 AU (Kopparapu et al., 2013). The inner edge of the HZ is set by loss of surface water and the outer edge is set by the "maximum greenhouse" of a CO_2 atmosphere where extensive CO_2 condensation and increased Rayleigh scattering prevent any further greenhouse warming from CO_2 (e.g. Kasting et al., 1993; Kopparapu et al., 2013). This definition of the HZ only considers H_2O and CO_2 as greenhouse gases, so Earth-like planets warmed by other greenhouse gases (e.g. H_2 or CH_4) could remain habitable at bigger orbital distances (e.g. Stevenson, 1999; Seager, 2013; Catling & Kasting, 2017, §15.1.3). However, CH_4-rich atmospheres in the HZ may not be possible without life to generate substantial CH_4 (Krissansen-Totton et al., 2018b). In addition, more complex climate models have shown the HZ might extend to smaller orbital distances, perhaps interior to Venus' orbit, with appropriate planetary conditions (e.g. Abe et al., 2011; Zsom et al., 2013; Yang et al., 2014).

Residing within the HZ does not guarantee habitable surface conditions. Crucially, greenhouse gas abundances (and planetary albedo) must conspire to produce clement surface conditions. For example, by most estimates, Mars resides within the Sun's HZ but is not habitable because there is insufficient greenhouse warming from CO_2, in part because of the lack of volcanic outgassing of CO_2. What, then, controls the CO_2 abundance and therefore the habitability of Earth-like planets within the habitable zone?

The prevailing hypothesis, first outlined by Walker et al. (1981), is that CO_2 levels are controlled by a weathering thermostat. This can explain why Earth has maintained a clement surface throughout its history despite the ∼30% brightening of the Sun over the past ∼4.5 Gyr (Krissansen-Totton et al., 2018a; Sleep & Zahnle, 2001; Sagan & Mullen, 1972). The changing luminosity of the Sun with time is similar to moving a planet through the HZ, and so the same CO_2 weathering process responsible for maintaining habitability on the Earth through time, the carbonate-silicate weathering cycle, may similarly stabilize planetary climates within the HZ.

In the carbonate-silicate cycle, atmospheric CO_2 dissolves in water and weathers silicates on both the continents and seafloor, which releases cations and anions (Walker et al., 1981; Walker, 1993; Berner, 2004; Mills et al., 2014; Krissansen-Totton & Catling, 2017). On the continents, the weathering products, including dissolved SiO_2, HCO_3^-, and Ca^{++}, wash into the oceans where the ${HCO_3}^-$ combines with cations like Ca^{++} to create $CaCO_3$, which precipitates out of solution. The net process converts atmospheric CO_2 into marine carbonate minerals (i.e., $CaCO_3$). Also, seafloor weathering occurs when seawater releases Ca^{++} ions from the seafloor basalt and $CaCO_3$ precipitates in pores and veins. Subsequently, the carbonates within sediments and altered seafloor can be subducted.

Carbon returns to the atmosphere from outgassing. CO_2 outgassing raises a planet's surface temperature, which leads to increased rainfall and continental weathering as well as potentially warmer deep sea temperatures and more seafloor weathering (Krissansen-Totton et al., 2018a; Berner, 2004; Coogan & Dosso, 2015). Increased weathering draws down atmospheric CO_2 and stabilizes the climate over $\sim 10^6$-year timescales on habitable, Earth-like planets (e.g. Kadoya & Tajika, 2014).

Climate calculations of HZ limits (e.g. Kasting, 1993; Kopparapu et al., 2013; Yang et al., 2014) assume that a carbonate-silicate weathering cycle is functioning but do not explicitly include it. The assumed presence of the carbonate-silicate cycle would predict that atmospheric CO_2 of Earth-like planets increases with orbital distance in the HZ (e.g. Kasting, 1993; Kopparapu et al., 2013; Kadoya & Tajika, 2014). In particular, future telescopic observations (e.g. NASA's HabEx and LUVOIR) could search for the CO_2 trend to test the HZ hypothesis (Bean et al., 2017; Checlair et al., 2019; Turbet, 2019). Previous studies (e.g. Abbot et al., 2012; Kadoya & Tajika, 2014) have suggested the carbonate-silicate weathering cycle could alter predictions of pCO_2 in the HZ, but it is important to know the exact trend we are looking for. Also, while an increase of pCO_2 with orbital distance in the HZ may be true if all Earth-like exoplanets have the exact same properties as the modern Earth, the trend becomes less certain if HZ planetary characteristics deviate from those of the modern Earth. There could be considerable variability in atmospheric CO_2 throughout the HZ, perhaps even enough to obscure a monotonic trend with orbital distance.

Here, we first examine the theory of how the carbonate-silicate weathering cycle (Krissansen-Totton & Catling, 2017, and references therein) defines a trend of surface temperatures and atmospheric pCO_2 for Earth-like planets in the HZ. Then we model how uncertain physico-chemical and geophysical parameters in the cycle cause scatter in pCO_2 with orbital distance. Finally, we consider the number of HZ planetary atmospheres that future telescopes must observe to confidently detect our predicted trend between atmospheric CO_2 and orbital distance in the HZ.

5.3 Habitable zone climate theory revisited

A conventional assumption is that the carbonate-silicate weathering cycle will approximately maintain a stable, temperate surface temperature for an Earth-like planet moved about in the HZ (e.g. Kasting & Toon, 1989; Kasting et al., 1993; Kopparapu et al., 2013) or even a constant temperature (e.g. Bean et al., 2017; Turbet, 2019). Thus, if we moved the modern Earth outward in the HZ, the smaller incident flux would initially cause the planet to cool. The cooler temperature would lower the CO_2 weathering rate causing CO_2 to accumulate

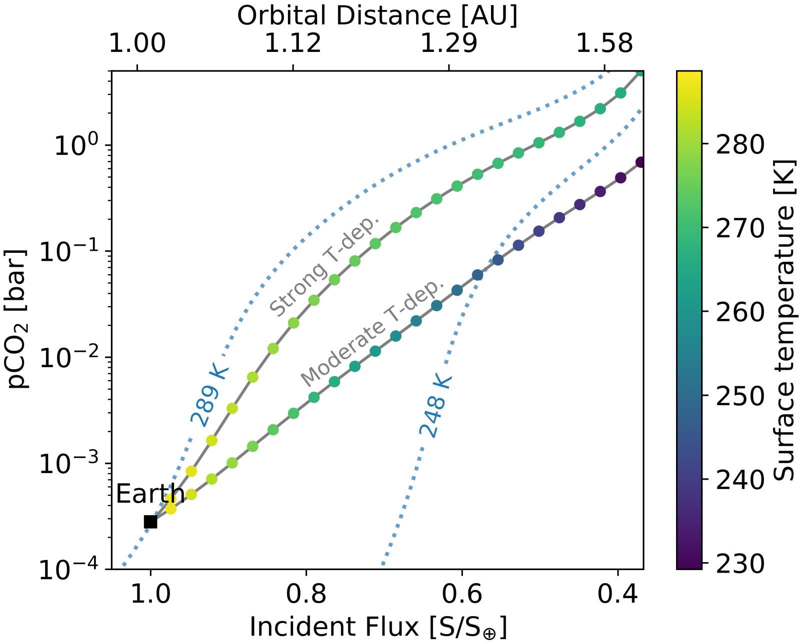

Figure 5.1: The relationship between incident flux and atmospheric CO_2 for Earth-like planets regulated by a carbonate-silicate weathering cycle. The horizontal axis shows incident flux, S, normalized to the solar constant ($S_\oplus$) and the corresponding orbital distance in Astronomical Units (AU) above the plot. The vertical axis shows the atmospheric CO_2 partial pressure (pCO_2) in bar. The dotted blue curve labelled '289 K' shows the pCO_2 value required to maintain a 289 K surface temperature for the given incident flux, S. The dotted blue contour labelled '248 K' shows a similar temperature contour but for a 248 K mean surface temperature. The conventional assumption of CO_2 in the HZ stipulates that pCO_2 will adjust to maintain a temperate or even constant surface temperature. Under this assumption, moving the modern Earth (labelled black square) outward in the HZ would have the planet approximately follow the dotted blue 289 K contour. The colored points and gray curves show the modern Earth moving outward in the HZ with a functioning carbonate-silicate weathering cycle, calculated from equation 5.6. We consider two temperature and pCO_2 dependencies for continental weathering in this plot. The strong temperature dependence contour (labelled 'Strong T-dep.'), uses a temperature and pCO_2-dependent weathering factor of $cT_e = 2.3$, which implies a strong temperature feedback on continental weathering compared to the pCO_2 feedback (see equation 5.7). The moderate temperature dependence contour (labelled 'Moderate T-dep.'), uses a temperature and pCO_2-dependent weathering factor of $cT_e = 7.5$. These two values for cT_e result in two different paths the Earth can take as it moves outward in the HZ. The planet color shows the mean surface temperature. Log-linear fits to the colored points of the 'Strong T-dep.' and 'Moderate T-dep.' contours have r^2 values of 0.959 and 0.999, respectively. Thus, even for a strong temperature dependence of continental weathering, our coupled climate and weathering model predicts an approximately log-linear relationship between incident flux and pCO_2 on Earth-like planets in the HZ.

in the atmosphere until the temperature returned to its nominal value of 289 K. Figure 5.1 shows this scenario with the dotted blue 289 K contour, which gives the pCO_2 value required to maintain a 289 K surface temperature for the modern Earth as it moves about the HZ. The line was calculated from a radiative-convective climate model described in Section 5.4.1.

The constant, 289 K surface temperature contour in Figure 5.1 is a non-linear relationship between incident flux, S, and log(pCO_2) but it does not consider the temperature and pCO_2 feedbacks inherent to the carbonate-silicate weathering cycle. We now show that if these feedbacks are taken into account, surface temperature declines with orbital distance and the relationship between S and log(pCO_2) is actually approximately linear for Earth-like planets in the HZ.

If Bond albedo is fixed, the surface temperature, T_s, for an Earth-like planet in steady-state varies approximately linearly with incident flux, S (Budyko, 1969; Koll & Cronin, 2018; Catling & Kasting, 2017, p.37-39). This linear relationship between T_s and S arises from energy balance and from the water vapor feedback and can be expressed as

$$F_{SOL} = F_{OLR} = \left(\frac{1 - A_B}{4}\right) S = a + bT_s \tag{5.1}$$

where F_{SOL} is the incoming solar radiation flux, F_{OLR} is the outgoing long-wavelength radiation flux, A_B is the Bond albedo, and a and b are empirical constants. From satellite measurements of the modern Earth and radiative calculations, for T_s in K, the empirical constants in equation 5.1 are approximately $a = -370$ W·m^{-2} and $b = 2.2$ W·m^{-2}·K^{-1} (Koll & Cronin, 2018).

Solving for T_s in equation 5.1, the surface temperature is given by

$$T_s = \left(\frac{1 - A_B}{4b}\right) S - \frac{a}{b}. \tag{5.2}$$

Under the conventional assumption that the HZ is regulated by a CO_2-H_2O greenhouse effect where H_2O concentrations respond to changes in pCO_2, the temperature offset in equation 5.2, $-a/b$, is a function of pCO_2. Thus, surface temperature as a function of S and pCO_2 is given by

$$T_s\left(S, \mathrm{pCO_2}\right) = \left(\frac{1 - A_B}{4b}\right) S + f\left(\mathrm{pCO_2}\right). \tag{5.3}$$

where $f\left(\mathrm{pCO_2}\right)$ is a function that depends on $\mathrm{pCO_2}$. For the modern Earth at 1 AU, $f(\mathrm{pCO_2}) = -a/b$. For $\mathrm{pCO_2} < 0.1$ bar, the $\mathrm{CO_2}$ greenhouse effect is logarithmic in $\mathrm{pCO_2}$, i.e., $f(\mathrm{pCO_2}) \propto \ln\left(\mathrm{pCO_2}\right)$ (e.g. Myhre et al., 1998; Pierrehumbert, 2010, p. 275). Above ~0.1 bar, weaker $\mathrm{CO_2}$ absorption features become important and $f(\mathrm{pCO_2})$ deviates from $\propto \ln\left(\mathrm{pCO_2}\right)$ (e.g. Charnay et al., 2017; Pierrehumbert, 2010, p. 226).

As $\mathrm{pCO_2}$ increases for an Earth-like planet moved outward in the HZ, the surface temperature will follow equation 5.3 while the rate at which $\mathrm{CO_2}$ is removed from the atmosphere will adjust according to the carbonate-silicate weathering feedback. Quantitatively, the $\mathrm{pCO_2}$- and T_s-dependent flux of $\mathrm{CO_2}$ removal due to the continental weathering flux, F_w (in mol $\mathrm{CO_2}$ per unit time) is described by

$$F_w = \rho \left(\frac{\mathrm{pCO_2}}{\mathrm{pCO_2^{mod}}}\right)^c \exp\left(\frac{T_s\left(S, \mathrm{pCO_2}\right) - T_s^{\mathrm{mod}}}{T_e}\right) \tag{5.4}$$

where ρ is a constant determined by the continental weathering properties of the modern Earth, c is a dimensionless constant between 0.1 and 0.5 and regulates the $\mathrm{pCO_2}$ dependence of continental weathering, T_e is a constant between 10 K and 40 K and represents the e-folding temperature dependence of continental weathering, and $\mathrm{pCO_2^{mod}} = 288 \times 10^{-6}$ bar and $T_s^{\mathrm{mod}} = 289$ K are the modern Earth's preindustrial $\mathrm{pCO_2}$ and surface temperature, respectively (Krissansen-Totton et al., 2018a).

In our full carbonate-silicate weathering model (see Section 5.4), which uses the parameters in Table 5.1, continental carbonate and continental silicate weathering are calculated independently. The $\mathrm{pCO_2}$-dependent continental weathering constant, c, in equation 5.4 incorporates both the $\mathrm{pCO_2}$-dependent continental weathering rate for silicates (α in Table 5.1) and for carbonates (ξ in Table 5.1). In equation 5.4, we assume seafloor weathering is negligible, which is a reasonable approximation for the modern Earth (Krissansen-Totton et al., 2018a), and illustrative for our purposes of deriving a simple, analytic relationship between S and $\mathrm{pCO_2}$. Here, we seek to predict the behavior of the modern Earth in the HZ to gain intuitive understanding, whereas in subsequent sections, we consider a general numerical model that includes Earth-like planets on which seafloor weathering may be important.

The modern Earth, and all Earth-like planets considered in this work, are assumed to be in steady-state, in which the flux of CO_2 from volcanic outgassing is equal to the rate of CO_2 removal from weathering, F_w. If we assume a HZ planet with CO_2 outgassing the same as the modern Earth's, F_w remains constant despite changes in S and $\mathrm{pCO_2}$. Setting $T_s\left(S, \mathrm{pCO_2}\right) = T_s^{\mathrm{mod}}$ and $\mathrm{pCO_2} = \mathrm{pCO_2^{mod}}$ for the modern Earth, from equation 5.4, we see that $F_w = \rho$ and

$$1 = \left(\frac{\mathrm{pCO_2}}{\mathrm{pCO_2^{mod}}}\right)^{c} \exp\left(\frac{T_s\left(S, \mathrm{pCO_2}\right) - T_s^{\mathrm{mod}}}{T_e}\right). \tag{5.5}$$

Equation 5.5 must hold for a "modern Earth" within the HZ. If it did not, F_w would not balance CO_2 outgassing, which would result in either complete CO_2 removal, or CO_2 accumulation without bound.

Solving for $T_s\left(S, \mathrm{pCO_2}\right)$ in equation 5.5 we find

$$T_s\left(S, \mathrm{pCO_2}\right) = T_s^{\mathrm{mod}} - cT_e \ln\left(\frac{\mathrm{pCO_2}}{\mathrm{pCO_2^{mod}}}\right). \tag{5.6}$$

Equating equation 5.6 to equation 5.3 and rearranging gives

$$\left(\frac{1 - A_B}{4b}\right) S = T_s^{\mathrm{mod}} - \left[cT_e \ln\left(\frac{\mathrm{pCO_2}}{\mathrm{pCO_2^{mod}}}\right) + f\left(\mathrm{pCO_2}\right)\right]. \tag{5.7}$$

If $f(\mathrm{pCO_2}) \propto \ln\left(\mathrm{pCO_2}\right)$, which is the case for $\mathrm{pCO_2} < 0.1$ bar (Charnay et al., 2017; Pierrehumbert, 2010, p. 226), then $S \propto -\ln\left(\mathrm{pCO_2}\right)$. However, even if $f(\mathrm{pCO_2})$ deviates from log-linearity with $\mathrm{pCO_2}$, S will become increasingly log-linear with $\mathrm{pCO_2}$ as cT_e increases. In equation 5.7, increasing cT_e will cause the $\ln\left(\mathrm{pCO_2}\right)$ term to dominate the relationship between S and $\mathrm{pCO_2}$. Intuitively, increasing cT_e decreases the temperature dependence of continental weathering relative to its $\mathrm{pCO_2}$ dependence. Note that bigger T_e reduces the temperature dependence of continental weathering while bigger c increases the $\mathrm{pCO_2}$ dependence of continental weathering (equation 5.4).

In addition to predicting a linear relationship between $\log(\mathrm{pCO_2})$ and S, the carbonate-silicate cycle implies that moving an Earth-like planet outward in the HZ will cause $T_s\left(S, \mathrm{pCO_2}\right)$ to decrease. For increasing orbital distance, $\mathrm{pCO_2}$ must increase for $T_s\left(S, \mathrm{pCO_2}\right)$ to increase in the HZ. From equation 5.5, $\mathrm{pCO_2}$ will be greater than $\mathrm{pCO_2^{mod}}$ in such cases so $T_s\left(S, \mathrm{pCO_2}\right)$ must be less than T_s^{mod}. This decrease in $T_s\left(S, \mathrm{pCO_2}\right)$ as S decreases is shown in Figure 5.1. Physically, the power law dependence of weathering on $\mathrm{pCO_2}$ can balance volcanic outgassing at lower surface temperatures in the outer HZ. The assumption in conventional HZ calculations of temperate or constant surface temperature (the 289 K line in 5.1) may be erroneous for a real planet with geochemical cycling.

Figure 5.1 shows the approximately log-linear relationship between $\mathrm{pCO_2}$ and S for the modern Earth moved outward in the HZ. The gray lines and colored circles in Figure 5.1 show the expected $\mathrm{pCO_2}$ value for the given incident flux S, calculated from equation 5.6. For each S value in Figure 5.1, equation 5.6 was solved for $\mathrm{pCO_2}$ by using equation 5.10, the polynomial fit for surface temperature based on a 1D climate model (described in Section 5.4.1), assuming values of cT_e.

The value of cT_e affects the slope of the relationship between S and $\mathrm{pCO_2}$ due to the carbonate-silicate weathering cycle, shown in Figure 5.1. From above, the ranges for c and T_e are $0.1 \leq c \leq 0.5$ and $10 \leq T_e \leq 40$ (Krissansen-Totton et al., 2018a), so $1 \leq cT_e \leq 20$. If we consider uniform distributions of c and T_e then roughly 95% of cT_e values will be greater than 2.3. If $c = 0.23$ and $T_e = 10$ K then $cT_e = 2.3$, which is used for the 'Strong T-dep.' curve in Figure 5.1. The mean of each parameter, $c = 0.3$ and $T_e = 25$ K gives $cT_e = 7.5$, which corresponds to the 'Moderate T-dep.' curve in Figure 5.1. For $cT_e < 2.3$ the colored points and gray curves become increasingly similar to the constant 289 K surface temperature contour in Figure 5.1. However, for uniform distributions of c and T_e, $\sim$95% of cT_e values are greater than 2.3 so an approximately log-linear relationship between S and $\ln\left(\mathrm{pCO_2}\right)$ is the default expectation for Earth-like planets in the HZ.

As shown in Figure 5.1, the relationship between $\mathrm{pCO_2}$ and incident flux may be log-linear for an Earth-like planet within the HZ. However, if uncertainties in planetary characteristics, such as land fraction, outgassing rates, and biological weathering are taken into account, considerable variability could exist between stable $\mathrm{pCO_2}$ levels and incident flux for Earth-like planets in the HZ. These variations could lead to considerable scatter around the expected log-linear relationship between $\mathrm{pCO_2}$ and S in the HZ, which motivates us to consider a numerical carbonate-silicate model.

5.4 Methods for numerical carbonate-silicate cycle modeling

To calculate the steady-state $\mathrm{pCO_2}$ in the atmospheres of Earth-like planets in the HZ, we use the weathering model developed by Krissansen-Totton & Catling (2017) and Krissansen-Totton et al. (2018a). We summarize the model below and highlight how the the model in this work differs from that of Krissansen-Totton et al. (2018a). The reader should consult Krissansen-Totton et al. (2018a) for a comprehensive explanation and justification of the model parameterizations, and empirical and theoretical basis.

The weathering model balances the flux of outgassed $\mathrm{CO_2}$ against the loss of carbon in the weathering of carbonates and silicates, which results in precipitation of carbonates in the ocean and seafloor pore space. Quantitatively, for time t, this is described by time-dependent equations where we normalize to the mass of the ocean, M_o (nominally, an Earth ocean, 1.35×10^{21} kg):

$$\begin{aligned} \frac{dC}{dt} &= \frac{F_{out} + F_{carb} - P_o - P_p}{M_o} \\ \frac{dA}{dt} &= 2 \cdot \frac{F_{sil} + F_{carb} + F_{diss} - P_o - P_p}{M_o}. \end{aligned} \tag{5.8}$$

Here, C is the non-organic carbon content of the atmosphere-ocean system in mol C $\mathrm{kg^{-1}}$, and A is the carbonate alkalinity in mol equivalents. Carbonate alkalinity (henceforth "alkalinity") is the charge-weighted sum of the mol/liter concentration of bicarbonate and carbonate anions, $[\mathrm{HCO_3^-}] + 2[\mathrm{CO_3^{2-}}]$. F_{out} is the global $\mathrm{CO_2}$ outgassing flux (mol C $\mathrm{yr^{-1}}$), F_{carb} and F_{sil} are the continental carbonate and silicate weathering fluxes (mol C $\mathrm{yr^{-1}}$), and P_p and P_o are the pore and ocean precipitation fluxes (mol C $\mathrm{yr^{-1}}$).

Parameter	Parameter Description	Range	Scaling	Units
F_{out}^{mod}	Modern CO_2 outgassing flux	6-10		Tmol C yr^{-1}
n	Carbonate precipitation coefficient	1-2.5	$\propto \left[CO_3^{2-}\right]^n$	
x	Modern seafloor dissolution relative to precipitation	0.5-1.5	$\propto xF_{out}^{mod}$	
T_e	E-folding temperature factor for continental weathering	10-40		K
α	Power law exponent for CO_2 dependence of continental silicate weathering	0.1-0.5	$\propto (pCO_2)^{\alpha}$	
ξ	Power law exponent for CO_2 dependence of continental carbonate weathering	0.1-0.5	$\propto (pCO_2)^{\xi}$	
f_{land}	Land fraction compared to modern Earth	0-1		
S_{thick}	Ocean sediment thickness relative to modern Earth	0.2-1		
F_{carb}^{mod}	Modern continental carbonate weathering	7-14		Tmol C yr^{-1}
f_{bio}	Biological weathering compared to modern Earth	0-1		
a_{grad}	Surface to deep ocean temperature gradient scaling	0.8-1.4	$\propto a_{grad}T_s$	
γ	Power law exponent for pH dependence of seafloor dissolution	0-0.5	$\propto \left(\left[H^+\right]\right)^{\gamma}$	
β	Power law exponent for seafloor spreading rate	0-0.2	$\propto Q^{\beta}$	
m	Exponent for outgassing dependence on crustal production	1-2	$\propto Q^m$	
E_{bas}	Seafloor dissolution activation energy	60-100		kJ mol^{-1}
n_{out}	Exponent for internal heat with time	0-0.73	see eq. 5.9	
τ	Planet age (see eq. 5.9)*	0-10		Gyr
S	Incident flux relative to modern Earth*	0.35-1.05		

Table 5.1: Parameters are dimensionless unless otherwise described. The fourth column shows how scaling parameters impact the model, where T_s is the surface temperature in K and Q is the internal heat of the planet relative to the modern Earth (see equation 5.9 for Q). The justification for each parameter range can be found in Krissansen-Totton et al. (2018a) unless otherwise noted. *The justification for this parameter is given in Section 5.4.

The alkalinity that enters the ocean from weathering will balance a +2 charge cation (e.g. Ca^{++}), which is why a factor of 2 enters in the definition of dA/dt in equation 5.8. Hence, geochemists often think of alkalinity in terms the balance of cations produced in weathering, principally Ca^{++}. This reasoning arises because the weighted sum of carbonate and bicarbonate concentrations must balance the charge of conservative cations minus conservative anions (i.e., 2[Ca^{++}] + 2[Mg^{++}] + Na^{+} +... - [Cl^{-}] - ...), ignoring minor contributions form weak acid anions and water dissociation. Weathering releases cations and carbon speciation adjusts to ensure charge balance, so that the cation release is effectively equivalent to carbonate alkalinity.

To improve the rate of model convergence and range of model inputs over which equation 5.8 converges, we do not consider the seafloor pore space and atmosphere-ocean as separate systems. This differs from Krissansen-Totton et al. (2018a) who consider the atmosphere-ocean and pore space independently. Rather, we approximate the atmosphere-ocean and pore space as a single entity in equation 5.8. This simplification does not appreciably change the model output for atmospheric CO_2 because we run the model to steady-state in all cases, where the atmosphere-ocean and pore space reach approximate equilibrium. Section 5.4.2 presents additional details on our model implementation and discusses the agreement between our no-pore model and the original, two-box model of Krissansen-Totton et al. (2018a).

A second modification is the range of incident stellar fluxes over which the model can be run. Krissansen-Totton et al. (2018a) studied the Earth through time and thus only considered solar fluxes between $S_\oplus$ (the modern solar constant) and early Earth's $0.7S_\oplus$ ($S_\oplus$ = 1360 W m^{-2}). We extend that range to include the entire conservative HZ of a Sun-like star, roughly $1.05S_\oplus$ to $0.35S_\oplus$ (Kopparapu et al., 2013).

Our model uses the Virtual Planetary Laboratory (VPL) 1D climate model, described in detail by Meadows et al. (2018b) and Appendix A of Catling & Kasting (2017), to generate surface temperatures for an Earth-like planet at various pCO_2 and incident fluxes. We assume the atmosphere is comprised of CO_2, N_2, and water vapor. To reduce model runtimes, we fit a 4^{th}-order polynomial in $\ln(pCO_2)$ and stellar flux to the 1D climate model surface temperature output to use with our weathering model. Section 5.4.1 shows our climate model polynomial and its agreement with the 1D VPL climate model.

With the coupled climate and weathering model, we generate steady-state, Earth-like planets by randomly sampling plausible initial model inputs. The ranges and justification for each parameter we consider are described in Krissansen-Totton et al. (2018a) and shown in our Table 5.1. These ranges represent very broad uncertainties of the carbonate-silicate cycle on the Earth through time and so are appropriate for Earth-like planets. We conservatively assume a uniform distribution for each parameter range shown in Table 5.1.

We parameterize the internal heat of an Earth-like planet conservatively using the planet's age, ranging 0 to 10 Gyr, which is the approximate habitable lifetime of an Earth-like planet around a Sun-like star (Rushby et al., 2013). The equation for planetary heat relative to the modern Earth, Q, is given by

$$Q = \left(1 - \frac{4.5 - \tau}{4.5}\right)^{-n_{out}} \tag{5.9}$$

where τ is the age of the planet in Gyr, and n_{out} is the scaling exponent for internal heat, with a range given in Table 5.1 (justified in the supplementary materials of Krissansen-Totton et al. (2018a)).

Our model assumes that each simulated planet is habitable, i.e., it has a stable, liquid surface ocean, a necessity for the carbonate-silicate cycle to operate. For a mean surface temperature below 248 K, Earth-like planets are likely completely frozen (Charnay et al., 2013), which we use as a lower temperature bound in the model. While 248 K is below the freezing point of water, it is a global mean surface temperature and 3D models show that the range 248-273 K for this parameter does not preclude the existence of a liquid ocean belt near the equator. At the other temperature extreme, a hot, Earth-like planet can rapidly lose its surface oceans due to high atmospheric water vapor concentrations that are photolyzed and subsequently lost to space. This upper temperature bound on habitability occurs at ∼355 K (Wolf et al., 2017). Above 355 K, Earth-like planets are unlikely to remain habitable for more than ∼1 Gyr (Wolf et al., 2017) and cannot operate a carbonate-silicate cycle over geologic timescales. We use these two temperature bounds, 248 K and 355 K, as the limits for habitability in our model. Any modeled planet with a final surface temperature outside these limits is uninhabitable and removed from our results.

We limit HZ planets to those with pCO_2 below 10 bar. For most Earth-like planets in the HZ, 10 bar of CO_2 results in planets with surface temperatures well above 355 K, which are not habitable on long time scales. If we impose a fixed stratospheric water vapor concentration in the 1D climate model and modify the tropospheric water vapor concentration based on empirical data from the modern Earth, we enable the 1D climate model to accurately model habitable, Earth-like planets through much of the HZ. But in the outer HZ, with more than $\sim$10 bar of CO_2, this assumption overestimates atmospheric water vapor concentrations and leads to artificially warm planets, so we reject such cases. Above $\sim$10 bar of CO_2 in the outer HZ, Kopparapu et al. (2013) found that increasing atmospheric CO_2 does not lead to additional warming, using a model that assumed a saturated troposphere for water vapor. Rather, the surface cools in such scenarios because additional CO_2 leads to increased Rayleigh scattering and no additional warming. Because Earth-like planets in the outer HZ would be frozen and uninhabitable even with CO_2 partial pressures above $\sim$10 bar, we impose a 10 bar limit for CO_2 in the outer HZ. This limit agrees with the coupled climate and weathering model of Kadoya & Tajika (2014).

5.4.1 Expanded Climate Model

We use the 1D radiative-convective climate model described in Meadows et al. (2018b) and Appendix A of Catling & Kasting (2017) to model the surface temperatures of Earth-like planets. We consider incident fluxes between $1.05S_\oplus$ and $0.35S_\oplus$, the HZ limits for a Sun-like star, and atmospheric CO_2 partial pressures between 10^{-6} and 10 bar. We assume the atmosphere is comprised of CO_2 and H_2O. If the CO_2 partial pressure is below 1 bar, we set the initial atmospheric pressure to 1 bar and add N_2 to the atmosphere such that the total surface pressure is 1 bar. We fix the stratospheric water vapor concentration to the modern Earth value and follow the Manabe-Wetherald relative humidity distribution in the troposphere with empirical constraints based on the modern Earth (Manabe & Wetherald, 1967).

We fit the surface temperature output, T_s in K, from the climate model with a 4^{th} order

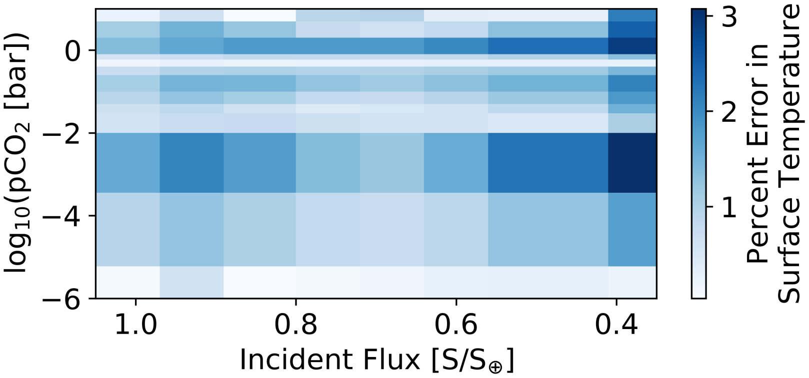

Figure 5.2: The relative error between our 4^{th}-order polynomial fit and the full 1D radiative-convective climate model. Our polynomial fit is valid between 1.05$S_\oplus$ and 0.35$S_\oplus$, where $S_\oplus$ is the Solar constant. The polynomial fit is valid for atmospheric CO_2 abundances between 10^{-6} and 10 bar. The surface temperatures predicted by the polynomial fit reproduce the results of the 1D climate model. The maximum error in predicted surface temperature between the polynomial fit and the 1D climate model is ~3%.

polynomial in $\ln(\mathrm{pCO_2})$ and normalized stellar flux, as follows:

$$\begin{aligned} T_s\left(S, \mathrm{pCO_2}\right) = 4.809 - 222.0X - 68.44X^2 - 6.737X^3 - 0.206X^4 \\ +1414XY + 446.4X^2Y + 44.41X^3Y + 1.364X^4Y \\ -2964XY^2 - 978.4X^2Y^2 - 98.86X^3Y^2 - 3.059X^4Y^2 \\ +2655XY^3 + 907.5X^2Y^3 + 92.87X^3Y^3 + 2.892X^4Y^3 \\ -868.4XY^4 - 304.6X^2Y^4 - 31.48X^3Y^4 - 0.985X^4Y^4 \\ +1045Y - 1496Y^2 + 1064Y^3 - 281.1Y^4. \end{aligned} \tag{5.10}$$

Here, CO_2 partial pressure $\mathrm{pCO_2}$ is in bar, $X = \ln(\mathrm{pCO_2})$, and $Y = S/S_\oplus$ is the incident flux, S, normalized to the solar constant, $S_\oplus$.

Figure 5.2 shows the agreement between the 1D climate model and the polynomial fit used in this work.

5.4.2 Combined Ocean and Pore Space Model

The carbon cycle model described by Krissansen-Totton et al. (2018a) used a two-box model, where the atmosphere-ocean and the seafloor pore space were separated. In this work, we combine the ocean-atmosphere and the pore space into a single unit. This modification can be implemented in the Krissansen-Totton et al. (2018a) model by assuming that the pH of the pore space is the same as the pH of the ocean, and assuming that the alkalinity and carbon content of the ocean and pore space are the same. The dissolution and precipitation fluxes can then be calculated without treating the ocean-atmosphere and the pore space as different systems. This modification allows the model to converge quicker over a wider range of parameter combinations.

To validate our combined model, we ran the modern Earth through both the original, two-box model of (Krissansen-Totton et al., 2018a) and our modified model at 10 different incident fluxes between $S_\oplus$ and $0.7S_\oplus$. The average error in predicted CO_2 values between our model and the two-box model was 2.8%, with a minimum error of 2.3%, and a maximum error of 3.6%. Given the large uncertainties in model inputs (Table 5.1), the few percent error introduced by our simplified model is unimportant.

For each parameter combination in our simplified model, we run the simulation for 10 Gyr or until the system reaches steady state. We consider the model to have converged if the change in atmospheric CO_2 partial pressure is less than 1% over 1 Gyr. Rarely (2 of the 1200 planets simulated in this work), parameter combinations will not reach-steady state after 10 Gyr. Simulations with combinations of exceptionally high outgassing rates and low CO_2 weathering rates can enter a regime were atmospheric CO_2 builds without bound, never converging. Such model results are beyond the range of validity of our model.

5.5 Results of habitable zone carbonate-silicate cycling modeling

We generated 1050 habitable, stable, Earth-like exoplanet climates using uniform distributions of the parameters in Table 5.1. A total of 1200 random, initial parameter combinations

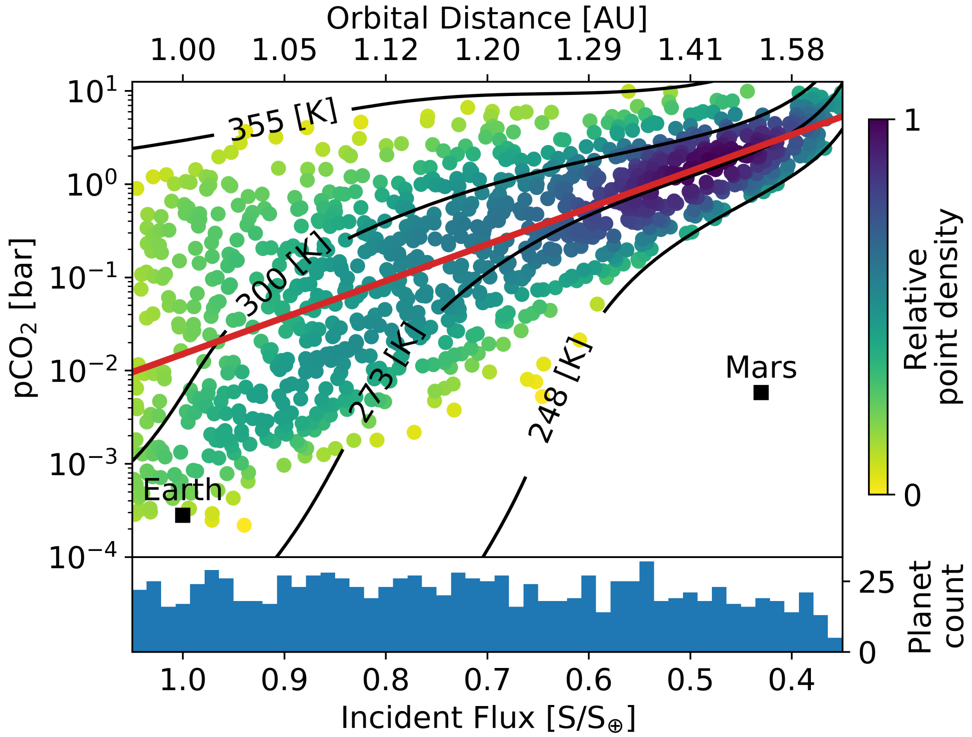

Figure 5.3: The expected distribution of stable, Earth-like exoplanet climates from our habitable zone weathering model. The horizontal axis shows incident flux, S, normalized to the solar constant ($S_\oplus$) and the corresponding orbital distance in Astronomical Units (AU) above the plot. The vertical axis shows the atmospheric CO_2 partial pressure (pCO_2) in bar. Each point represents a climate in steady-state. The black labeled contours show the mean global surface temperature for the given pCO_2 and incident flux. The white region below the 248 K contour is where our model assumption of a liquid ocean is no longer plausible so no planets are shown in that region. Above the 355 K contour Earth-like planets are too hot to retain their liquid oceans for billions of years. Similar to the frozen planets, such hot planets are not considered habitable. The red line shows the line of log-linear best fit through the simulated planets. Modern Earth and Mars are shown by black squares. The blue histogram at the bottom of the figure shows the number of stable planets in each incident flux bin. The color of each simulated planet shows the relative point density in the plot at that location. The color was calculated using a kernel-density estimate with Gaussian kernels and rescaled from 0 to 1. A color value of 0 represents the lowest relative point density, 1 the highest. Our model predicts that atmospheric CO_2 should increase with orbital distance in the HZ. The slope of the best fit line is 3.92 ± 0.24 (95%) with units $-\log_{10}(pCO_2\ [\mathrm{bar}])/[S/S_\oplus]$.

were considered but we eliminated those that resulted in planets that froze completely or were too hot to retain their surface oceans. As colored dots, Figure 5.3 shows habitable, steady-state solutions.

Our model indeed predicts that atmospheric CO_2 abundances should broadly increase

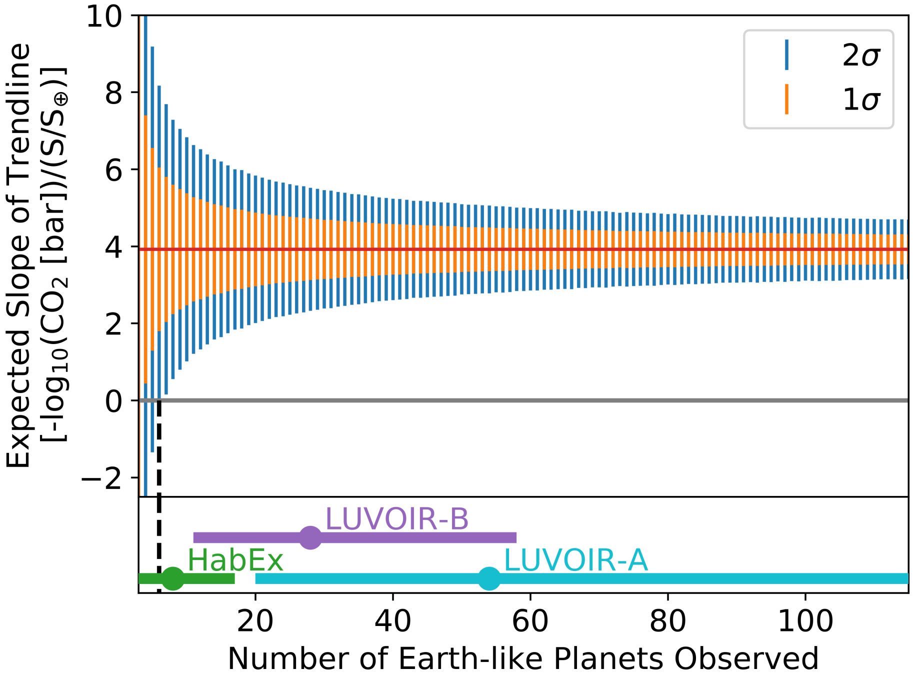

Figure 5.4: The expected trend of atmospheric CO_2 with incident flux vs the number of observed Earth-like planets. The solid red line shows the mean slope from 10,000 random subsets of the planets in Figure 5.3 with each subset containing the given number of observed planets. The orange and blue error bars show the 1σ and 2σ uncertainties on the expected slope. The solid gray line highlights the zero slope line. The dashed black line shows the point where the expected slope with 2σ confidence is above zero. At the bottom of the figure, the labeled points and error bars show the number of Earth-like exoplanets the next generation of proposed space telescopes are expected to observe (telescope data in Table 5.2). The vertical scaling of the telescope points is arbitrary, only the horizontal position and extent of the error bars is significant. Six Earth-like exoplanets should be observed to be 95% confident that a positive trend between atmospheric CO_2 and decreasing incident flux is detected.

and narrow in their spread with orbital distance in the HZ (Figure 5.3). If a log-linear fit is applied to the data in Figure 5.3, the expected relationship between pCO_2 and S (Section 5.3), the fit has an r^2-value of 0.49. Thus, about half the variance in $\log(pCO_2)$ is described by changes in incident flux. This best fit is shown by a solid red line in Figure 5.3. It has a slope of 3.92±0.24 (95%) with units $-\log_{10}(pCO_2\ [\text{bar}])/[S/S_\oplus]$. Thus our model predicts a trend of increasing atmospheric CO_2 with orbital distance, which future missions might detect. However, there is sufficient spread in our simulated planets that, should a future mission detect only a few planets, it might not detect such a trend and could detect scatter or even the reverse trend.

This uncertainty between incident flux and atmospheric CO_2 is shown in Figure 5.4. This figure is generated by randomly selecting 10,000 subsets of the planets in Figure 5.3 for each number of observed Earth-like exoplanets (horizontal axis in Figure 5.4). For example, for the value 3 on the horizontal axis of Figure 5.4, we select 10,000 3-planet subsets at random from all the stable, habitable planets shown in Figure 5.3. For each of the 10,000 subsets, we calculate the log-linear line of best fit through the selected planets, relating incident flux and atmospheric CO_2. The slopes of all 10,000 best fit lines are used to find the mean and standard deviation in expected slope for the given number of observed Earth-like exoplanets. As the number of subsets increases, the mean slope approaches the slope of the best fit line in Figure 5.3, which is shown by the solid red line in Figure 5.4. The 1σ and 2σ uncertainties on the expected slope are shown by the orange and blue error bars, respectively, in Figure 5.4.

From Figure 5.4 we see that, to be 95% confident of a trend of increasing atmospheric CO_2 with decreasing incident flux (i.e., a slope > 0), we would need to observe 6 or more Earth-like HZ exoplanets. Proposed NASA telescopes, HabEx and LUVOIR, are expected to observe between 3 and 115 Earth-like exoplanets (Table 5.2). The ranges are shown by the colored circles with error bars in Figure 5.4 for each mission concept. The nominal capability of LUVOIR-A or LUVOIR-B would confidently detect a trend of increasing atmospheric CO_2 with decreasing incident flux. A caveat is that this calculation does not consider the instrument uncertainty in derived pCO_2 measurements for each telescope.

Telescope	Diameter [m]	Expected Yield (1σ)
HabEx	4	8^{+9}_{-5}
LUVOIR-B	8	28^{+30}_{-17}
LUVOIR-A	15	54^{+61}_{-34}

Table 5.2: The number of expected Earth-like exoplanets observed by each platform from the HabEx (2019) and LUVOIR (2019) final reports.

5.6 Discussion

Our model assumes that the full variation and uncertainty in Earth's carbon cycle parameters through time (Table 5.1) are representative of habitable Earth-like exoplanets generally. This assumption is a reasonable first-order approximation as the bulk composition and geochemistry of rocky exoplanets appear similar to Earth's (Doyle et al., 2019). However, the validity of this assumption likely depends on the parameter in question. For example, it is probably reasonable to expect habitable exoplanets to have a wide range of land fractions and outgassing fluxes, but it is unclear whether there is as much natural variability in the temperature dependence of silicate weathering. An improved mechanistic understanding of weathering on Earth (e.g. Maher & Chamberlain, 2014; Winnick & Maher, 2018) might reduce these uncertainties.

Other weathering feedbacks have been proposed to operate on the Earth through time, such as reverse weathering (Isson & Planavsky, 2018). In reverse weathering, cations and dissolved silica released from silicate weathering are sequestered into clay minerals rather than carbonates so that CO_2 remains in the atmosphere, warming the climate and reducing ocean pH. Reverse weathering is thought to be strongly pH dependent and as ocean pH decreases, reverse weathering turns off, acting as a climate stabilization mechanism similar to the carbonate-silicate cycle. The importance of reverse weathering is so poorly constrained through Earth's history (Krissansen-Totton & Catling, 2020) that it does not make sense to consider it in our model. However, with future constraints from geology and lab measurements, reverse weathering might increase the stable CO_2 abundances of our modeled atmospheres shown in Figure 5.3.

Because we only consider variations on an Earth-like planet, our model predictions may underestimate the inherent variability in habitable exoplanetary conditions. Planets very different from the modern Earth, such as waterworlds without a carbonate-silicate weathering cycle (e.g. Kite & Ford, 2018) or CH_4-rich worlds (e.g. Haqq-Misra et al., 2008; Wordsworth et al., 2017), could introduce additional uncertainty in an observed relationship between S and pCO_2 in the HZ. Despite such uncertainties, future missions should search for a trend of pCO_2 with orbital distance in the HZ. If the carbonate-silicate weathering cycle is indeed ubiquitous, as is typically assumed in HZ calculations, then the relationship between orbital distance and pCO_2 may follow the trends predicted in Sections 5.3 and 5.5. If no such trend is observed, then the carbonate-silicate weathering cycle may have limited influence on planetary habitability and the limits of the conventional HZ could need revision.

5.7 Conclusions

The conventional HZ concept assumes that the carbonate-silicate cycle "thermostats" Earth-like planets to temperate, or even constant surface temperature, but the way the cycle actually operates has been neglected in HZ climate calculations. We find that for constant CO_2 outgassing, the surface temperature declines with orbital distance within the HZ because as pCO_2 rises with distance due to carbon cycle feedbacks, the power law pCO_2-dependence of weathering can remove carbon and balance outgassing at a lower surface temperature (Figure 5.1).

We also find that standard energy-balance theory combined with carbonate-silicate cycle theory predicts a linear relationship between $\log(pCO_2)$ and incident stellar flux within the HZ (Figure 5.1). However, variability in geophysical and physicochemical parameters in the carbonate-silicate cycle will produce spread in $\log(pCO_2)$ at a given orbital distance (Figure 5.3).

Future telescopes will probe the atmospheric compositions of Earth-like planets in the HZ. However, proposed testing of the HZ hypothesis via such measurements (e.g. Bean et al., 2017; Turbet, 2019) may be precluded if too few planets are observed. Considering variability of parameters in the carbonate-silicate cycle, we show that pCO_2 could vary a few orders of magnitude at a given incident flux for a stable, habitable, Earth-like planet, but nonetheless an underlying statistical trend exists (Figure 5.3).

Our modeling results show that to observe the predicted trend of increasing pCO_2 with increasing orbital distance in the HZ with 95% confidence, future telescopes would need to observe at least 6 Earth-like exoplanets. This estimate does not consider observational uncertainties nor the uncertainties that planets very different from Earth could introduce and thus should be considered a lower bound.

Chapter 6

PLANT COLOR AROUND OTHER STARS

Status

This work is currently in preparation under the title *The color of plants around other stars from spectral optimization theory* by **Owen R. Lehmer, David C. Catling, Mary N. Parenteau, Nancy Kiang, and Tori M. Hoehler**. This chapter is an initial draft that will likely differ from a future published version.

6.1 Abstract

In the search for life on other planets, the presence of photosynthetic surface organisms may be detectable from the colors of light they reflect, which on the modern Earth is a steep increase in reflectance at long, visible wavelengths, a “red edge”. However, the total reflected spectra of Earth-like exoplanets could only be affected by a few percent due to “red edge” analogs. Thus, knowing the wavelengths at which photosynthetic organisms preferentially absorb and reflect photons is necessary to detect “red edge” analogs on other planets. Using a numerical model that predicts the absorption profile of extant photosynthetic pigments on Earth, we calculate the absorption profile for pigments on an Earth-like planet around F through late M type stars that are adapted for maximal energy production. In our model, cellular energy production is maximized when pigments are tuned to absorb at the wavelength that maximizes energy input from incident photons while minimizing energy losses due to thermal emission and building the photosynthetic apparatus. We find that peak photon absorption for photosynthetic organisms around F type stars tends to be in the blue while for G, K, and early M type stars, red or just beyond is preferred. Around the coolest M type stars these organisms may preferentially absorb in the infrared, possibly past 1 μm.

Our predicted absorption profiles for photosynthetic surface organisms depends on both the stellar type and the atmospheric composition, especially atmospheric H_2O concentrations, which alter the availability of surface photons and thus the predicted pigment absorption. By constraining the possible absorption profiles of alien, photosynthetic organisms, future observations may be better equipped to detect the weak spectral signal of "red edge" analogs.

6.2 Introduction

Why are plants green? Despite the question's simplicity, a definitive answer remains elusive. Obviously, the color of plants depends largely on their pigments, which preferentially reflect in the green. So, the real questions are: "why do photosynthetic organisms have the pigments they do, and what determines the spectral absorption of those pigments?" In particular, we are interested in the extraterrestrial analogs of chlorophyll *a* (chl *a*), the dominant pigment responsible for the red absorption profile in oxygen-producing photosynthetic organisms, such as green land plants, algae, and cyanobacteria.

Previously, the structure of chl *a* has been attributed to evolution from simpler porphyrins, or the chemical properties required of a pigment to participate in oxygenic photosynthesis (e.g. Mauzerall et al., 1976; Björn et al., 2009; Björn & Ghiradella, 2015). In addition, optimization arguments based on the available solar spectrum have been proposed as a driver for the structure and absorption profile of chl *a* (Björn, 1976; Stomp et al., 2007; Kiang et al., 2007a; Milo, 2009; Marosvölgyi & van Gorkom, 2010). Briefly, these arguments posit that pigment absorption should evolve to correspond to peaks in the spectral photon flux. While these optimization arguments cannot explain the entire absorption spectra of chl *a*, such as its absorption of blue photons, they do predict the peak in red photon absorption (Björn, 1976; Milo, 2009) and even the shape of the pigment absorption profile around that peak (Marosvölgyi & van Gorkom, 2010). In addition to predicting the red absorption profile of chl *a*, the same optimization arguments can explain the absorption profiles of pigments in niche environments where photons are limited, such as the bottom of the water column or within an organic-rich microbial community (Stomp et al., 2007; Kiang et al., 2007a;

Marosvölgyi & van Gorkom, 2010).

Of particular interest among these photon optimization studies is the model developed by Marosvölgyi & van Gorkom (2010), which considered incident photon flux (accounting for atmospheric absorption), thermal emission of pigments, and the cellular costs required to create the photosynthetic apparatus. The model of Marosvölgyi & van Gorkom (2010) was able to predict both the absorption peak of extant Earth pigments and the shape of the absorption profile around that peak. Similar spectral optimization models correctly predict the wavelength of peak absorption in extant organisms but do not constrain the shape of the absorption profile around that peak (Björn, 1976; Milo, 2009).

Here, we apply the photon optimization model of Marosvölgyi & van Gorkom (2010) to the Earth around other stars to predict the absorption profiles of alien photoautotrophs. Prediction of pigment absorption around other stars has been considered previously, but via a simplified model with stars approximated as blackbodies (Lehmer et al., 2018), or qualitatively based on the incident spectral flux (Kiang et al., 2007b; Ritchie et al., 2017; Takizawa et al., 2017). In addition, from the pigment properties of infrared-absorbing organisms reported by Kiang et al. (2007b), Tinetti et al. (2006) predicted a "red edge" for an M dwarf star could be near 1.1 μm. Using simulated surface spectra through the modern Earth's atmosphere for F2V through M5V stars from Kiang et al. (2007b), we predict the absorption peak and profile of pigments for various stellar types. Our predictions could inform future observations looking for the photosynthetic "red edge" as a possible biosignature (Sagan et al., 1993; Seager et al., 2005; Kiang et al., 2007b; O'Malley-James & Kaltenegger, 2018).

6.3 Methods

To predict optimal pigment absorption based on incident photon flux, we use the model initially developed by Björn (1976) then refined and justified in detail by Marosvölgyi & van Gorkom (2010). Our implementation recreates the numerical model described in Marosvölgyi & van Gorkom (2010), which we summarize below.

The model solves for an absorption profile that optimizes energy production in a photosynthetic cell. It does so by considering the incident flux available for absorption, thermal emission, and the costs to build the photosynthetic apparatus. With incident flux known, the input intensity in Watts m^{-2}, P_{in}, is given by

$$P_{in} = J_L \cdot \mu = J_L \cdot kT \cdot \ln\left(\frac{J_L}{J_D}\right) \tag{6.1}$$

where k is the Boltzmann constant (1.381×10^{-23} J K^{-1}), T in K is the temperature of the organism (assumed to be at room temperature, 295 K), J_L is the excitation rate in light (s^{-1} m^{-2}), and J_D is the thermal excitation rate (s^{-1} m^{-2}) (Ross & Calvin, 1967; Marosvölgyi & van Gorkom, 2010). In equation 6.1, μ is the potential energy of the excited pigments in the system, in Joules, corrected for emissive loss. Thus, P_{in} is the number of excitation events (photon absorption) generating an excited pigment multiplied by the potential energy of such a pigment, μ.

The excitation rate due to the incident solar flux, J_L, is found by dividing the incident flux into n equally sized frequency bins ($n = 1200$ in this work) then multiplying by the pigment absorptance for the given frequency. Each bin represents the integrated photon flux across the the frequency bin. Thus,

$$J_L = \sum_{i=1}^{n} I_{sol,i}(1 - e^{-\tau_i}) \tag{6.2}$$

where τ_i is the optical depth of the pigment over the frequencies in bin i, and $I_{sol,i}$ (photons m^{-2} s^{-1}) is the integrated incident photon flux per unit area for the given frequency bin. Similarly, the thermal excitation rate, J_D, is given by

$$J_D = \sum_{i=1}^{n} \tau_i \cdot I_{bb,i} \tag{6.3}$$

where $I_{bb,i}$ (photons m^{-2} s^{-1}) is the integrated blackbody photon flux at 295 K (room temperature) per unit area for the frequency range of bin i. The bin size should be small enough such that spectral features are not obscured. However, large discontinuities between adjacent bins can hinder convergence, which can occur if too many bins are used. Dividing the spectra in this work, which includes frequencies between ∼1200 and ∼120 THz (280 to 2500 nm), into 1200 bins preserves spectral features and does not hinder convergence. The photon fluxes used in this work are shown in Figure 6.1.

If the relative cellular cost of creating the photosynthetic apparatus is given by C, then the optimal absorption profile is found by finding the τ_i that satisfy

$$I_{sol,i} \cdot h\nu_i \cdot e^{-\tau_i} = \frac{kT \cdot e^{\mu/(kT)} \cdot h\nu_i}{\mu + kT} \cdot I_{bb,i} + \frac{P_{in}}{(\mu + kT) \cdot \sum_{i=1}^{n} \tau_i/(h\nu_i)} \cdot C. \tag{6.4}$$

In equation 6.4, h is the Planck constant (6.626×10^{-34} J s). The relative cost parameter, C, is a free parameter set between 0 and 1. The left-hand side of equation 6.4 is the transmitted photon energy.

The first term on the right-hand side (RHS) of equation 6.4 is the scaled blackbody flux of the pigment. This term sets the frequency below which pigments would emit more energy than they absorb and results in an abrupt transition to a transmittance of 1 below the cutoff frequency. This frequency cutoff is analogous to the bandgap in photovoltaic semiconductors (Marosvölgyi & van Gorkom, 2010).

The second term on the RHS of equation 6.4 is spectrally constant and imposes an input energy threshold on the frequencies at which a pigment can absorb. As C increases, the net energy input in a frequency bin must be above the threshold set by this term for pigments to absorb. For high costs, pigments will only absorb photons in spectral regions where net input energy is abundant (which depends on both the quantity of photons available and their energy). The effect of this term on the calculated absorption profile for the Earth around the Sun is shown in Figure 1 of Marosvölgyi & van Gorkom (2010).

Equation 6.4 is a fixed-point equation that can be solved with iterative mapping. For a given cost, C, an initial guess for each τ_i is provided then equation 6.4 is iterated until convergence is reached. For values of C near 0 or 1, the initial guess for each τ_i must be close to the solution for the model to converge. Therefore, we initially run the model with an intermediate value for C (such as $C = 0.5$) and initialize each τ_i to 1 then iterate equation 6.4 to convergence. With the converged solution for each τ_i at the intermediate C value, we iterate over C to $C = 1$ or $C = 0$ using the previously converged solution for each τ_i as inputs to equation 6.4 for the next value of C. In this way, equation 6.4 converges for all C values between 0 and 1, including the end points.

The relative cost parameter, C, can be freely tuned in the model. However, a relative cost of $C = 0.962$, indicating photosynthetic machinery is expensive to produce, reproduces the red absorption feature of spinach chloroplasts. Furthermore, the same cost parameter applied to the ambient spectra in a muddy water column reproduces the absorption position and shape of the *Rhodobacter sphaeroides* chromatophores (Marosvölgyi & van Gorkom, 2010). Following Marosvölgyi & van Gorkom (2010), we assume that a cost of $C = 0.962$ is applicable to photosynthetic organisms generally, but see Section 6.7.1 for details on how the cost parameter alters the optimal absorption spectra.

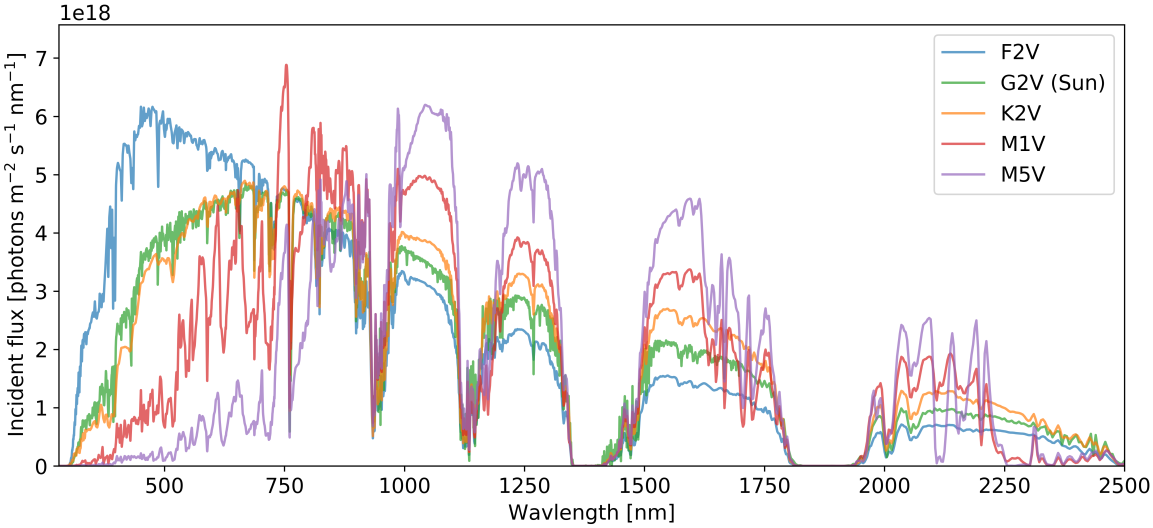

Figure 6.1: Surface flux for a planet with the modern Earth's atmosphere around different stars. The horizontal axis shows photon wavelength in nm, the vertical axis shows the incident photon flux per unit area, per second, per nm. Each colored contour shows the surface photon flux for a different stellar type, as labelled. For each stellar type, the total flux at the top of atmosphere was assumed to be the same as the modern Earth's.

As inputs to the model, we use the standard solar irradiance spectrum for the modern Earth at sea level from ASTM (2020). We also consider simulated surface spectra from Kiang et al. (2007b) for the modern Earth around F2V, K2V, M1V, and M5V type stars, with a top of atmosphere total flux equal to the modern Earth's. The spectra considered in this work are shown in Figure 6.1.

6.4 Results

From the spectra in Figure 6.1, Figure 6.2 shows the predicted absorption profile for optimal pigments around each stellar type. The gray shaded region shows the absorption profile of spinach chloroplasts from Marosvölgyi & van Gorkom (2010), which matches the predicted absorption profile for red photons in chl a on Earth (green contour in Figure 6.2). The green contour in Figure 6.2 reproduces the results of Marosvölgyi & van Gorkom (2010). It is important to note in Figure 6.2 that the absolute absorptance value predicted by the model is not necessarily representative of the total absorptance of an organism. The model predicts an optimal absorption wavelength and profile over wavelength, but an organism could produce multiple copies of the optimal pigment, which would alter the absolute absorptance of the organism.

The predicted optimal absorption profiles for each stellar type shows the influence of atmospheric absorption on pigment optimization. In Figure 6.3, we show the predicted pigment absorption profile and the corresponding stellar spectra on the planet's surface. The atmospheric absorption features, particularly from H_2O at 720, 820, 940, and 1130 nm (Hill & Jones, 2000; Kiang et al., 2007b), exert a strong pressure on pigments to absorb in atmospheric windows. In addition, short wavelength, high energy photons in the visible (and just beyond) provide maximum growth energy for organisms around F, G, K, and even early M stars. Only around the coolest, M5V star are organisms optimized when absorbing well into the near infrared (IR).

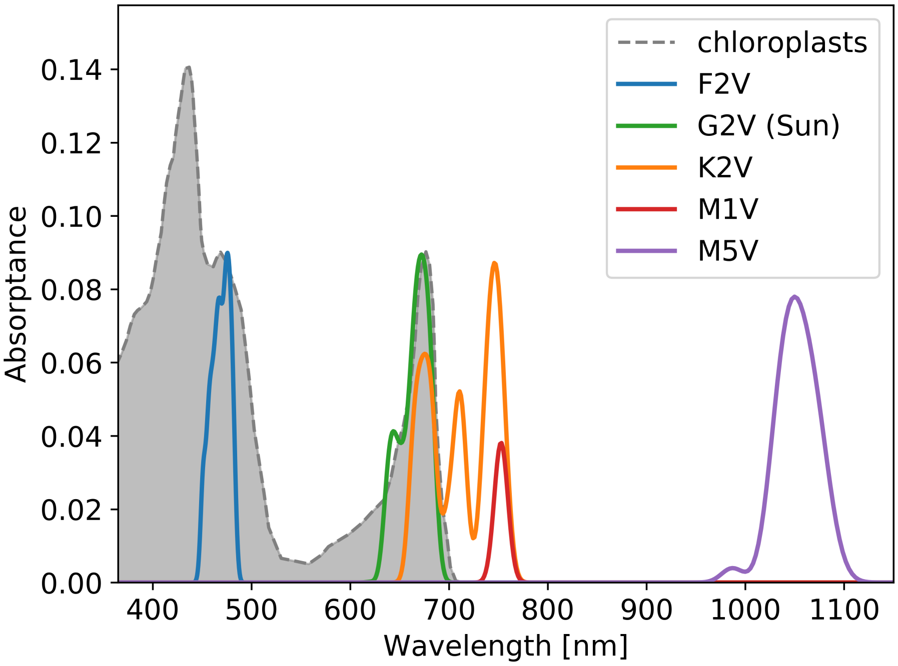

Figure 6.2: The optimal pigment absorption profile for each stellar type from our pigment optimization model (see Section 6.3). The horizontal axis shows wavelength in nm. The vertical axis shows the predicted absorptance of pigments from the model. Each colored contour represents a different stellar type, as labelled. The shaded gray region and dashed gray line show the absorptance of spinach chloroplasts from Marosvölgyi & van Gorkom (2010), arbitrarily normalized to match the vertical extent of the optimal pigment profile for Earth. The absorption profiles were smoothed by convolution with a 10 nm wide Gaussian function, following Marosvölgyi & van Gorkom (2010). The model predicts the wavelength of peak absorption and the corresponding absorption shape around that peak. The total absorptance of an organism is not reflected by the vertical axis. An organism could produce additional pigments to boost total absorptance, but the optimized absorption peak and shape would remain the same. The position of and shape of chl *a* absorption at ∼680 nm (dashed gray contour) is predicted in both location and shape by the model (green contour).

6.5 Discussion

If we are to detect a sharp change in reflectance spectra from alien, photosynthetic organisms, i.e., a “red edge” analog, knowing the exact wavelengths to observe is critical as the spectral

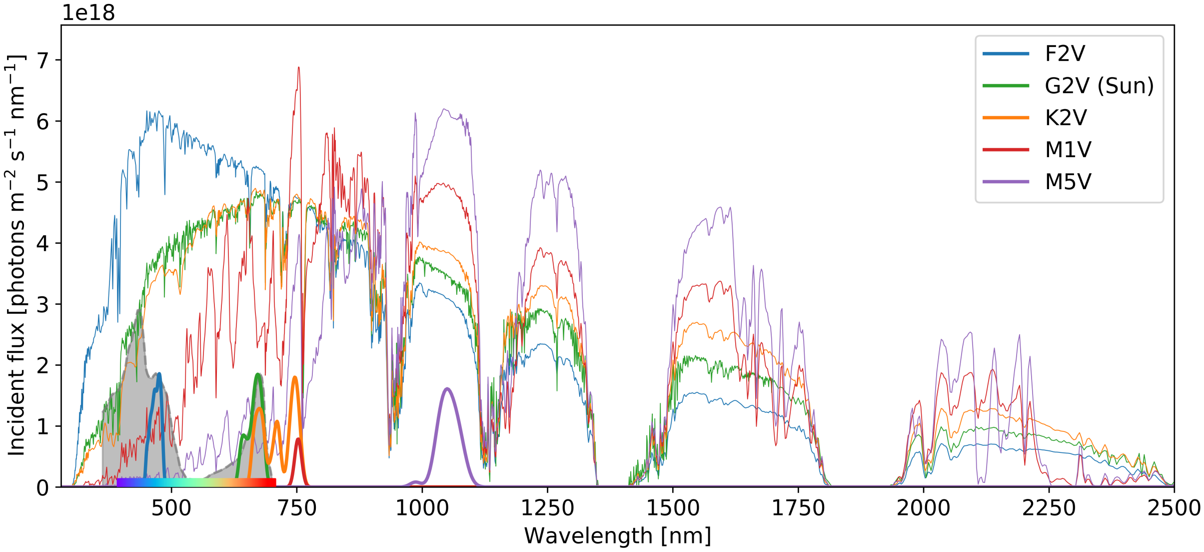

Figure 6.3: The optimal pigment absorption profile for each stellar type from Figure 6.2 with stellar spectra shown. The horizontal axis shows wavelength in nm. The vertical axis shows the incident photon flux, taken from Figure 6.1. The predicted pigment absorptance profile for each stellar type is shown in the same color. The vertical scaling of these absorptance profiles from Figure 6.2 is arbitrary as the wavelength of peak absorption and the shape of the absorption peak for each stellar type are the quantities of interest, which are agnostic of the vertical scaling. The dashed gray contour and shading shows the absorption profile of spinach chloroplasts from Marosvölgyi & van Gorkom (2010). The optimal absorption profile predicted by the model shows how pigments should be tuned to avoid atmospheric absorption if they are to maximize growth. Section 6.7.2 has each stellar spectra and corresponding optimal absorption profile shown individually, for clarity.

signal may be small (Sagan et al., 1993; Seager et al., 2005; Kiang et al., 2007a; O'Malley-James & Kaltenegger, 2018). In this work, the goal of predicting pigment absorption profiles is to inform the wavelength ranges future observations should preferentially consider for detection of a "red edge" analog.

In Section 6.4, for a given stellar type and atmosphere, we predicted the optimal pigment absorption profile, which is inversely proportional to reflectance. Indeed, on the modern Earth, the "red edge" in the near-IR corresponds to the steep drop in absorption beyond the optimal peak of chl *a* (gray shaded region in Figure 6.2). If photosynthetic organisms around other stars exhibit similar absorption behavior, we might expect "red edges" to occur on the long-wavelength side of the optimal pigment absorption, similar to the prediction of Tinetti et al. (2006).

A "red edge" at the long-wavelength limit of the optimal absorption peak does not preclude the presence of accessory pigments that absorb at shorter wavelengths. This is the case for terrestrial organisms, such as land plants, which have abundant accessory pigments throughout the visible spectrum. Indeed, green plants absorb almost all visible photons, including ∼95% of green photons (e.g. Björn et al., 2009), with the help of these accessory pigments. The energy produced from photon absorption by these pigments is stepped down via resonant transfer to be used in the photosynthetic reaction center (e.g. Kiang et al., 2007b). Effectively, after energy loss as heat, the absorption of short-wavelength photons is energetically equivalent to an organism gathering more red photons.

It is not surprising that green land plants contain these accessory pigments. If chl *a* bearing organisms were limited to the narrow range of photons around the absorption peak at ∼680 nm, say photons between 670 and 690 nm, $\sim 9 \times 10^{19}$ photons m^{-2} s^{-1} would be available from the spectra in Figure 6.1 for the Earth around the Sun. To first order, this is only $\sim \frac{1}{4}$ of the current photon use by the terrestrial biosphere (3.26×10^{20} photons m^{-2} s^{-1}) (Field et al., 1998; Lehmer et al., 2018). Without accessory pigments, terrestrial, chl *a*-bearing organisms would not be fully exploiting available light and potential growth. Instead, land plants appear to have adapted by adding accessory pigments until photon absorption is no longer growth limiting and nutrient availability, often bioavailable phosphorous or nitrogen on Earth (e.g. Reinhard et al., 2016), limits growth.

In addition to absorption of short-wavelength photons from accessory pigments, large pigments, such as chl *a*, should have auxiliary, short-wavelength absorption features (e.g. Papageorgiou, 2004). Pigments like chl *a* must be sufficiently large that their π-electrons can be excited by long-wavelength photons at the edge of the visible spectrum (e.g. Mauzerall et al., 1976). This large structure results in additional absorption features from higher energy electron orbitals (e.g. Björn et al., 2009). So the absorption of blue photons by chl *a*, which provides additional photon harvesting for a chl *a*-bearing organism similar to an accessory pigment, may be a side-effect of the structure of chl *a* being tuned to optimally absorb in the red rather than a feature that was selected for (Marosvölgyi & van Gorkom, 2010).

If alien photoautotrophs have abundant accessory pigments and auxiliary, short-wavelength absorption features in their pigments, as occur on Earth, Earth-like planets around the stars considered here would have sufficient spectral energy to sustain the Earth's extant biosphere. If we assume photons longer than 300 nm may be used by photosynthetic organisms (McCree, 1971), more than double the current photon use of the terrestrial biosphere is available for each stellar type shown in Figure 6.3. This assumes absorption only occurs between 300 nm and the optimal wavelength shown in Figure 6.2. Even if we account for the reduced quantum yield of the M5V pigment, which may be $\sim$50% as productive due to the lower quantum yield of low-energy, long-wavelength photons (Wolstencroft & Raven, 2002; Kiang et al., 2007b; Lehmer et al., 2018), no spectral energy limitation on growth is encountered, although the total flux may be a constraint around the coolest of stars (Lehmer et al., 2018). Thus, it may be unlikely for an organism to produce pigments absorbing beyond the optimal pigment absorption wavelength. Such pigments may need to be large to absorb the longer wavelength photons and thus could be costly for the cell to build. In addition, these pigments would absorb lower-energy photons and potentially have a lower quantum yield compared to accessory pigments at short wavelengths, where photons are still abundant.

The full reflectance spectra of an organism is derived not only from its pigments. As noted by Kiang et al. (2007b), cellular structure, and in the case of land plants, canopy structure and leaf morphology could play important roles in determining the reflectance spectra and thus the "red edge". These aspects are not considered in our model so the discussion of the "red edge" location should be considered approximate. However, given the lack of understanding on how these other properties may alter the "red edge" around different stars (Kiang et al., 2007b), we propose the long-wavelength limit of the optimal absorption peak is a reasonable initial location to search for a vegetative "red edge", as is the case on on the modern Earth.

6.6 Conclusion

Future exoplanet observations may search for a vegetative "red edge", a spectral signature due to a sharp slope in the reflectance of pigments in photosynthetic organisms (e.g. Sagan et al., 1993; Seager et al., 2005; Kiang et al., 2007b; O'Malley-James & Kaltenegger, 2018). The wavelength where a "red edge" analog occurs on other planets will likely depend on the stellar type and the composition of the planets' atmosphere (Sections 6.4 and 6.5). Direct imaging mission concepts, such as NASA's HabEx and LUVOIR, could constrain the surface photon flux of habitable worlds and search for a vegetative "red edge" based on that measurement, as modeled here.

The exact nature of oxygenic photosynthesis, why certain absorption features exist and what drives accessory pigment production remains under investigation (e.g. see reviews Björn et al., 2009; Björn & Ghiradella, 2015). However, the model described in this work and similar models can explain the absorption features, at least in part, of numerous extant Earth organisms (Björn, 1976; Stomp et al., 2007; Kiang et al., 2007a; Milo, 2009; Marosvölgyi & van Gorkom, 2010). We thus propose the best candidate for a photosynthetic "red edge" on habitable exoplanets occurs on the long-wavelength edge of the optimal absorption peak as depicted in Figure 6.2.

6.7 Supplemental figures

6.7.1 Cost Parameter Variations

The relative cost of the the photosynthetic apparatus, C, in equation 6.4 can vary between 0 and 1, inclusive. Marosvölgyi & van Gorkom (2010) found that for $C = 0.962$ equation 6.4 could reproduce the absorption profiles, at least in part, of multiple extant pigments. As C increases, equation 6.4 predicts pigment absorption should focus on spectral regions where the balance between photon absorption and thermal emission maximizes energy input to the cell. Thus, pigment absorption profiles should jump across atmospheric absorption bands.

Figure 6.4 shows the different model predicted absorption profiles for various values of C for the Solar spectra shown in Figure 6.1. As cost increases, Figure 6.4 clearly shows pigment absorptance jumping the atmospheric absorption features, such as those of O_2 at 688 and 761 nm and from H_2O at 720, 820, and 940 nm (Hill & Jones, 2000; Kiang et al., 2007b). Figures 6.5, 6.6, 6.7, and 6.8 show the same cost variation as Figure 6.4 but for the other spectral fluxes shown in Figure 6.1.

As wavelength increases, blackbody emission of the organism becomes increasingly important. Even in the scenario of no cost, $C = 0$, no pigment absorption is predicted beyond ∼1100 nm for the modern Earth around the Sun. Beyond this wavelength, there are insufficient photons to make up for the emissions from the pigments. Thus, in this model, pigments cannot absorb beyond ∼1100 nm without a loss of energy. This limit agrees with extant Earth organisms and theoretical calculations of the long-wavelength limit of light-driven energy production (Marosvölgyi & van Gorkom, 2010). For different stellar types this limit will change based on the incident flux of infrared photons.

The incident photon fluxes for each stellar type considered in this work are shown in Figures 6.9, 6.10, 6.11, 6.12, and 6.13. The contours in these figures are the same contours as shown in Figure 6.3, but shown individually for clarity. The model calculated wavelength of optimal pigment absorption and the shape of the absorption profile around that peak are also shown in each figure.

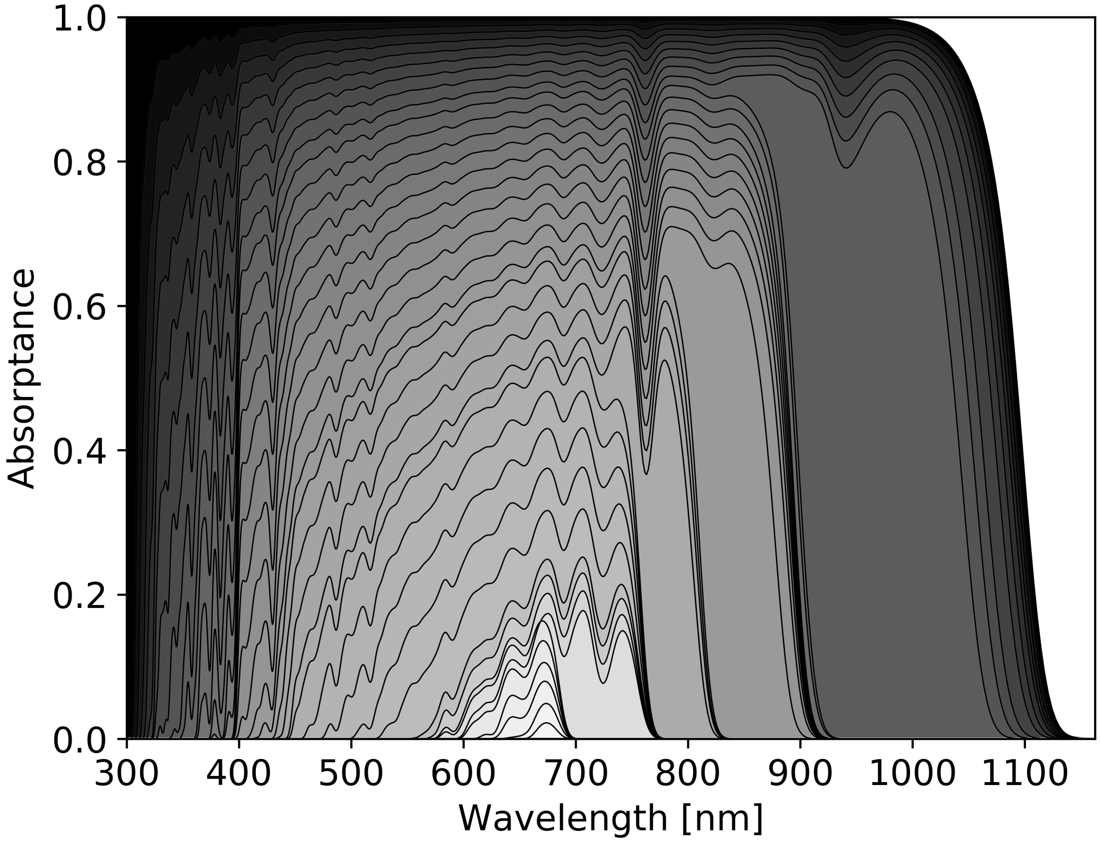

Figure 6.4: The optimal pigment absorption profile for different cost parameters around the Sun, a G2V star. The horizontal axis shows wavelength in nm, the vertical axis shows pigment absorptance. Each black curve shows the predicted pigment absorptance for the given cost parameter, C from equation 6.4. The value of C is indicated by the shading where darker shading indicates lower cost. The black shading corresponds to no cost, i.e. $C = 0$, shading approaches white as the cost increases, i.e. $C \to 1$. The predicted absorption profile was smoothed by convolution with a 10 nm wide Gaussian function. This figure recreates the results of Marosvölgyi & van Gorkom (2010), see their Figure 2.

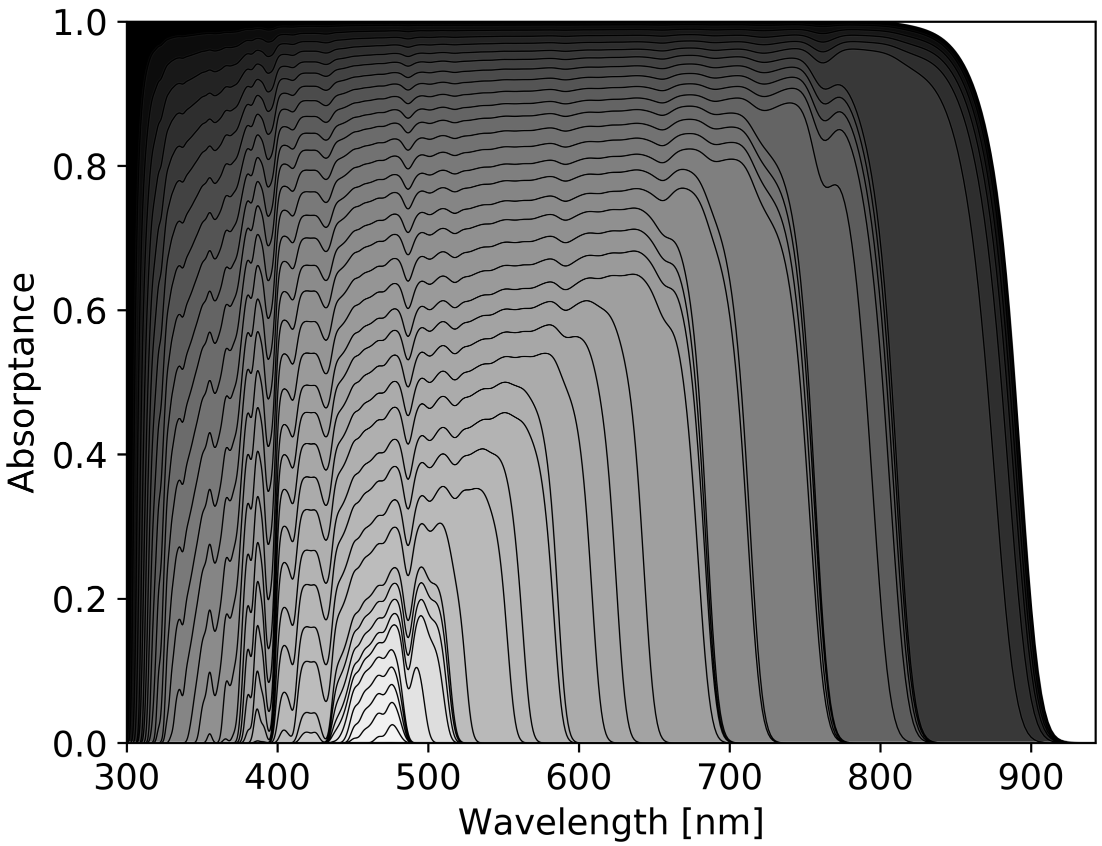

Figure 6.5: The optimal pigment absorption profile for different cost parameters around an F2V star. See Figure 6.4 for a full description.

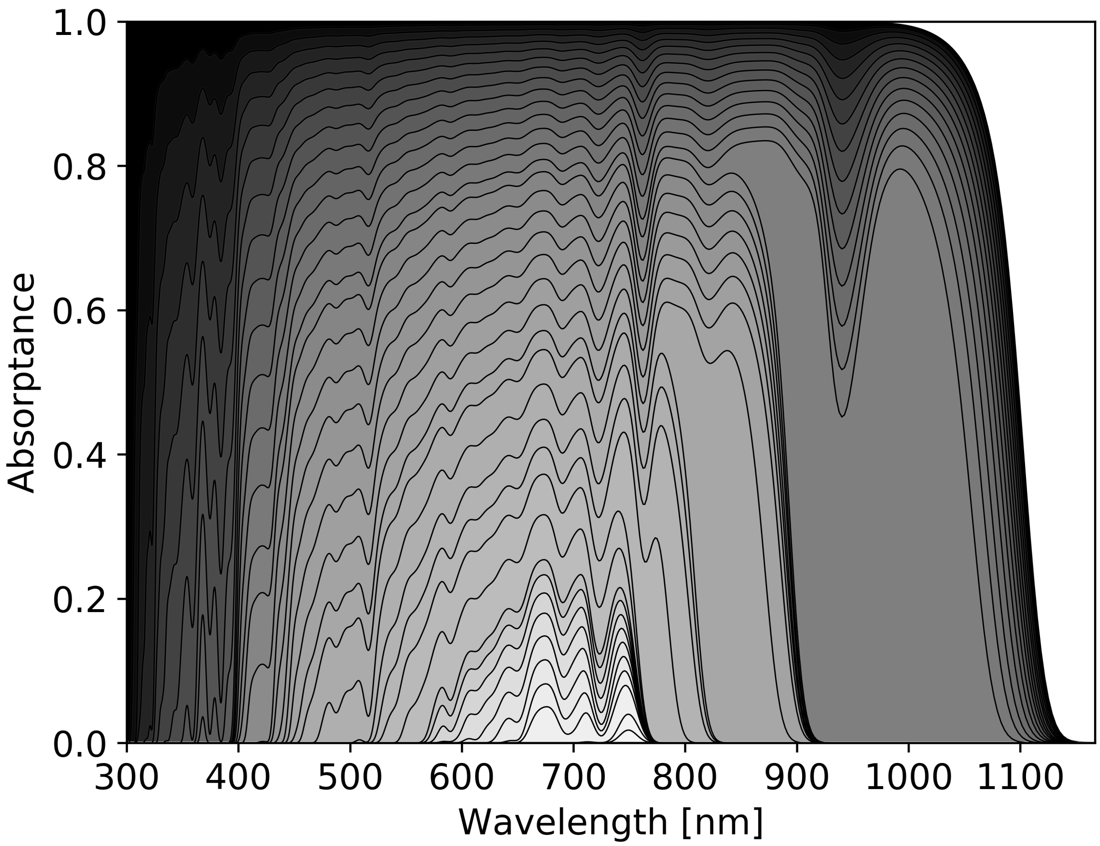

Figure 6.6: The optimal pigment absorption profile for different cost parameters around an K2V star. See Figure 6.4 for a full description.

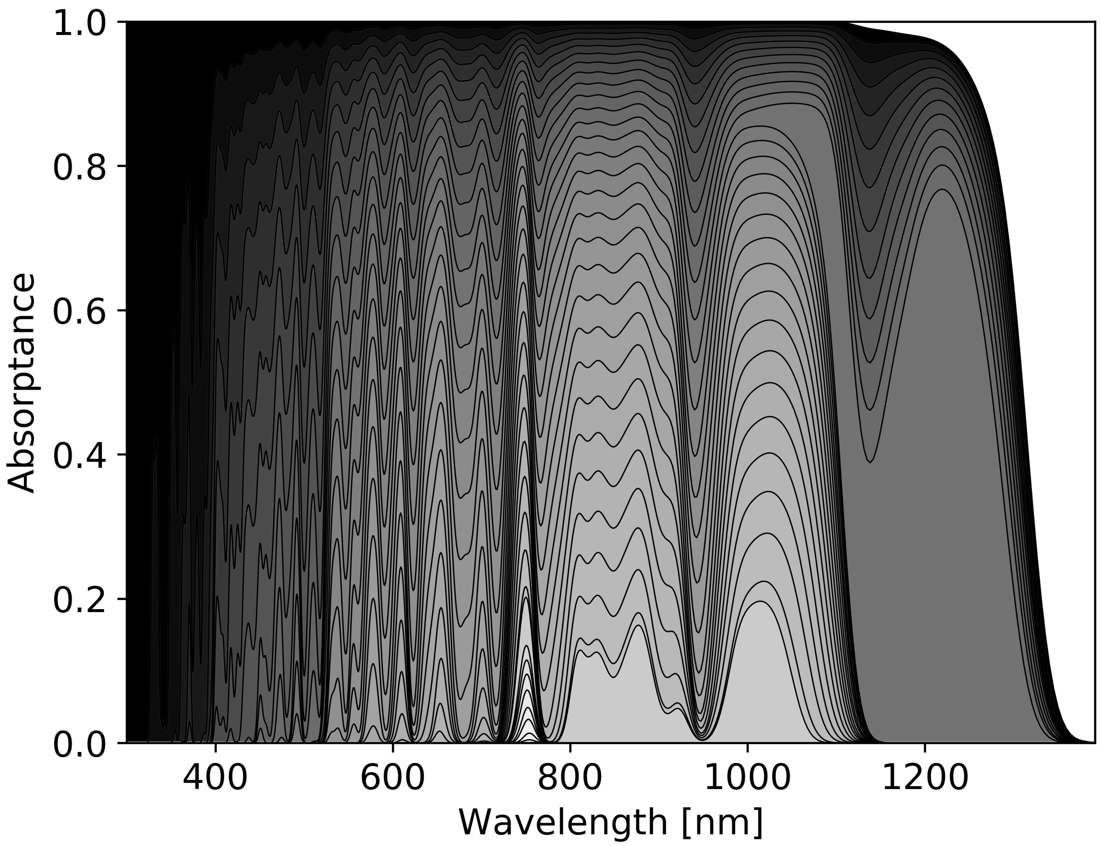

Figure 6.7: The optimal pigment absorption profile for different cost parameters around an M1V star. See Figure 6.4 for a full description.

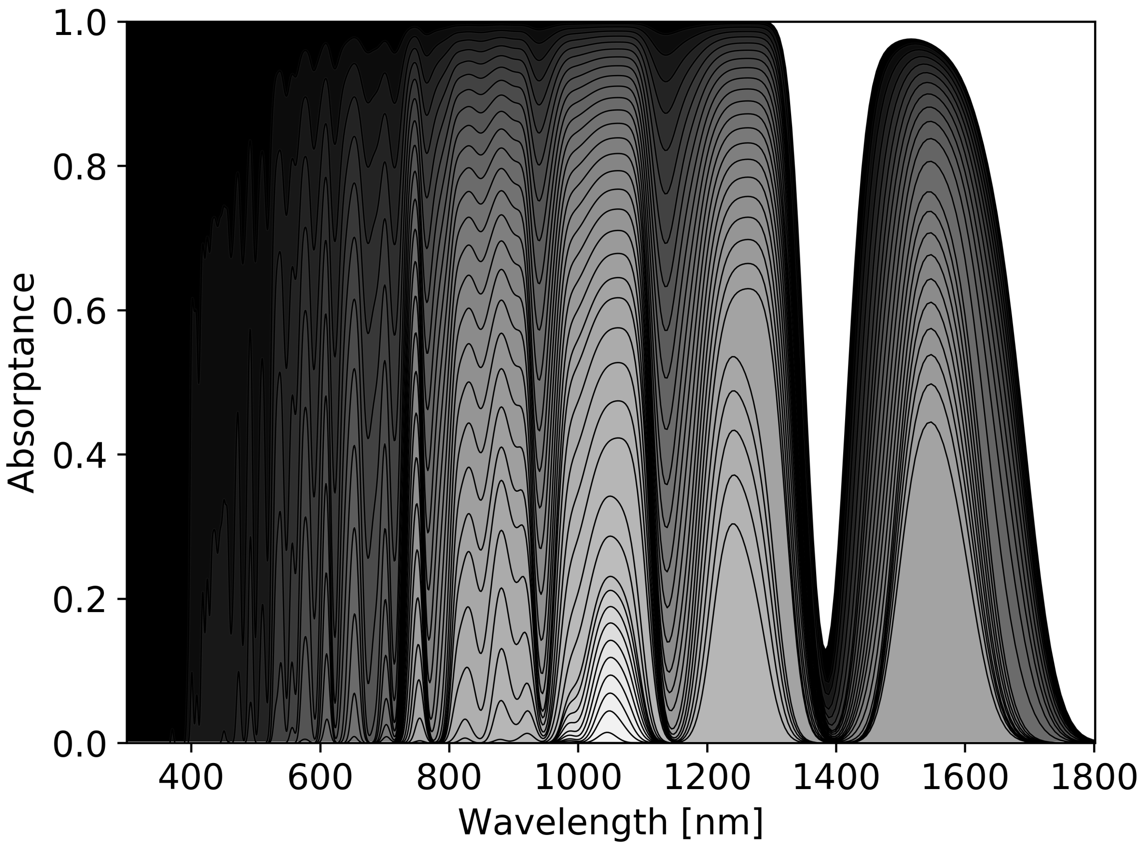

Figure 6.8: The optimal pigment absorption profile for different cost parameters around an M5V star. See Figure 6.4 for a full description.

6.7.2 Individual Spectra

Each stellar type shown in Figure 6.3 is shown in its own figure here.

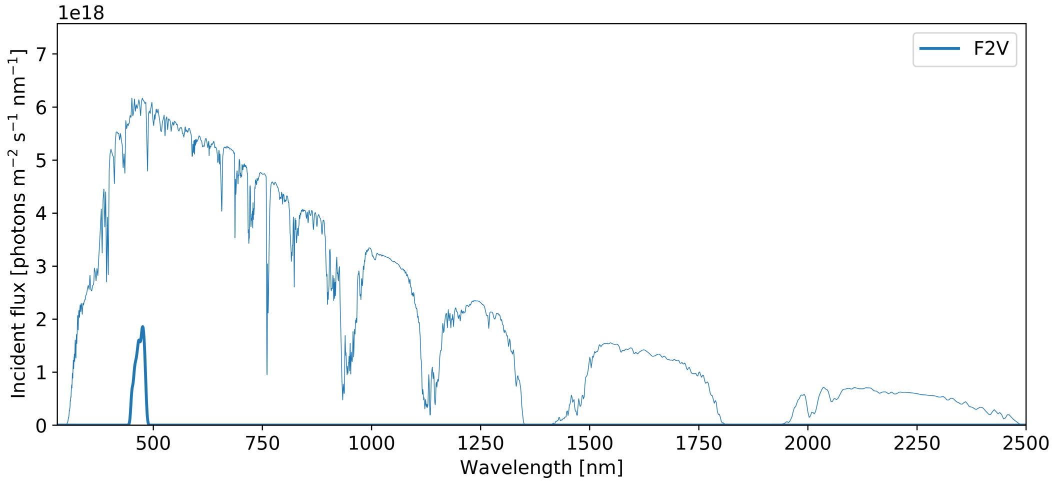

Figure 6.9: The predicted optimal pigment absorption profile for an F2V star from Figure 6.3.

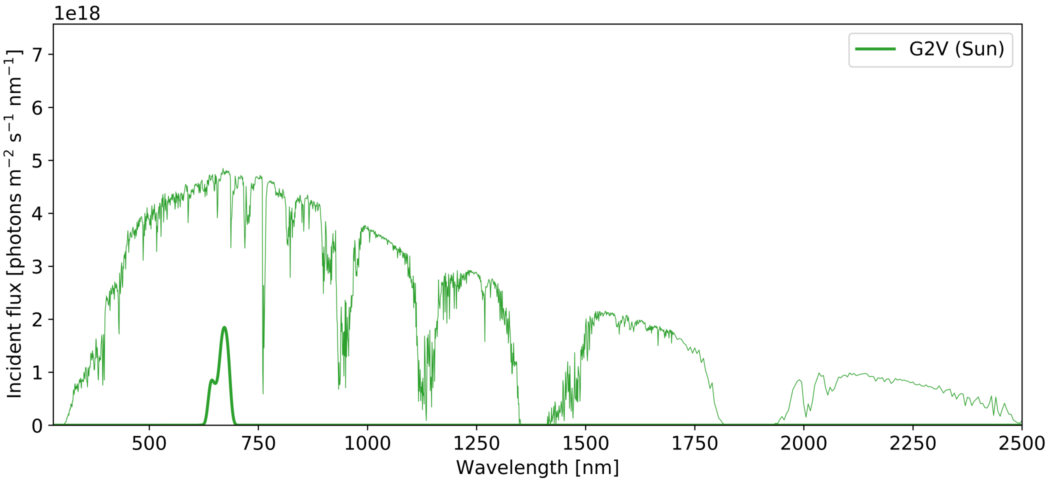

Figure 6.10: The predicted optimal pigment absorption profile for an G2V star, the Sun, from Figure 6.3.

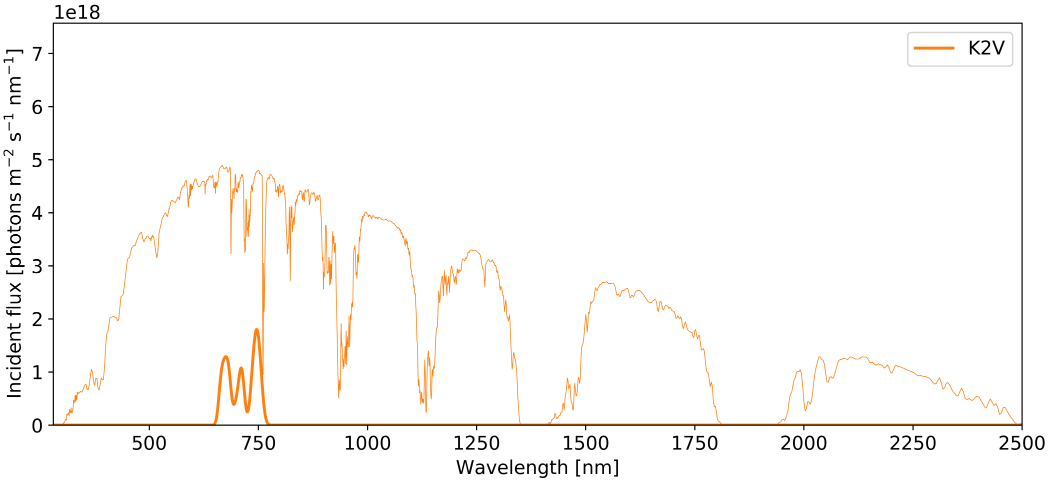

Figure 6.11: The predicted optimal pigment absorption profile for an K2V star from Figure 6.3.

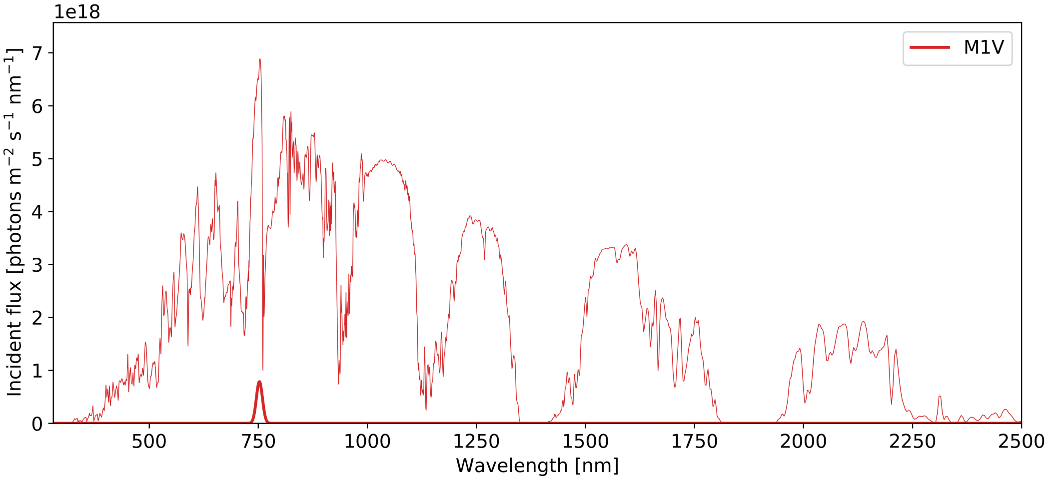

Figure 6.12: The predicted optimal pigment absorption profile for an M1V star from Figure 6.3.

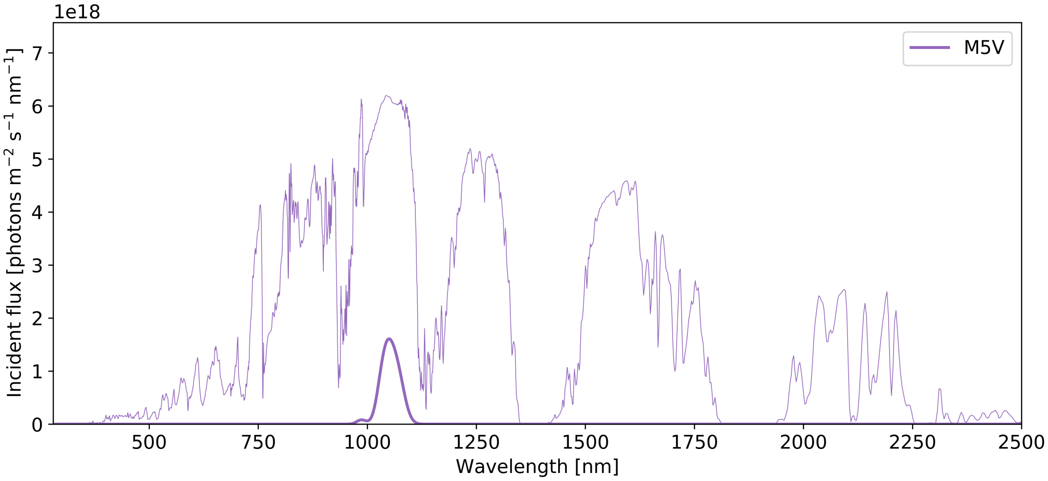

Figure 6.13: The predicted optimal pigment absorption profile for an M5V star from Figure 6.3.

Chapter 7

LIGHT-LIMITED BIOSPHERES

Status

This work was published under the title *The Productivity of Oxygenic Photosynthesis around Cool, M Dwarf Stars* by **Owen R. Lehmer, David C. Catling, Mary N. Parenteau, and Tori M. Hoehler**. It was published in *The Astrophysical Journal* in **2018**. See the reference Lehmer et al. (2018).

7.1 Abstract

In the search for life around cool stars, the presence of atmospheric oxygen is a prominent biosignature as it may indicate oxygenic photosynthesis (OP) on the planetary surface. On Earth, most oxygenic photosynthesizing organisms (OPOs) use photons between 400 and 750 nm, which have sufficient energy to drive the photosynthetic reaction that generates O_2 from H_2O and CO_2. OPOs around cool stars may evolve similar biological machinery capable of producing oxygen from water. However, in the habitable zones (HZ) of the coolest M dwarf stars, the flux of 400-750 nm photons may be just a few percent that of Earth's. We show that the reduced flux of 400-750 nm photons around M dwarf stars could result in Earth-like planets being growth limited by light, unlike the terrestrial biosphere, which is limited by nutrient availability. We consider stars with photospheric temperatures between 2300K and 4200K and show that such light-limited worlds could occur at the outer edge of the HZ around TRAPPIST-1-like stars. We find that even if OP can use photons longer than 750 nm there would still be insufficient energy to sustain the Earth's extant biosphere throughout the HZ of the coolest stars. This is because such stars emit largely in the infrared and near infrared, which provide sufficient energy to make the planet habitable, but limits

the energy available for OP. TRAPPIST-1f and g may fall into this category. Biospheres on such planets, potentially limited by photon availability, may generate small biogenic signals, which could be difficult for future observations to detect.

7.2 Introduction

Biomass production on the modern Earth is dominated by organisms doing oxygenic photosynthesis (OP). In its most basic form, OP produces organic matter by the simplified reaction (e,g, Falkowski & Raven, 1997, p. 2)

$$CO_2 + H_2O + h\nu \rightarrow CH_2O + H_2O + O_2 \tag{7.1}$$

where $h\nu$ represents a collection of photons with sufficient energy to drive the photosynthetic reaction. Though there are uncertainties in the primary productivity from OP on the modern Earth (e.g. Chen Jing M. et al., 2012; Frankenberg Christian et al., 2011; Prokopenko Maria G. et al., 2011), to a first order approximation biomass production is split roughly equally between ocean and terrestrial organisms, generating ∼1014 kg year^{-1} of biomass (Field et al., 1998). The total biomass generated by these oxygenic photosynthesizing organisms (OPOs) on the modern Earth is limited by nutrients, often bioavailable phosphorus or nitrogen, and not by energy input (e.g. Agren et al., 2012; Reinhard et al., 2016; Tyrrell, 1999). In fact, the majority of OPOs on the Earth use only a few percent of the incident photosynthetically active radiation (PAR) (Field et al., 1998), defined as photons between 400 and 750 nm (e.g. Blankenship & Chen, 2013; Chen & Blankenship, 2011; Pettai et al., 2005).

Around stars cooler than the Sun, would the biomass productivity of an Earth-like planet be similarly constrained by nutrients or by light? More specifically, if the modern Earth were placed around a TRAPPIST-1-like star with a photospheric temperature of ∼2500 K (Gillon et al., 2017), could its biomass production be maintained? For the modern Earth to be growth limited by light rather than nutrients, the PAR flux must be less than the current use by extant OPOs. We call such a biosphere potentially light-limited, where the flux of PAR photons is less than the number of photons used for OP by the modern Earth's biosphere.

Orbiting the Sun, the modern Earth is far from being potentially light-limited. Even if the planet were moved to the outer edge of the Sun's habitable zone (HZ) it would still have sufficient photons to sustain the extant biosphere (assuming no limitation by nutrients or other factors), as shown in Figure 7.1. However, if the Earth were placed around cooler stars, the green and blue dots in Figure 7.1 would move closer to the host star, potentially entering the HZ of the star.

For constant total incident photon flux on a planet, the PAR flux decreases with stellar temperature so planets in the HZ of cool stars like TRAPPIST-1 may be potentially light-limited, especially toward the outer edge of the HZ. Of course, the biospheres could be even more limited if the supply of nutrients is less than the modern Earth, e.g., a water-covered world with no continents from which to weather phosphorus, which are the sole source of phosphorus to the oceans on the modern Earth (e.g. Ruttenberg, 2014; Catling & Kasting, 2017, p. 297). Consequently, the limit being considered here can generally be taken as a conservative upper limit.

7.2.1 Photon requirements for oxygenic photosynthesis

At the outer edge of the HZ around TRAPPIST-1-like stars, the photon flux in the 400-750 nm range is only a few percent that of Earth's. Any Earth-like planets orbiting in this region must expand the range of photons usable by OPOs to avoid a potentially light-limited biosphere. However, if OPOs are able to use photons beyond 750 nm, then the total photon input per CO_2 fixed by equation (1) must be increased to account for the decreased photon energy at long wavelengths. While OPOs on Earth use 8 photons in the 400-750 nm range per CO_2 fixed by equation 7.1 under ideal conditions (e.g. Hill & Rich, 1983; Kiang et al., 2007b), if OPOs were tuned to the emissions of a TRAPPIST-1-like star they could require 24-36 photons per CO_2 fixed by equation 7.1 to have the same total energy input (e.g. Kiang et al., 2007b; Wolstencroft & Raven, 2002).

To determine if an Earth-like planet is potentially light-limited around cool stars, the PAR range for the star-planet system must be known. The lower PAR wavelength limit

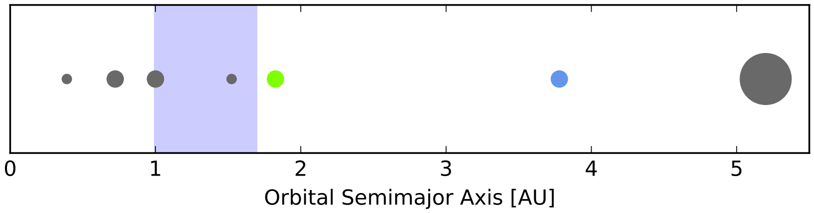

Figure 7.1: The inner Solar System in which Mercury, Venus, Earth, Mars, and Jupiter are shown in gray (planet size not to scale). The green circle shows the orbital distance at which the flux of 400-750 nm photons would be insufficient to sustain the current biomass productivity of the Earth's extant terrestrial biosphere. The blue circle shows the orbital distance where the photon flux would no longer be sufficient to sustain the modern Earth's ocean biosphere. The habitable zone for the Sun is shown by the shaded blue band from Kopparapu et al. (2013). As shown by the green and blue circles, with increasing orbital distance, solar energy flux becomes limiting to surface habitability well before it drops below levels required to support Earth's photosynthetic biosphere. Thus, the biospheres of Earth-like planets (with similar albedos and nutrient availability) in the habitable zones of Sun-like stars will not be limited by photon availability.

for other planets may be the same as on Earth, ∼400 nm. Below ∼400 nm, ultraviolet photons have an ionizing effect when absorbed by pigments, which damages the cell (e.g. Carvalho et al., 2011). This ionizing effect will occur in organic matter around other stars, so we take ∼400 nm as an approximate lower limit for PAR regardless of stellar type. We note that it may be possible for shorter wavelengths to be used, down to perhaps ∼300 nm (McCree, 1971), but the stars of interest in this study produce small photon fluxes at such short wavelengths. Indeed, the difference between a lower limit of 300 nm versus 400 nm is negligible in on our final results, so the lower limit is set at 400 nm in this study.

The upper limit of the PAR is more difficult to determine and is currently not known for Earth (e.g. Blankenship & Chen, 2013; Chen & Blankenship, 2011; Kiang et al., 2007a). It is generally found that beyond ∼680 nm the efficiency of the oxygenic photosynthetic apparatus decreases monotonically (e.g. Pettai et al., 2005). However, there are instances where the monotonic decrease abates, such as in the leaves of the sunflower plant which see a moderate boost in efficiency at 745 nm during the fall and achieve about 20% of the efficiency at 680 nm (Pettai et al., 2005). Another example is the chlorophyll *d* containing cyanobacterium *Acaryochloris marina*, which has evolved to use photons up to ∼750 nm for OP (Mielke et al., 2013). While the observed upper limit of PAR for OP in the Earth-Sun system is ∼750 nm, this limit may be different around other stars with different spectral emissions. Indeed, though not evolving oxygen, some organisms can use photons up to ∼1020 nm for anoxygenic photosynthesis indicating that an electronic excitation can be triggered at wavelengths beyond 750 nm (Björn & Ghiradella, 2015; Blankenship, 2008). Electronic excitation is required for any form of photosynthesis and becomes more difficult at longer wavelengths that can only excite vibrational or rotational transitions.

If the upper limit of the PAR changes around cooler stars, at what wavelengths would we expect OPOs to absorb in such systems? On Earth, models and in situ studies of OPOs have shown that pigments are likely optimized when they absorb at 680 nm, which is near the peak photon flux per uniform frequency interval from the Sun and precisely where chlorophyll *a* absorbs (Björn, 1976; Björn & Ghiradella, 2015; Björn et al., 2009; Kiang et al., 2007b; Marosvölgyi & van Gorkom, 2010; Milo, 2009; Ritchie, 2010; Stomp et al., 2007). It is expected that a similar pressure to evolve optimized pigments would exist around other stars, causing pigments to be tuned close to the frequency of peak photon flux per uniform frequency interval from the star (Kiang et al., 2007b, e.g.). The numerical models presented by Björn (1976) and Marosvölgyi & van Gorkom (2010) provide an elegant explanation for why OPOs absorb largely in the visible spectrum on Earth and allow us to calculate where optimized pigments should absorb around other stars, based on the spectral flux from the star.

The peak photon flux for stars cooler than the Sun falls at longer wavelengths than on Earth, often beyond 750 nm. Thus, following the models of Björn (1976) and Marosvölgyi & van Gorkom (2010), the optimal pigment absorption should fall near the peak photon flux wavelength, well past 750 nm for cool stars. If there are no physical restrictions on the upper limit of the PAR, then we expect OPOs to evolve under natural selection so that their pigments are adapted to this optimal wavelength. However, if the upper PAR limit falls below the optimal pigment absorption wavelength then OPOs would be forced to use a suboptimal portion of the spectrum, where photons may be scarce. Indeed, Kiang et al. (2007b) showed that Earth-like organisms may be ∼10% as productive around an M dwarf star where 400-700 nm photons are in short supply, but could produce Earth-like amounts of biomass if the PAR range extended to ∼1100 nm. A recent study by Ritchie et al. (2017) found that on *Proxima Centauri b* the total productivity of the biosphere could be ∼20% that of Earth's, based on the productivity of several Earth organisms.

In this study, we explore how orbital distance, stellar type, and PAR photon limits impact the photon availability of a planet, and thus its biosphere. We focus on planets with habitable environments around M dwarf stars, which may be common in our stellar neighborhood (see Shields et al. (2016) and Gale & Wandel (2017) for recent reviews M dwarf habitability). If potentially light-limited biospheres exist on these planets, then they may have only a modest impact on the planetary surface and atmosphere. Understanding the total potential biomass productivity of a planet will be an important consideration when looking for biosignatures on nearby exoplanets.

7.3 Methods

To determine if an Earth-like planet around an M dwarf star would be potentially light-limited, we must first define the light requirements of the Earth's extant biosphere. From Field et al. (1998) photoautotrophs in the ocean use 7% of the incident PAR, with the rest being either reflected or absorbed by other constituents in the water. On land (without permanent ice cover) terrestrial plants absorb 31% of the PAR (Field et al., 1998). Using the standard solar irradiance spectrum at sea level from the American Society for Testing and Materials (ASTM) (`http://rredc.nrel.gov/solar/spectra/am1.5/`), we find that 1.05×10^{21} photons m^{-2} s^{-1} are incident on the Earth's surface between 400-700 nm, which is the PAR range for chlorophyll *a* bearing OPOs that dominate primary productivity on Earth (Blankenship & Chen, 2013; Chen & Blankenship, 2011; Field et al., 1998; Raven et al., 2000). Thus, to a first order approximation, Earth's oceans require 7.35×10^{19} photons m^{-2} s^{-1} to maintain extant biomass productivity, and the terrestrial regions require 3.26×10^{20} photons m^{-2} s^{-1}.

Photosynthesis is a reaction that depends on the quantum nature of light, and is therefore measured in photons and molecules, not Watts and molecules (e.g. McCree, 1973). As such, we compare photon fluxes rather than flux densities (irradiances) (W m^{-2}) in this study.

To compare the biomass productivity of an M dwarf planet to the Earth, the photon flux available to OPOs must be known. To determine the available photon flux, we must calculate at what wavelengths OPOs should absorb photons, then compare the result to the spectral emission of the host star. For Earth, previous studies have examined this problem, which showed that pigments should absorb in spectral regions where photons capable of generating an electronic excitation are most abundant (Björn, 1976; Kiang et al., 2007a; Stomp et al., 2007; Milo, 2009; Marosvölgyi & van Gorkom, 2010; Ritchie, 2010).

The model developed by Björn (1976) provides a simple way to relate stellar temperature, T_s, and the optimal pigment absorbing frequency, by finding the frequency, ν_0, that maximizes

$$P(\nu_0) = u_{eff}(\nu_0)\nu_0^2 \exp\left(\frac{-h\nu_0}{kT_s}\right) \tag{7.2}$$

where $P(\nu_0)$ is the power output of the photosynthetic system at frequency ν_0, $u_{eff}(\nu_0)$ is the effective potential at frequency ν_0 (see Section 7.3.1 for how u_{eff} is calculated), h is Planck's constant, and k is the Boltzmann constant. Figure 7.2 shows the optimal pigment absorption wavelength across stellar type following equation 7.2 for an Earth-like planet with an incident flux equal to the modern Earth's. In Figure 7.2 we see that, if the same selective pressure to optimize pigments for peak photon flux occurs around other stars as it appears to on Earth, then pigments of OPOs around the coolest M dwarf stars should absorb well past 1μm. It should be noted that the Björn (1976) model does not account for several factors, including atmospheric absorption, so it slightly overestimates the optimal pigment absorption wavelength for Earth. Marosvölgyi & van Gorkom (2010) took the model of Björn (1976) and, by accounting for atmospheric absorption and energy to create the pigment, found that 680 nm was indeed the optimal pigment absorption wavelength. In addition, Kiang et al. (2007a) found that by accounting for atmospheric absorption the peak photon flux for OPOs occurs at ∼685 nm. As the atmospheric composition of terrestrial exoplanets remains unknown, we use the simpler model developed by Björn (1976) with the caveat that the position in wavelength of atmospheric windows could alter the predicted optimal absorption wavelength.

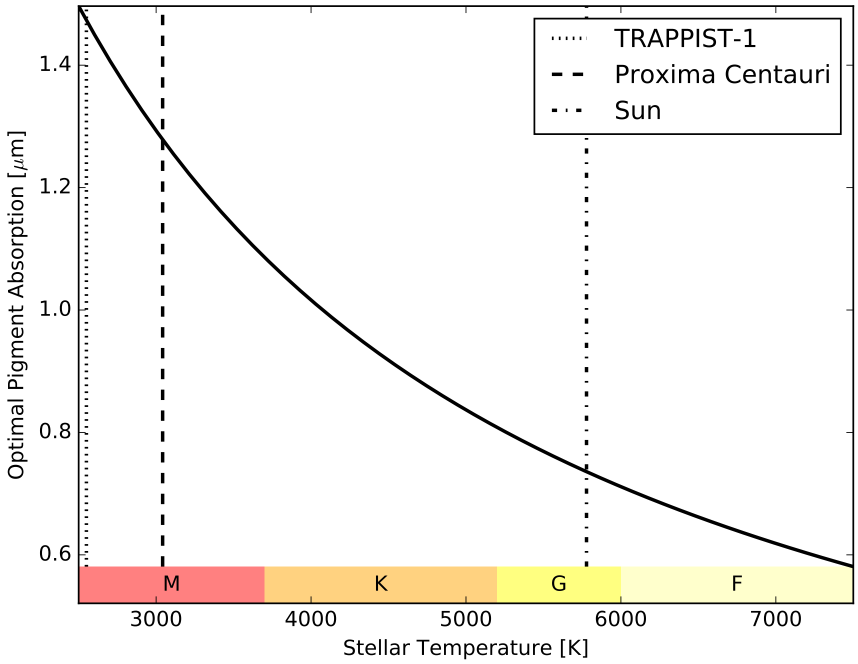

Figure 7.2: The optimal pigment absorption wavelength based on stellar temperature following Björn (1976). We assumed an Earth-like planet that orbited its host star at such a distance that the total incident flux is equal to the modern Earth's.

Could OPOs around M dwarf stars use photons past ∼1 μm and up to ∼1.5 μm for OP, as may be optimal from Figure 7.2? It remains unknown if the PAR limit for OP on Earth at ∼750 nm is a physical limit, or merely the observed limit for extant OPOs (e.g. Blankenship

& Chen, 2013; Chen & Blankenship, 2011; Kiang et al., 2007a; Wolstencroft & Raven, 2002). However, it has been proposed that OPOs could indeed use photons past 750 nm to perform OP by modifying the photosynthetic pathway to use additional, longer-wavelength photons (e.g. Kiang et al., 2007b; Wolstencroft & Raven, 2002). Given the lower energy per photon as wavelength increases, an OPO absorbing at $\sim$1.5 μm could require triple the number of photons of a similar Earth organism absorbing at 680 nm to have the same energy input for biomass productivity (Kiang et al., 2007b; Wolstencroft & Raven, 2002).

At longer wavelengths, photons have less energy so more photons must be absorbed to provide the same total energy needed to drive equation 7.1 to make O_2. OP on the modern Earth uses a 2-step photosynthetic pathway to convert CO_2 and H_2O to O_2 and organic matter (see Falkowski & Raven (1997, Ch. 4) for a review of the 2-step "Z-scheme" for OP). To produce the same biomass at longer wavelengths where additional photons are required, a 3-step photosystem could be used for photons up to $\sim$1040 nm, a 4-step system for photons up to $\sim$1400 nm, and a 6-step system for photons up to $\sim$2100 nm (Kiang et al., 2007b) if electronic excitation is still possible. We term this increased photon requirement at longer wavelengths the photon energy scaling parameter and denote it with ϵ. The ϵ term does not consider the increased energy requirements of the cell to build additional steps in the photosynthetic pathway (or, indeed, whether it is even plausible that organisms can evolve such complex, multistep photosystems), so the resultant calculation reflects an upper bound on the efficiency as wavelength increases. Takizawa et al. (2017) note that it may be possible for the current 2-step system to be modified such that additional photons may be absorbed without additional reaction centers, but even in this case the total photon requirements remain the same.

While absorbing additional photons past $\sim$750 nm can provide the same total energy input, at some wavelength a photon will be incapable of driving photosynthesis no matter how many photons are absorbed. The cutoff occurs because a photon must have sufficient energy to cause an electronic excitation in the absorbing pigment. It has been pointed out by some studies (e.g. Gale & Wandel, 2017) that a water molecule typically requires at least 1.23

eV to split, corresponding to a photon of ∼1 μm, which could be a potential wavelength limit for OP. However, it is a common misconception that photons absorbed during photosynthesis split a water molecule directly. Rather, photons are absorbed by the light harvesting pigment which causes an electron to move down a biochemical pathway before reducing CO_2. The pigment's electron is replaced by one from the reductant, H_2O in this case (see Falkowski & Raven (1997, Ch. 3) for a discussion of the topic). The upper wavelength limit for OP, where a photon triggers an electronic excitation in the absorbing pigment, is unknown but it could be greater than ∼1 μm. For completeness, without providing theoretical or experimental justification, Heath et al. (1999) state that oxygenic photosynthesis may be possible with photons up to 2.1 μm.

It is difficult to know where the wavelength limit of photosynthesis falls in theory, given the vast possibilities for pigment construction. In practice, there appear to be limits well below 2.1 μm, and even below ∼1.5 μm, which is the longest optimal wavelength we would expect around even the coolest M dwarf stars (we do not consider LTY stars in this study). The best manmade sensors are unable to detect any electronic excitations (a requirement for photosynthesis) with photons beyond 1.1 μm (Kiang et al., 2007b). While this may be a limit of human ingenuity, pigments on Earth have encountered a similar barrier as no organism has been found that utilizes photons much past ∼1 μm for photosynthesis of any kind. As mentioned previously, for anoxygenic photosynthesis, the longest known wavelength limit is at 1020 nm using bacteriochlorophyll *b* (e.g. Björn & Ghiradella, 2015; Blankenship, 2008). On some planets, the PAR limit for OP may be well below even the ∼1100 nm limit of detectable electric transitions. By approaching the photosynthetic apparatus as a thermodynamic system, van Grondelle & Boeker (2017) found that if a pigment is tuned to wavelengths beyond 900 nm for OP, back reactions at night will become more efficient than the daily energy production making any such system energetically unfavorable. This 900 nm limit may not apply to synchronously rotating planets as the OPOs are unlikely to be subjected to prolonged periods of darkness. However, on planets that are locked in a 3-2 spin-orbit resonance or other non-synchronously rotating resonances, which may be common around M dwarf stars (e.g. Shields et al., 2016), such a wavelength limit could be imposed.

We consider four possible wavelength limits for OP, denoted by L_λ. The first case is the current limit found on the modern Earth at $L_\lambda = 750$ nm. The second limit is at $L_\lambda = 900$ nm, which is the limit found by van Grondelle & Boeker (2017) for OPOs exposed to a diurnal cycle. The third limit we consider is the limit of detectable electronic transitions at $L_\lambda = 1100$ nm, and the final limit we consider is at $L_\lambda = 1500$ nm, which is beyond the optimal pigment absorption of even the coolest M dwarf stars (see Figure 7.2) which are found at ~2300 K (e.g. Kaltenegger & Traub, 2009). Table 7.1 shows ϵ for the various wavelength limit values, L_λ, used in this study.

We approximate all stars in this study as blackbody emitters and compute the optimal pigment absorption wavelength from equation 7.2. Once the optimal wavelength of pigment absorption has been estimated, an appropriate ϵ is easily determined from the above limits. For example, pigments tuned to 900 nm would require a 3-step system and would thus be 2/3 as efficient as the 2-step system on Earth, giving $\epsilon = 2/3$. If the optimal pigment wavelength is above L_λ, we assume OPOs on that planet will absorb at L_λ.

For each L_λ value considered, we model an Earth-like planet with a Bond albedo of 0.3 at different orbital distances around stars with photospheric temperatures between 2300 K and 4200 K. A Bond albedo of 0.3 may be too high for an Earth-twin planet around an M dwarf star as previous work has shown that, due in part to atmospheric absorption of CO_2 and H_2O in the near infrared where M dwarf stars output most of their radiation, the total reflected light should be less than around hotter stars while atmospheric absorption should be greater (Kasting et al., 1993; von Paris et al., 2013; Selsis et al., 2007; Shields et al., 2013). However, to compute the incident flux at the surface of these planets would require knowledge of the planetary atmospheric composition, which is currently unknown; in any case, if near-IR photons are absorbed in the atmosphere and thermalized, then they are unavailable to photosynthesis at the surface. Consequently, we use a Bond albedo of 0.3 as a reasonable first order approximation. We compare the incident PAR flux, which we assume encompasses wavelengths between 400 nm and L_λ, to the oceanic and terrestrial photon requirements of the modern Earth (7.35×10^{19} photons m^{-2} s^{-1} for the oceans, 3.26×10^{20} photons m^{-2} s^{-1} on land).

To calculate the flux from a star of a given temperature we must also know the star's radius. We estimate stellar radii from temperature via

$$R = 10.5440 - 33.7536X + 35.1909X^2 - 11.5928X^3 \tag{7.3}$$

(3) where $X = T/3500$ for stellar temperature T, following equation 4 of Mann et al. (2015). See Section 7.3.2 for a discussion of equation 7.3.

PAR Upper Wavelength Limit [nm]	Photon Energy Scaling Parameter [dimensionless]
$L_\lambda = 750$	$\epsilon = 1$
$L_\lambda = 900$	$\epsilon = 2/3$
$L_\lambda = 1100$	$\epsilon = 1/2$
$L_\lambda = 1500$	$\epsilon = 1/3$

Table 7.1: Wavelength limits for OP and the corresponding photon energy scaling parameter.

7.3.1 Optimal pigment model

We follow the model of Björn (1976) to calculate the optimal pigment absorption wavelength, given by equation 7.2. In that equation, effective potential u_{eff} is the total potential energy of the system corrected for loss through back reaction via fluorescence and delayed light emission. It is defined as

$$u_{eff} = \frac{u}{1 + kT/u} \tag{7.4}$$

for pigment temperature T (assumed 300 K) where

$$u = u_0 + kT \ln\left(\frac{kT}{u + kT}\right) \tag{7.5}$$

with

$$u_0 = kT \ln\left(\frac{\Phi r^2}{4R^2}\right) + h\nu_0\left(1 - \frac{T}{T_s}\right) \tag{7.6}$$

for stellar radius r and orbital distance R. The fluorescent yield is given by Φ, which was assumed to be 0.33, corresponding to chlorophyll *a* (Björn, 1976).

7.3.2 Stellar radius model

We relate stellar temperature to radius via equation 7.3 from Mann et al. (2015). However, the equation from Mann et al. (2015) is only defined for temperatures between 2700 K and 4100 K. This range excludes some of the coolest stars, such as TRAPPIST-1. There are few reliable data points to fit a model relating stellar temperature and radius below 2700 K and the spread in the data is large at such temperatures (Mann et al., 2015). To estimate the stellar radius for temperature below 2700 K, we linearly extrapolated from equation 7.3 at 2700 K through the point corresponding to TRAPPIST-1 at 2500 K. The radius of the star has only a minor effect on the result of our calculations and, even if we treated the stellar radius as constant below 2700 K, had a negligible impact on our final results. Similarly, above 4100 K we extrapolated linearly from equation 7.3 at 4100 K through the Sun.

7.4 Results

To a first order approximation, we find that an Earth-like biosphere would be potentially light-limited around the coolest of stars, regardless of the wavelength limit for oxygenic photosynthesis. This is shown in Figure 7.3, where the blue shaded regions indicate that the photon flux is beneath the usage of the terrestrial Earth. The red shaded regions in Figure 7.3 show where the incident PAR flux is below the amount used by Earth's modern oceans. If the upper limit for the PAR occurs at 750 nm (Figure 7.3A) or 900 nm (Figure 7.3B), HZ planets around cool stars could not support even the Earth's ocean biosphere. The sharp jumps in the contours of Figure 7.3C and Figure 7.3D are due to the ϵ term, which is

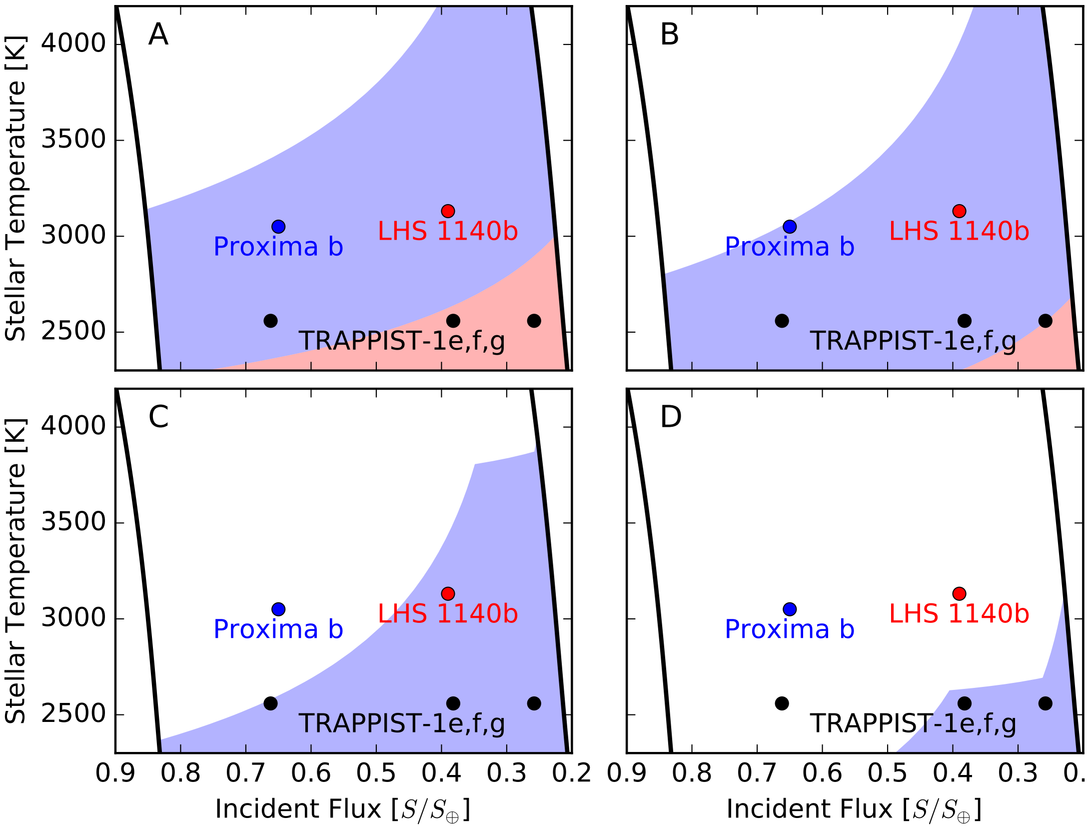

Figure 7.3: Regions around a star where biomass productivity on an Earth-like planet would be potentially light-limited compared to Earth. Regions are shown for an oxygenic photosynthetic long wavelength limit of $L_\lambda = 750$ nm in plot A, $L_\lambda = 900$ nm in plot B, $L_\lambda = 1100$ nm in plot C, and $L_\lambda = 1500$ nm in plot D. The horizontal axis shows the incident stellar flux, S, normalized by Earth's incident solar flux, $S_\oplus = 1361$ W m−2. The blue shaded regions represent PAR photon fluxes below the terrestrial limit (3.26×10^{20} photons m^{-2} s^{-1}), scaled by the wavelength efficiency factor, ϵ (see text). The red shaded regions represent PAR photon fluxes below the Earth ocean limit (7.35×10^{19} photons m^{-2} s^{-1}), scaled by the wavelength efficiency factor, ϵ. The black lines show the inner and outer limits of the habitable zone from Kopparapu et al. (2013).

changed as soon as the optimal pigment wavelength calculated from equation 7.2 crosses the ϵ thresholds. Whether such discontinuities exist in nature is unknown. Given that there are only 2-step OPOs on Earth, we do not know what the transition from a 2-step to a 3-step or 4-step photosynthetic apparatus would look like.

As seen in Figure 7.3, TRAPPIST-1 has a temperature of only ∼2500 K and the three planets that fall within the HZ, as defined by Kopparapu et al. (2013), have incident fluxes of $0.662S_\oplus$, $0.382S_\oplus$, and $0.258S_\oplus$ (Gillon et al., 2017). If any of these planets have a spin orbit resonance other than one-to-one, then they may be bound by the 900 nm limit for oxygenic photosynthesis found by van Grondelle & Boeker (2017), shown in Figure 7.3B. In this plot, all three planets would have insufficient light to maintain Earth's terrestrial biosphere, and TRAPPIST-1g would be unable to sustain Earth's current ocean biosphere. Even if the planets are synchronous rotators, and the wavelength limit for oxygenic photosynthesis is closer to 1500 nm, the outer two HZ planets of the TRAPPIST-1 system would still be unable to support Earth's terrestrial biosphere (Figure 7.3D).

7.5 Discussion

For an atmosphere to become oxygenated by OP, the rate of O_2 production must exceed the rate of consumption by kinetically efficient O_2 sinks from the environment. On the modern Earth, the O_2 produced in equation 7.1 is nearly all lost on a short timescale of $\sim 10^2$ years through the back reaction of respiration or oxidative decay of the organic matter. Only a small fraction of the total organic matter, less than a percent (Berner & Maasch, 1996), escapes respiration or oxidative decay and is buried, which provides a net source of O_2. The modern Earth produces $\sim 10^{14}$ kg yr^{-1} of organic matter (Field et al., 1998), which corresponds to a total of ∼3000 Tmol yr^{-1} of CH_2O produced via OP from equation 7.1, if we assume all organic carbon is formed as CH_2O. Estimates of the amount of organic carbon burial, and hence the net O_2 flux, range from 5.3 Tmol O_2 yr^{-1} (Berner, 2004, p. 42) to 10.0 ± 1.7 Tmol O_2 yr^{-1} (Holland, 2002), which are 0.16% and 0.30% of the total productivity, respectively, if we take the order of magnitude estimate of Field et al. (1998). In addition to burial of organic carbon, the burial of pyrite is a net source of O_2 on the modern Earth (by removing the ferrous iron reductant) that produces an equivalent 4.7 ± 1.2

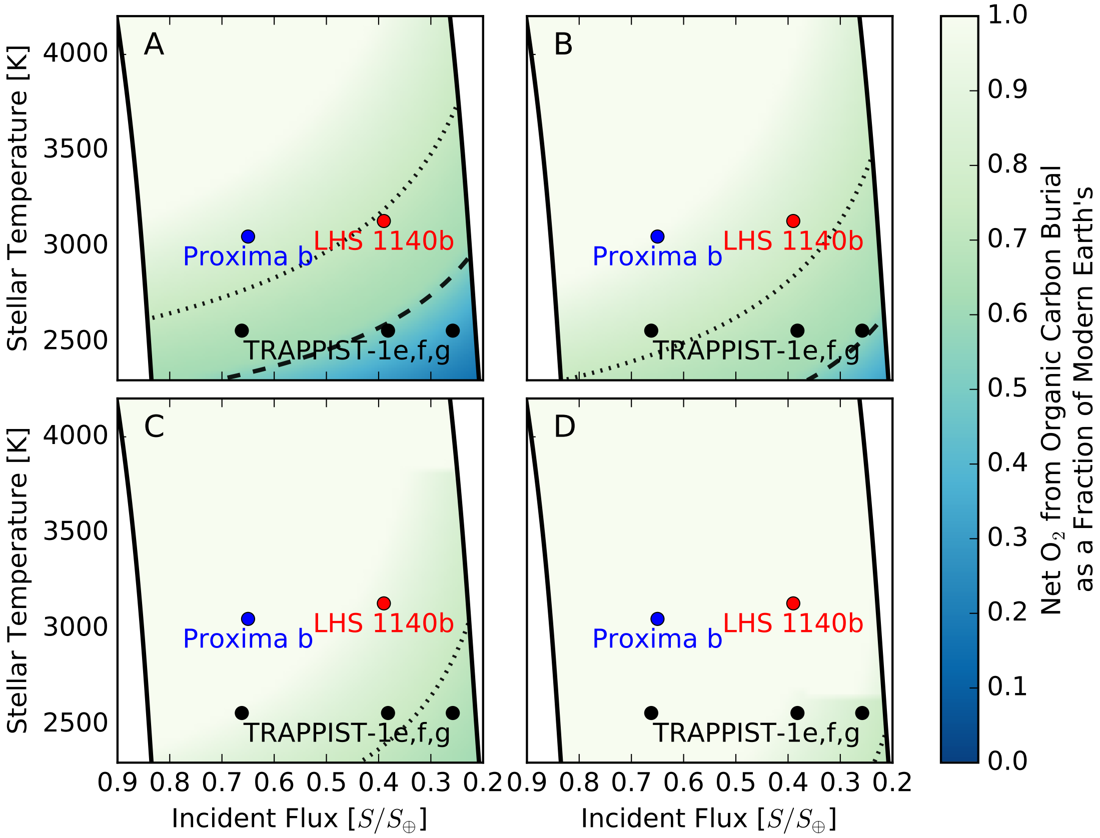

Figure 7.4: The net O_2 produced from organic carbon burial on Earth-like planets. Plots are shown for an oxygenic photosynthetic long wavelength limit of $L_\lambda = 750$ nm in plot A, $L_\lambda = 900$ nm in plot B, $L_\lambda = 1100$ nm in plot C, and $L_\lambda = 1500$ nm in plot D. The horizontal axis shows the incident stellar flux, S, normalized by Earth's incident solar flux, $S_\oplus = 1361$ W m^{-2}. The solid black lines show the inner and outer limits of the habitable zone from Kopparapu et al. (2013). The dashed black line shows the contour where the O_2 flux is equal to the assumed planetary reductant flux that efficiently removes atmospheric O_2 contributed by an organic burial rate of 0.3%. The reductant flux is a kinetically rapid sink for atmospheric O_2, which must be overcome for O_2 to accumulate in the atmosphere (see text). Planets above the dashed contour could build up atmospheric oxygen from oxygenic photosynthesis alone, while planets below the line may be unable to. The dotted black line shows the same as the dashed line, but for a burial rate of 0.23%.

Tmol O_2 yr^{-1} (Catling & Kasting, 2017, p. 262). Thus, within a large uncertainty, O_2 is generated at a rate of up to ∼15 Tmol yr^{-1} on the modern Earth with the majority coming from burial of organic carbon.

Of course, the atmosphere on the modern Earth is not gaining O_2 at ∼15 Tmol yr^{-1}. The amount of O_2 is in approximately steady state because the O_2 input is balanced by sink fluxes. On the modern Earth, ∼30% of the O_2 sink is from kinetically rapid reactions with reductants from volcanic or metamorphic emissions (e.g., H_2, CO, H_2S, SO_2, etc.) and seafloor weathering. The remaining 70% of the O_2 flux is consumed when O_2 dissolves in rainwater and reacts with reducing substances exposed on continental rocks (e.g. organic carbon and ferrous iron) in oxidative weathering. O_2 is readily consumed by this oxidative surface weathering on the modern Earth because O_2 is abundant in the atmosphere. However, in a reducing atmosphere, O_2 would largely be consumed by kinetically rapid reactions with atmospheric reductants and oxidative weathering of the planetary surface would be negligible as shown by Claire et al. (2006). Only when the flux of O_2 surpasses the flux of reducing gases will surface sinks for O_2 become important; at that point, O_2 would build up in the atmosphere and a continental oxidative weathering sink would kick-in.

In this study we are interested in the possibility of OP transforming a reducing atmosphere to an O_2 rich atmosphere as a potential biosignature. Thus, an Earth-like exoplanet must have sufficient biomass productivity that net O_2 from burial of organic carbon can overcome the reducing gas flux from the planet, which produces a combined O_2 sink of 5.7 ± 1.2 Tmol yr^{-1} on the modern Earth (Catling & Kasting, 2017, p. 264). The potentially light-limited planets considered in this study are assumed to be Earth-like and thus must generate at least 5.7 Tmol O_2 yr^{-1} for atmospheric O_2 to accumulate if we assume a kinetically rapid O_2 sink comparable to that of the modern Earth. The biomass productivity scales linearly with photon flux, shown by equation 7.1, so planets with few available photons for OP are likely unable to produce Earth-like O_2 fluxes. Assuming the planets have an Earth-like burial rate of 0.16-0.30%, we can easily compute the net O_2 from OP by following the same process used to generate Figure 7.3.

In Figure 7.4 we show how net O_2 from OP scales with stellar type and orbital distance. We plot the same wavelength limits for OP as in Figure 7.3 but show the net O_2 flux on the planet from organic carbon burial as a fraction of the modern Earth's. We assumed that, like on the modern Earth, biomass productivity was split equally between ocean and terrestrial regions. Figure 7.4 shows that, depending on L_λ, planets may produce only a few percent of modern Earth's net O_2 flux (Figure 7.4A). The dotted line in Figure 7.4 shows the point above which the O_2 flux exceeds the flux of reducing gases if the organic carbon burial rate is set to 0.23% (the average of 0.16% and 0.3%). The dashed line shows the same, but for the estimated upper limit on burial rate of 0.3%. Thus, we see that even if the burial rate is maximal for a modern Earth-like planet (0.3%), it is possible that planets like TRAPPIST-1 f and g would be growth limited by photon availability (Figure 7.4A). Under such conditions, they would be unable produce sufficient O_2 from organic carbon burial to build up atmospheric O_2.

The lower bound on burial rate, 0.16% for the modern Earth, is not shown in Figure 7.4. This is because a burial rate of 0.16% generates only ~5.3 Tmol O_2 yr^{-1} for an Earth-size biosphere. An O_2 flux of 5.3 Tmol yr^{-1} is below the 5.7 Tmol yr^{-1} sink from reducing gases and would require a biomass production greater than the modern Earth's to accumulate atmospheric O_2. A burial rate of 0.16% would preclude an oxygen rich atmosphere on any of the Earth-like planets considered in this study.

Planets with reductant fluxes greater than the net O_2 flux from organic carbon burial will be unable to produce O_2 rich atmospheres from OP. In Figure 7.4, the area under the dotted and dashed contours corresponds to Earth-like planets where this is the case. On such planets, OP could be functioning without ever producing an O_2 rich atmosphere and thus no O_2 biosignature. Planets like TRAPPIST-1e,f,g may fall into this regime, however, the flux of reducing gases from abiotic sources may be quite different on these planets than on the modern Earth. Additional studies should be conducted on reductant fluxes to determine how other planets may differ from Earth.

Even if the flux of reductants is lower on exoplanets like TRAPPIST-1e,f,g than the modern Earth and doesn't overwhelm net O_2 from OP, atmospheric oxygen may still be scarce. Atmospheric O_2 didn't build up in Earth's atmosphere until ~2.4 Ga during the

Great Oxidation Event. But various lines of geochemical evidence suggest that OP may have evolved by 2.7-3.2 Ga (Buick, 2008; Crowe et al., 2013; Farquhar et al., 2011; Planavsky et al., 2014; Satkoski et al., 2015; Stüeken et al., 2012), or possibly earlier, before even 3.4-3.8 Ga (Cardona, 2018; Frei et al., 2016; Rosing & Frei, 2004). Thus, 300 Myr or more may have passed between the advent of OP and the buildup of atmospheric O_2. The O_2 produced during this window could have been drawn down by kinetically rapid sinks at the planetary surface, like ferrous iron and reduced sulfur, that took hundreds of millions of years to overcome. If terrestrial exoplanets form with similar compositions to the Earth, they may have similar O_2 sinks that must be overcome before atmospheric O_2 can build up. If the O_2 flux from OP is only a few percent that of Earth's (see Figure 7.4) then what took perhaps a few hundred Myr on Earth could take billions of years on another planet, during which atmospheric O_2 could be negligible.

7.6 Conclusions

The energy for the vast majority of life on Earth is sustained by solar photons, either directly or through the food chain. This biosphere has altered the atmosphere and surface of the planet, making it detectable to a remote observer (e.g. Catling et al., 2018; Sagan et al., 1993; Schwieterman et al., 2018). The next generation of telescopes will look for signatures of an Earth-like biosphere on the surfaces and in the atmospheres of other planets, with atmospheric oxygen from OP being one of the most enticing biosignatures (e.g. Meadows et al., 2018a; Schwieterman et al., 2018). But detecting life may be challenging if the biosphere is limited in size. Indeed, a planet that is sustained by chemical energy alone, rather than stellar photon energy, may be so restricted in terms of biomass productivity that it would be undetectable (McKay, 2014). The potentially light-limited planets modelled in this study may fall into a similar category, where the total biosphere productivity may be small compared to natural planetary processes (see Section 7.5) and unable to generate a meaningful biosignature.

The potentially light-limited biospheres discussed in this study may be abundant around cool stars, especially if the upper limit for useable photons at ∼750 nm on Earth holds on other planets. This limit may be especially common on water rich planets as an ocean based biosphere would be limited to visible and near infrared photons, because water strongly absorbs the longer wavelength photons (e.g. Takizawa et al., 2017). If PAR is bound at ∼750 nm, all the HZ planets of the TRAPPIST-1 system fall within the potentially light-limited regime, where an Earth-like biosphere would be limited by energy input from light rather than nutrients. Even if the limit of useable photons for OP extends beyond 750 nm, the planets in the outer edge of the HZ around TRAPPIST-1-like stars are still likely unable to support an Earth-size biosphere. Future observations of the TRAPPIST-1 planets and similar systems should consider reduced biosphere productivity when looking for potential biosignatures.

Chapter 8

CONCLUSION

The previous chapters considered some of the features that habitable and inhabited worlds may exhibit. In "Radius limit for rocky planets" and "Icy moons in the habitable zone" we explored the possible size limits of habitable worlds, both for planets and icy moons. We found that habitable worlds could range in size from about Ganymede's size up to $\sim$1.8 $R_\oplus$. The radius of a planet is easily measured using the transit method (e.g. Batalha, 2014) making this constraint an ideal criteria to filter exoplanets, and even exomoons, for potentially habitable worlds. But also measuring mass to infer mean density is still desirable to know more about the kind of world (e.g. internal composition and gravity).

In "Archean carbon dioxide levels from micrometeorite oxidation" and "Carbon dioxide in the habitable zone" we saw the expected variability in atmospheric CO_2 on the Earth through time and Earth-like planets in the habitable zone (HZ). From micrometeorite oxidation, we showed the Earth's atmosphere may have been $>$70% CO_2 at 2.7 Ga, orders of magnitude larger than the atmospheric CO_2 level of the modern Earth. Our constraint on Earth's atmospheric CO_2 at 2.7 Ga in Chapter 4 could inform understanding of habitable exoplanets very different to the modern Earth (e.g. Arney et al., 2016). A similarly broad range in atmospheric CO_2 may exist on Earth-like planets in the HZ, as demonstrated with our coupled climate and carbonate-silicate weathering model. In addition, observing our predicted trend for CO_2 in the HZ from Chapter 5 could confirm the validity of the HZ hypothesis (e.g. Bean et al., 2017; Turbet, 2019).

Thematically, this work concludes by considering properties of biospheres around other stars in "Plant color around other stars" and "Light-limited biospheres". By modeling pigment optimization based on incident spectral energy distribution, we predict likely pigment absorption profiles for alien photosynthetic organisms in Chapter 6. We show these organisms may preferentially absorb blue photons around F type stars, while red photons may be optimal around G, K, and early M type stars. Around late M dwarfs, infrared (IR) photons may be optimal. A “red edge” analog may exist beyond this optimal absorption wavelength, which future missions might detect.

We extend our consideration of Earth-like biospheres around the coolest M type stars, with large IR emissions, in Chapter 7. Earth-like biospheres around these stars may be growth limited by photon availability because high-energy photons are in short supply. This photon-limited regime could result in meager biomass productivity making such biospheres difficult to detect.

From the models of habitable worlds and constraints on their potential biospheres presented in Chapters 2 through 7, future telescopes will be better equipped to target and understand potentially habitable worlds. In particular, the soon-to-launch JWST, which will target planets around M dwarf stars, may benefit from our consideration of biospheres around such stars in Chapters 6 and 7. JWST and future missions capable of observing potentially habitable planets around a wider range of stellar types, such as HabEx and LUVOIR, might test the other predictions made here as well, such as those in Chapters 2, 3, and 5. From the observations of these telescopes, habitable worlds and signs of life beyond the Earth could be found in the near future.

BIBLIOGRAPHY

Abbot, D. S., Cowan, N. B., & Ciesla, F. J. 2012, Indication of Insensitivity of Planetary Weathering Behavior and Habitable Zone to Surface Land Fraction, The Astrophysical Journal, 756, 178, doi: 10.1088/0004-637X/756/2/178

Abe, Y., Abe-Ouchi, A., Sleep, N. H., & Zahnle, K. J. 2011, Habitable Zone Limits for Dry Planets, Astrobiology, 11, 443, doi: 10.1089/ast.2010.0545

Abuluwefa, H. T., Guthrie, R. I. L., & Ajersch, F. 1997, Oxidation of low carbon steel in multicomponent gases: Part I. Reaction mechanisms during isothermal oxidation, Metallurgical and Materials Transactions A, 28, 1633, doi: 10.1007/s11661-997-0255-7

Adams, E. R., Seager, S., & Elkins-Tanton, L. 2008, Ocean Planet or Thick Atmosphere: On the Mass-Radius Relationship for Solid Exoplanets with Massive Atmospheres, The Astrophysical Journal, 673, 1160, doi: 10.1086/524925

Agren, G. I., Wetterstedt, J. A. M., & Billberger, M. F. K. 2012, Nutrient limitation on terrestrial plant growth – modeling the interaction between nitrogen and phosphorus, New Phytologist, 194, 953, doi: 10.1111/j.1469-8137.2012.04116.x

Arney, G., Domagal-Goldman, S. D., Meadows, V. S., et al. 2016, The Pale Orange Dot: The Spectrum and Habitability of Hazy Archean Earth, Astrobiology, 16, 873, doi: 10.1089/ast.2015.1422

ASTM. 2020, Reference Air Mass 1.5 Spectra | Grid Modernization | NREL. https://www.nrel.gov/grid/solar-resource/spectra-am1.5.html

Batalha, N. M. 2014, Exploring exoplanet populations with NASA's Kepler Mission, Proceedings of the National Academy of Sciences, 111, 12647, doi: 10.1073/pnas.1304196111

Bean, J. L., Abbot, D. S., & Kempton, E. M.-R. 2017, A Statistical Comparative Planetology Approach to the Hunt for Habitable Exoplanets and Life Beyond the Solar System, The Astrophysical Journal, 841, L24, doi: 10.3847/2041-8213/aa738a

Berner, R. A. 2004, The Phanerozoic Carbon Cycle: CO2 and O2 (New York, NY: Oxford University Press)

Berner, R. A., & Maasch, K. A. 1996, Chemical weathering and controls on atmospheric O2 and CO2: Fundamental principles were enunciated by J.J. Ebelmen in 1845, Geochimica et Cosmochimica Acta, 60, 1633, doi: 10.1016/0016-7037(96)00104-4

Björn, L. O. 1976, Why are plants green - relationships between pigment absorption and photosynthetic efficiency, Photosynthetica, 10, 121. http://lup.lub.lu.se/record/134648

Björn, L. O., & Ghiradella, H. 2015, in Photobiology, ed. L. O. Björn (New York, NY: Springer New York), 97–117, doi: 10.1007/978-1-4939-1468-5_9

Björn, L. O., Papageorgiou, G. C., Blankenship, R. E., & Govindjee. 2009, A viewpoint: Why chlorophyll a?, Photosynthesis Research, 99, 85, doi: 10.1007/s11120-008-9395-x

Blake, R. E., Chang, S. J., & Lepland, A. 2010, Phosphate oxygen isotopic evidence for a temperate and biologically active Archaean ocean, Nature, 464, 1029, doi: 10.1038/nature08952

Blankenship, R. E. 2008, in Molecular Mechanisms of Photosynthesis (Blackwell Science Ltd), 1–10, doi: 10.1002/9780470758472.ch1

Blankenship, R. E., & Chen, M. 2013, Spectral expansion and antenna reduction can enhance photosynthesis for energy production, Current Opinion in Chemical Biology, 17, 457, doi: 10.1016/j.cbpa.2013.03.031

Bodenheimer, P., & Lissauer, J. J. 2014, Accretion and Evolution of 2.5 M $\oplus$ Planets with Voluminous H/He Envelopes, The Astrophysical Journal, 791, 103, doi: 10.1088/0004-637X/791/2/103

Bolmont, E., Selsis, F., Owen, J. E., et al. 2017, Water loss from terrestrial planets orbiting ultracool dwarfs: implications for the planets of TRAPPIST-1, Monthly Notices of the Royal Astronomical Society, 464, 3728, doi: 10.1093/mnras/stw2578

Buchhave, L. A., Dressing, C. D., Dumusque, X., et al. 2016, A 1.9 Earth Radius Rocky Planet and the Discovery of a Non-transiting Planet in the Kepler-20 System, The Astronomical Journal, 152, 160, doi: 10.3847/0004-6256/152/6/160

Budyko, M. I. 1969, The effect of solar radiation variations on the climate of the Earth, Tellus, 21, 611, doi: 10.3402/tellusa.v21i5.10109

Buick, R. 2008, When did oxygenic photosynthesis evolve?, Philosophical Transactions of the Royal Society of London B: Biological Sciences, 363, 2731, doi: 10.1098/rstb.2008.0041

Buratti, B. J. 1991, Ganymede and Callisto: Surface textural dichotomies and photometric analysis, Icarus, 92, 312, doi: 10.1016/0019-1035(91)90054-W

Cardona, T. 2018, Early Archean origin of heterodimeric Photosystem I, Heliyon, 4, e00548, doi: 10.1016/j.heliyon.2018.e00548

Carvalho, A. P., Silva, S. O., Baptista, J. M., & Malcata, F. X. 2011, Light requirements in microalgal photobioreactors: an overview of biophotonic aspects, Applied Microbiology and Biotechnology, 89, 1275, doi: 10.1007/s00253-010-3047-8

Catling, D. C., & Kasting, J. F. 2017, Atmospheric Evolution on Inhabited and Lifeless Worlds (New York: Cambridge University Press)

Catling, D. C., Krissansen-Totton, J., Kiang, N. Y., et al. 2018, Exoplanet Biosignatures: A Framework for Their Assessment, Astrobiology, doi: 10.1089/ast.2017.1737

Cecchi-Pestellini, C., Ciaravella, A., & Micela, G. 2006, Stellar X-ray heating of planet atmospheres, Astronomy & Astrophysics, 458, L13, doi: 10.1051/0004-6361:20066093

Chambers, J. E. 2009, Planetary Migration: What Does It Mean for Planet Formation?, Annual Review of Earth and Planetary Sciences, 37, 321, doi: 10.1146/annurev.earth.031208.100122

Charnay, B., Forget, F., Wordsworth, R., et al. 2013, Exploring the faint young Sun problem and the possible climates of the Archean Earth with a 3-D GCM, Journal of Geophysical Research: Atmospheres, 118, 10,414, doi: 10.1002/jgrd.50808

Charnay, B., Le Hir, G., Fluteau, F., Forget, F., & Catling, D. C. 2017, A warm or a cold early Earth? New insights from a 3-D climate-carbon model, Earth and Planetary Science Letters, 474, 97, doi: 10.1016/j.epsl.2017.06.029

Chase, M. W. 1998, NIST-JANAF Thermochemical Tables, Fourth Edition, 4th edn. (J. Phys. Chem. Ref. Data)

Checlair, J. H., Abbot, D. S., Webber, R. J., et al. 2019, A Statistical Comparative Planetology Approach to Maximize the Scientific Return of Future Exoplanet Characterization Efforts, arXiv:1903.05211 [astro-ph]. http://arxiv.org/abs/1903.05211

Chen, H., & Rogers, L. A. 2016, Evolutionary Analysis of Gaseous Sub-Neptune-mass Planets with MESA, The Astrophysical Journal, 831, 180, doi: 10.3847/0004-637X/831/2/180

Chen, J., & Kipping, D. M. 2016, Probabilistic Forecasting of the Masses and Radii of Other Worlds, The Astrophysical Journal, 834, 17, doi: 10.3847/1538-4357/834/1/17

Chen, M., & Blankenship, R. E. 2011, Expanding the solar spectrum used by photosynthesis, Trends in Plant Science, 16, 427, doi: 10.1016/j.tplants.2011.03.011

Chen Jing M., Mo Gang, Pisek Jan, et al. 2012, Effects of foliage clumping on the estimation of global terrestrial gross primary productivity, Global Biogeochemical Cycles, 26, doi: 10.1029/2010GB003996

Claire, M. W., Catling, D. C., & Zahnle, K. J. 2006, Biogeochemical modelling of the rise in atmospheric oxygen, Geobiology, 4, 239, doi: 10.1111/j.1472-4669.2006.00084.x

Cnossen, I., Sanz-Forcada, J., Favata, F., et al. 2007, Habitat of early life: Solar X-ray and UV radiation at Earth's surface 4–3.5 billion years ago, Journal of Geophysical Research: Planets, 112, doi: 10.1029/2006JE002784

Cohen, I. B., Whitman, A., & Budenz, J. 1999, The Principia: Mathematical Principles of Natural Philosophy, 1st edn. (University of California Press). https://www.jstor.org/stable/10.1525/j.ctt9qh28z

Coogan, L. A., & Dosso, S. E. 2015, Alteration of ocean crust provides a strong temperature dependent feedback on the geological carbon cycle and is a primary driver of the Sr-isotopic composition of seawater, Earth and Planetary Science Letters, 415, 38, doi: 10.1016/j.epsl.2015.01.027

Cossou, C., Raymond, S. N., & Pierens, A. 2013, Making systems of Super Earths by inward migration of planetary embryos, Proceedings of the International Astronomical Union, 8, 360, doi: 10.1017/S1743921313008958

Cox, J. D., Wagman, D. D., & Medvedev, V. A. 1984, CODATA Key Values for Thermodynamics, 1st edn. (New York, NY: Hemisphere Publishing Corp.)

Crowe, S. A., Døssing, L. N., Beukes, N. J., et al. 2013, Atmospheric oxygenation three billion years ago, Nature, 501, 535, doi: 10.1038/nature12426

Cubillos, P., Erkaev, N. V., Juvan, I., et al. 2016, An overabundance of low-density Neptune-like planets, Monthly Notices of the Royal Astronomical Society, 1868. http://mnras.oxfordjournals.org/content/early/2016/12/10/mnras.stw3103.abstract

Cunningham, N. J., Spencer, J. R., Feldman, P. D., et al. 2015, Detection of Callisto's oxygen atmosphere with the Hubble Space Telescope, Icarus, 254, 178, doi: 10.1016/j.icarus.2015.03.021

Demory, B.-O., Gillon, M., De Wit, J., et al. 2016, A map of the large day–night temperature gradient of a super-Earth exoplanet, Nature, 532, 207. http://www.nature.com/nature/journal/v532/n7598/full/nature17169.html

Doyle, A. E., Young, E. D., Klein, B., Zuckerman, B., & Schlichting, H. E. 2019, Oxygen fugacities of extrasolar rocks: Evidence for an Earth-like geochemistry of exoplanets, Science, 366, 356, doi: 10.1126/science.aax3901

Dressing, C. D., & Charbonneau, D. 2015, The Occurrence of Potentially Habitable Planets Orbiting M Dwarfs Estimated from the Full Kepler Dataset and an Empirical Measurement of the Detection Sensitivity, The Astrophysical Journal, 807, 45, doi: 10.1088/0004-637X/807/1/45

Ercolano, B., Clarke, C. J., & Drake, J. J. 2009, X-Ray Irradiated Protoplanetary Disk Atmospheres. II. Predictions from Models in Hydrostatic Equilibrium, The Astrophysical Journal, 699, 1639, doi: 10.1088/0004-637X/699/2/1639

Erkaev, N. V., Lammer, H., Odert, P., et al. 2013, XUV-Exposed, Non-Hydrostatic Hydrogen-Rich Upper Atmospheres of Terrestrial Planets. Part I: Atmospheric Expansion and Thermal Escape, Astrobiology, 13, 1011, doi: 10.1089/ast.2012.0957

Falkowski, P. G., & Raven, J. A. 1997, Aquatic photosynthesis (Malden, Mass.: Blackwell Science)

Farquhar, J., Bao, H., & Thiemens, M. 2000, Atmospheric Influence of Earth's Earliest Sulfur Cycle, Science, 289, 756, doi: 10.1126/science.289.5480.756

Farquhar, J., Zerkle, A. L., & Bekker, A. 2011, Geological constraints on the origin of oxygenic photosynthesis, Photosynthesis Research, 107, 11, doi: 10.1007/s11120-010-9594-0

Farquhar, J., Zerkle, A. L., & Bekker, A. 2014, in Treatise on Geochemistry, 2nd edn. (Elsevier Ltd.), 91–138

Field, C. B., Behrenfeld, M. J., Randerson, J. T., & Falkowski, P. 1998, Primary production of the biosphere: integrating terrestrial and oceanic components, Science, 281, 237. http://science.sciencemag.org/content/281/5374/237.short

Forget, F., & Leconte, J. 2014, Possible climates on terrestrial exoplanets, Philosophical Transactions of the Royal Society A: Mathematical, Physical and Engineering Sciences, 372, 20130084, doi: 10.1098/rsta.2013.0084

Fralick, P., & Carter, J. E. 2011, Neoarchean deep marine paleotemperature: Evidence from turbidite successions, Precambrian Research, 191, 78, doi: 10.1016/j.precamres.2011.09.004

Frankenberg Christian, Fisher Joshua B., Worden John, et al. 2011, New global observations of the terrestrial carbon cycle from GOSAT: Patterns of plant fluorescence with gross primary productivity, Geophysical Research Letters, 38, doi: 10.1029/2011GL048738

Frei, R., Crowe, S. A., Bau, M., et al. 2016, Oxidative elemental cycling under the low O_2 Eoarchean atmosphere, Scientific Reports, 6, 21058, doi: 10.1038/srep21058

Fulton, B. J., Petigura, E. A., Howard, A. W., et al. 2017, The California-Kepler Survey. III. A Gap in the Radius Distribution of Small Planets, arXiv:1703.10375 [astro-ph]. http://arxiv.org/abs/1703.10375

Gale, J., & Wandel, A. 2017, The potential of planets orbiting red dwarf stars to support oxygenic photosynthesis and complex life, International Journal of Astrobiology, 16, 1. https://www.cambridge.

org/core/journals/international-journal-of-astrobiology/article/the-potential-of-planets-orbiting-red-dwarf-stars-to-support-oxygenic-photosynthesis-00C0C95A669962E6A4E7E5A722707D4C

Gaucher, E. A., Govindarajan, S., & Ganesh, O. K. 2008, Palaeotemperature trend for Precambrian life inferred from resurrected proteins, Nature, 451, 704, doi: 10.1038/nature06510

Genge, M. J., Davies, B., Suttle, M. D., van Ginneken, M., & Tomkins, A. G. 2017, The mineralogy and petrology of I-type cosmic spherules: Implications for their sources, origins and identification in sedimentary rocks, Geochimica et Cosmochimica Acta, 218, 167, doi: 10.1016/j.gca.2017.09.004

Genge Matthew J. 2016, The origins of I-type spherules and the atmospheric entry of iron micrometeoroids, Meteoritics & Planetary Science, 51, 1063, doi: 10.1111/maps.12645

Gillon, M., Triaud, A. H. M. J., Demory, B.-O., et al. 2017, Seven temperate terrestrial planets around the nearby ultracool dwarf star TRAPPIST-1, Nature, 542, 456, doi: 10.1038/nature21360

Ginzburg, S., & Sari, R. 2017, Tidal Heating of Young Super-Earth Atmospheres, Monthly Notices of the Royal Astronomical Society, 464, 3937, doi: 10.1093/mnras/stw2637

Glassgold, A. E., Najita, J., & Igea, J. 2004, Heating Protoplanetary Disk Atmospheres, The Astrophysical Journal, 615, 972, doi: 10.1086/424509

Goldblatt, C. 2015, Habitability of Waterworlds: Runaway Greenhouses, Atmospheric Expansion, and Multiple Climate States of Pure Water Atmospheres, Astrobiology, 15, 362, doi: 10.1089/ast.2014.1268

Goldblatt, C., Robinson, T. D., Zahnle, K. J., & Crisp, D. 2013, Low simulated radiation limit for runaway greenhouse climates, Nature Geoscience, 6, 661, doi: 10.1038/ngeo1892

Grewell, G. 2001, Colonizing the Universe: Science Fictions Then, Now, and in the (Imagined) Future, Rocky Mountain Review of Language and Literature, 55, 25, doi: 10.2307/1348255

HabEx. 2019, Habitable Exoplanet Observatory (HabEx) Final Report, Tech. rep., NASA. https://www.jpl.nasa.gov/habex/documents/

Haqq-Misra, J. D., Domagal-Goldman, S. D., Kasting, P. J., & Kasting, J. F. 2008, A Revised, Hazy Methane Greenhouse for the Archean Earth, Astrobiology, 8, 1127, doi: 10.1089/ast.2007.0197

Harman, C. E., Schwieterman, E. W., Schottelkotte, J. C., & Kasting, J. F. 2015, Abiotic O2 Levels on Planets around F, G, K, and M Stars: Possible False Positives for Life?, The Astrophysical Journal, 812, 137, doi: 10.1088/0004-637X/812/2/137

Hatzes, A. P. 2016, The Architecture of Exoplanets, Space Science Reviews, 205, 267, doi: 10.1007/s11214-016-0246-3

Hayashi, C., Nakazawa, K., & Mizuno, H. 1979, Earth's melting due to the blanketing effect of the primordial dense atmosphere, Earth and Planetary Science Letters, 43, 22. http://www.sciencedirect.com/science/article/pii/0012821X79901523

Heath, M. J., Doyle, L. R., Joshi, M. M., & Haberle, R. M. 1999, Habitability of Planets Around Red Dwarf Stars, Origins of life and evolution of the biosphere, 29, 405, doi: 10.1023/A:1006596718708

Hill, C., & Jones, R. L. 2000, Absorption of solar radiation by water vapor in clear and cloudy skies: Implications for anomalous absorption, Journal of Geophysical Research: Atmospheres, 105, 9421, doi: 10.1029/1999JD901153

Hill, R., & Rich, P. R. 1983, A Physical Interpretation for the Natural Photosynthetic Process, Proceedings of the National Academy of Sciences of the United States of America, 80, 978. http://www.jstor.org.offcampus.lib.washington.edu/stable/13866

Holland, H. D. 2002, Volcanic gases, black smokers, and the Great Oxidation Event, Geochimica et Cosmochimica Acta, 66, 3811

Howard, A. W. 2013, Observed Properties of Extrasolar Planets, Science, 340, 572, doi: 10.1126/science.1233545

Howe, A. R., & Burrows, A. 2015, Evolutionary Models of Super-Earths and Mini-Neptunes Incorporating Cooling and Mass Loss, The Astrophysical Journal, 808, 150, doi: 10.1088/0004-637X/808/2/150

Howett, C., Spencer, J., Pearl, J., & Segura, M. 2010, Thermal inertia and bolometric Bond albedo values for Mimas, Enceladus, Tethys, Dione, Rhea and Iapetus as derived from Cassini/CIRS measurements, Icarus, 206, 573, doi: 10.1016/j.icarus.2009.07.016

Hren, M. T., Tice, M. M., & Chamberlain, C. P. 2009, Oxygen and hydrogen isotope evidence for a temperate climate 3.42 billion years ago, Nature, 462, 205, doi: 10.1038/nature08518

Hunten, D. M. 1990, Kuiper prize lecture: Escape of atmospheres, ancient and modern, Icarus, 85, 1, doi: 10.1016/0019-1035(90)90100-N

Ikoma, M., & Hori, Y. 2012, In Situ Accretion of Hydrogen-rich Atmospheres on Short-period Super-Earths: Implications for the Kepler-11 Planets, The Astrophysical Journal, 753, 66, doi: 10.1088/0004-637X/753/1/66

Inamdar, N. K., & Schlichting, H. E. 2015, The formation of super-Earths and mini-Neptunes with giant impacts, Monthly Notices of the Royal Astronomical Society, 448, 1751, doi: 10.1093/mnras/stv030

Ingersoll, A. P. 1969, The Runaway Greenhouse: A History of Water on Venus, Journal of the Atmospheric Sciences, 26, 1191, doi: 10.1175/1520-0469(1969)026<1191:TRGAHO>2.0.CO;2

Isson, T. T., & Planavsky, N. J. 2018, Reverse weathering as a long-term stabilizer of marine pH and planetary climate, Nature, 560, 471, doi: 10.1038/s41586-018-0408-4

Jackson, A. P., Davis, T. A., & Wheatley, P. J. 2012, The coronal X-ray-age relation and its implications for the evaporation of exoplanets: X-ray-age relation and exoplanet evaporation, Monthly Notices of the Royal Astronomical Society, 422, 2024, doi: 10.1111/j.1365-2966.2012.20657.x

Jin, S., Mordasini, C., Parmentier, V., et al. 2014, Planetary Population Synthesis Coupled with Atmospheric Escape: A Statistical View of Evaporation, The Astrophysical Journal, 795, 65, doi: 10.1088/0004-637X/795/1/65

Johnstone, C. P., Güdel, M., Stökl, A., et al. 2015, The Evolution of Stellar Rotation and the Hydrogen Atmospheres of Habitable-zone Terrestrial Planets, The Astrophysical Journal Letters, 815, L12, doi: 10.1088/2041-8205/815/1/L12

Kadoya, S., Krissansen-Totton, J., & Catling, D. C. 2020, Probable Cold and Alkaline Surface Environment of the Hadean Earth Caused by Impact Ejecta Weathering, Geochemistry, Geophysics, Geosystems, 21, e2019GC008734, doi: 10.1029/2019GC008734

Kadoya, S., & Tajika, E. 2014, Conditions for oceans on earth-like planets orbiting within the habitable zone: importance of volcanic CO2 degassing, The Astrophysical Journal, 790, 107, doi: 10.1088/0004-637X/790/2/107

Kahn, R. 1985, The evolution of CO2 on Mars, Icarus, 62, 175, doi: 10.1016/0019-1035(85)90116-2

Kaltenegger, L., & Traub, W. A. 2009, Transits of Earth-like Planets, The Astrophysical Journal, 698, 519, doi: 10.1088/0004-637X/698/1/519

Kanzaki, Y., & Murakami, T. 2015, Estimates of atmospheric CO2 in the Neoarchean–Paleoproterozoic from paleosols, Geochimica et Cosmochimica Acta, 159, 190, doi: 10.1016/j.gca.2015.03.011

Kasting, J. F. 1993, Earth's early atmosphere, Science, 259, 920, doi: 10.1126/science.11536547

Kasting, J. F., Chen, H., & Kopparapu, R. K. 2015, Stratospheric Temperatures and Water Loss from Moist Greenhouse Atmospheres of Earth-like Planets, The Astrophysical Journal Letters, 813, L3, doi: 10.1088/2041-8205/813/1/L3

Kasting, J. F., & Toon, O. B. 1989, in Origin and evolution of planetary and satellite atmospheres (Tucson, AZ: University of Arizona Press), 423–449. http://inis.iaea.org/Search/search.aspx?orig_q=RN:21012339

Kasting, J. F., Whitmire, D. P., & Reynolds, R. T. 1993, Habitable Zones around Main Sequence Stars, Icarus, 101, 108, doi: 10.1006/icar.1993.1010

Kiang, N. Y., Siefert, J., Govindjee, & Blankenship, R. E. 2007a, Spectral Signatures of Photosynthesis. I. Review of Earth Organisms, Astrobiology, 7, 222, doi: 10.1089/ast.2006.0105

Kiang, N. Y., Segura, A., Tinetti, G., et al. 2007b, Spectral Signatures of Photosynthesis. II. Coevolution with Other Stars And The Atmosphere on Extrasolar Worlds, Astrobiology, 7, 252, doi: 10.1089/ast.2006.0108

Kite, E. S., & Ford, E. B. 2018, Habitability of Exoplanet Waterworlds, The Astrophysical Journal, 864, 75, doi: 10.3847/1538-4357/aad6e0

Knauth, L. P., & Lowe, D. R. 2003, High Archean climatic temperature inferred from oxygen isotope geochemistry of cherts in the 3.5 Ga Swaziland Supergroup, South Africa, GSA Bulletin, 115, 566, doi: 10.1130/0016-7606(2003)115<0566:HACTIF>2.0.CO;2

Koll, D. D. B., & Cronin, T. W. 2018, Earth's outgoing longwave radiation linear due to H_2O greenhouse effect, Proceedings of the National Academy of Sciences, 115, 10293, doi: 10.1073/pnas.1809868115

Kopparapu, R. K., Ramirez, R., Kasting, J. F., et al. 2013, Habitable Zones around Main-sequence Stars: New Estimates, The Astrophysical Journal, 765, 131, doi: 10.1088/0004-637X/765/2/131

Koskinen, T. T., Harris, M. J., Yelle, R. V., & Lavvas, P. 2013, The escape of heavy atoms from the ionosphere of HD209458b. I. A photochemical–dynamical model of the thermosphere, Icarus, 226, 1678, doi: 10.1016/j.icarus.2012.09.027

Koskinen, T. T., Lavvas, P., Harris, M. J., & Yelle, R. V. 2014, Thermal escape from extrasolar giant planets, Phil. Trans. R. Soc. A, 372, 20130089, doi: 10.1098/rsta.2013.0089

Kramers, J. D., & Tolstikhin, I. N. 2006, Terrestrial Xe isotope systematics and the missing Xe problem can be resolved in a model of Giant Impact-related atmosphere loss, Geochimica et Cosmochimica Acta, 70, A336, doi: 10.1016/j.gca.2006.06.678

Krissansen-Totton, J., Arney, G. N., & Catling, D. C. 2018a, Constraining the climate and ocean pH of the early Earth with a geological carbon cycle model, Proceedings of the National Academy of Sciences, 2017, doi: 10.1073/pnas.1721296115

Krissansen-Totton, J., & Catling, D. C. 2017, Constraining climate sensitivity and continental versus seafloor weathering using an inverse geological carbon cycle model, Nature Communications, 8, 15423, doi: 10.1038/ncomms15423

Krissansen-Totton, J., & Catling, D. C. 2020, A coupled carbon-silicon cycle model over Earth history: Reverse weathering as a possible explanation of a warm mid-Proterozoic climate, Earth and Planetary Science Letters, 537, 116181, doi: 10.1016/j.epsl.2020.116181

Krissansen-Totton, J., Olson, S., & Catling, D. C. 2018b, Disequilibrium biosignatures over Earth history and implications for detecting exoplanet life, Science Advances, 4, eaao5747, doi: 10.1126/sciadv.aao5747

Krull-Davatzes, A. E., Byerly, G. R., & Lowe, D. R. 2010, Evidence for a low-O2 Archean atmosphere from nickel-rich chrome spinels in 3.24Ga impact spherules, Barberton greenstone belt, South Africa, Earth and Planetary Science Letters, 296, 319, doi: 10.1016/j.epsl.2010.05.014

Kuramoto, K., Umemoto, T., & Ishiwatari, M. 2013, Effective hydrodynamic hydrogen escape from an early Earth atmosphere inferred from high-accuracy numerical simulation, Earth and Planetary Science Letters, 375, 312, doi: 10.1016/j.epsl.2013.05.050

Lammer, H., Erkaev, N. V., Odert, P., et al. 2013, Probing the blow-off criteria of hydrogen-rich 'super-Earths', Monthly Notices of the Royal Astronomical Society, 430, 1247, doi: 10.1093/mnras/sts705

Lammer, H., Kislyakova, K. G., Odert, P., et al. 2011, Pathways to Earth-Like Atmospheres: Extreme Ultraviolet (EUV)-Powered Escape of Hydrogen-Rich Protoatmospheres, Origins of Life and Evolution of Biospheres, 41, 503, doi: 10.1007/s11084-012-9264-7

Lammer, H., Güdel, M., Kulikov, Y., et al. 2012, Variability of solar/stellar activity and magnetic field and its influence on planetary atmosphere evolution, Earth, Planets and Space, 64, 179, doi: 10.5047/eps.2011.04.002

Lammer, H., Stökl, A., Erkaev, N. V., et al. 2014, Origin and loss of nebula-captured hydrogen envelopes from 'sub'- to 'super-Earths' in the habitable zone of Sun-like stars, Monthly Notices of the Royal Astronomical Society, 439, 3225, doi: 10.1093/mnras/stu085

Leconte, J., Forget, F., Charnay, B., Wordsworth, R., & Pottier, A. 2013, Increased insolation threshold for runaway greenhouse processes on Earth-like planets, Nature, 504, 268. http://search.proquest.com/docview/1470094063/abstract

Lehmer, O. R., & Catling, D. C. 2017, Rocky Worlds Limited to ∼1.8 Earth Radii by Atmospheric Escape during a Star's Extreme UV Saturation, The Astrophysical Journal, 845, 130, doi: 10.3847/1538-4357/aa8137

Lehmer, O. R., Catling, D. C., Buick, R., Brownlee, D. E., & Newport, S. 2020, Atmospheric CO2 levels from 2.7 billion years ago inferred from micrometeorite oxidation, Science Advances, 6, eaay4644, doi: 10.1126/sciadv.aay4644

Lehmer, O. R., Catling, D. C., Parenteau, M. N., & Hoehler, T. M. 2018, The Productivity of Oxygenic Photosynthesis around Cool, M Dwarf Stars, The Astrophysical Journal, 859, 171, doi: 10.3847/1538-4357/aac104

Lehmer, O. R., Catling, D. C., & Zahnle, K. J. 2017, The Longevity of Water Ice on Ganymedes and Europas around Migrated Giant Planets, The Astrophysical Journal, 839, 32, doi: 10.3847/1538-4357/aa67ea

Leighton, R. B., & Murray, B. C. 1966, Behavior of Carbon Dioxide and Other Volatiles on Mars, Science, 153, 136. http://www.jstor.org/stable/1719588

Linsky, J. L., Yang, H., France, K., et al. 2010, Observations of Mass Loss from the Transiting Exoplanet HD 209458b, The Astrophysical Journal, 717, 1291, doi: 10.1088/0004-637X/717/2/1291

Lissauer, J. J., Jontof-Hutter, D., Rowe, J. F., et al. 2013, All Six Planets Known to Orbit Kepler-11 Have Low Densities, The Astrophysical Journal, 770, 131, doi: 10.1088/0004-637X/770/2/131

Lopez, E. D., & Fortney, J. J. 2013, THE ROLE OF CORE MASS IN CONTROLLING EVAPORATION: THE KEPLER RADIUS DISTRIBUTION AND THE KEPLER-36 DENSITY DICHOTOMY, The Astrophysical Journal, 776, 2, doi: 10.1088/0004-637X/776/1/2

Lopez, E. D., & Fortney, J. J. 2014, Understanding the Mass-Radius Relation for Subneptunes: Radius as a Proxy for Composition, The Astrophysical Journal, 792, 1, doi: 10.1088/0004-637X/792/1/1

Lopez, E. D., Fortney, J. J., & Miller, N. 2012, HOW THERMAL EVOLUTION AND MASS-LOSS SCULPT POPULATIONS OF SUPER-EARTHS AND SUB-NEPTUNES: APPLICATION TO THE KEPLER-11 SYSTEM AND BEYOND, The Astrophysical Journal, 761, 59, doi: 10.1088/0004-637X/761/1/59

Lopez, E. D., & Rice, K. 2016, Predictions for the Period Dependence of the Transition Between Rocky Super-Earths and Gaseous Sub-Neptunes and Implications for $$\backslash$ eta_ ${$$\backslash$ mathrm ${$$\backslash$ oplus$}$$}$ $, arXiv preprint arXiv:1610.09390. https://arxiv.org/abs/1610.09390

Love, S. G., & Brownlee, D. E. 1991, Heating and thermal transformation of micrometeoroids entering the Earth's atmosphere, Icarus, 89, 26

Luger, R., & Barnes, R. 2015, Extreme water loss and abiotic O2 buildup on planets throughout the habitable zones of M dwarfs, Astrobiology, 15, 119. http://online.liebertpub.com/doi/abs/10.1089/ast.2014.1231

Luger, R., Barnes, R., Lopez, E., et al. 2015, Habitable Evaporated Cores: Transforming Mini-Neptunes into Super-Earths in the Habitable Zones of M Dwarfs, Astrobiology, 15, 57, doi: 10.1089/ast.2014.1215

Lunine, J. I. 1993, The atmospheres of Uranus and Neptune, Annual review of astronomy and astrophysics, 31, 217. http://www.annualreviews.org/doi/pdf/10.1146/annurev.aa.31.090193.001245

LUVOIR. 2019, Large UV/Optical/IR Surveyor (LUVOIR) Final Report, Tech. rep., NASA. https://asd.gsfc.nasa.gov/luvoir/reports/

Lyons, T. W., Reinhard, C. T., & Planavsky, N. J. 2014, The rise of oxygen in Earth's early ocean and atmosphere, Nature, 506, 307, doi: 10.1038/nature13068

Maher, K., & Chamberlain, C. P. 2014, Hydrologic Regulation of Chemical Weathering and the Geologic Carbon Cycle, Science, 343, 1502, doi: 10.1126/science.1250770

Manabe, S., & Wetherald, R. T. 1967, Thermal Equilibrium of the Atmosphere with a Given Distribution of Relative Humidity, Journal of the Atmospheric Sciences, 24, 241, doi: 10.1175/1520-0469(1967)024<0241:TEOTAW>2.0.CO;2

Mann, A. W., Feiden, G. A., Gaidos, E., Boyajian, T., & Braun, K. v. 2015, How to Constrain Your M Dwarf: Measuring Effective Temperature, Bolometric Luminosity, Mass, and Radius, The Astrophysical Journal, 804, 64, doi: 10.1088/0004-637X/804/1/64

Marcy, G. W., Isaacson, H., Howard, A. W., et al. 2014, Masses, Radii, and Orbits of Small Kepler Planets: The Transition from Gaseous to Rocky Planets, The Astrophysical Journal Supplement Series, 210, 20, doi: 10.1088/0067-0049/210/2/20

Marosvölgyi, M. A., & van Gorkom, H. J. 2010, Cost and color of photosynthesis, Photosynthesis Research, 103, 105, doi: 10.1007/s11120-009-9522-3

Massie, S. T., & Hunten, D. M. 1981, Stratospheric eddy diffusion coefficients from tracer data, Journal of Geophysical Research: Oceans, 86, 9859, doi: 10.1029/JC086iC10p09859

Massol, H., Hamano, K., Tian, F., et al. 2016, Formation and Evolution of Protoatmospheres, Space Science Reviews, 205, 153, doi: 10.1007/s11214-016-0280-1

Masuda, K. 2014, Very Low Density Planets around Kepler-51 Revealed with Transit Timing Variations and an Anomaly Similar to a Planet-Planet Eclipse Event, The Astrophysical Journal, 783, 53, doi: 10.1088/0004-637X/783/1/53

Mauzerall, D., Neuberger, A., & Kenner, G. W. 1976, Chlorophyll and photosynthesis, Philosophical Transactions of the Royal Society of London. B, Biological Sciences, 273, 287, doi: 10.1098/rstb.1976.0014

McCree, K. J. 1971, The action spectrum, absorptance and quantum yield of photosynthesis in crop plants, Agricultural Meteorology, 9, 191

McCree, K. J. 1973, The measurement of photosynthetically active radiation, Solar Energy, 15, 83, doi: 10.1016/0038-092X(73)90010-8

McKay, C. P. 2014, Requirements and limits for life in the context of exoplanets, Proceedings of the National Academy of Sciences, 111, 12628, doi: 10.1073/pnas.1304212111

Meadows, V. S., Reinhard, C. T., Arney, G. N., et al. 2018a, Exoplanet Biosignatures: Understanding Oxygen as a Biosignature in the Context of Its Environment, Astrobiology, doi: 10.1089/ast.2017.1727

Meadows, V. S., Arney, G. N., Schwieterman, E. W., et al. 2018b, The Habitability of Proxima Centauri b: Environmental States and Observational Discriminants, Astrobiology, 18, 133, doi: 10.1089/ast.2016.1589

Mielke, S. P., Kiang, N. Y., Blankenship, R. E., & Mauzerall, D. 2013, Photosystem trap energies and spectrally-dependent energy-storage efficiencies in the Chl d-utilizing cyanobacterium, Acaryochloris marina, Biochimica et Biophysica Acta (BBA) - Bioenergetics, 1827, 255, doi: 10.1016/j.bbabio.2012.11.002

Mills, B., Daines, S. J., & Lenton, T. M. 2014, Changing tectonic controls on the long-term carbon cycle from Mesozoic to present, Geochemistry, Geophysics, Geosystems, 15, 4866, doi: 10.1002/2014GC005530

Milo, R. 2009, What governs the reaction center excitation wavelength of photosystems I and II?, Photosynthesis Research, 101, 59, doi: 10.1007/s11120-009-9465-8

Mordasini, C., Alibert, Y., Georgy, C., et al. 2012, Characterization of exoplanets from their formation - II. The planetary mass-radius relationship, Astronomy & Astrophysics, 547, A112, doi: 10.1051/0004-6361/201118464

Murray-Clay, R. A., Chiang, E. I., & Murray, N. 2009, Atmospheric Escape From Hot Jupiters, The Astrophysical Journal, 693, 23, doi: 10.1088/0004-637X/693/1/23

Myhre, G., Highwood, E. J., Shine, K. P., & Stordal, F. 1998, New estimates of radiative forcing due to well mixed greenhouse gases, Geophysical Research Letters, 25, 2715, doi: 10.1029/98GL01908

O'Malley-James, J. T., & Kaltenegger, L. 2018, The Vegetation Red Edge Biosignature Through Time on Earth and Exoplanets, Astrobiology, 18, 1123, doi: 10.1089/ast.2017.1798

Owen, J. E., & Jackson, A. P. 2012, Planetary evaporation by UV and X-ray radiation: basic hydrodynamics, Monthly Notices of the Royal Astronomical Society, 425, 2931, doi: 10.1111/j.1365-2966.2012.21481.x

Owen, J. E., & Morton, T. D. 2016, THE INITIAL PHYSICAL CONDITIONS OF KEPLER-36 b AND c, The Astrophysical Journal, 819, L10, doi: 10.3847/2041-8205/819/1/L10

Owen, J. E., & Wu, Y. 2013, Kepler Planets: A Tale of Evaporation, The Astrophysical Journal, 775, 105, doi: 10.1088/0004-637X/775/2/105

Owen, J. E., & Wu, Y. 2016, Atmospheres of Low-mass Planets: The "Boil-off", The Astrophysical Journal, 817, 107, doi: 10.3847/0004-637X/817/2/107

Papageorgiou, G. C. 2004, in Chlorophyll a Fluorescence: A Signature of Photosynthesis, ed. G. C. Papageorgiou & Govindjee, Advances in Photosynthesis and Respiration (Dordrecht: Springer Netherlands), 43–63, doi: 10.1007/978-1-4020-3218-9_2

Pavlov, A., & Kasting, J. 2002, Mass-Independent Fractionation of Sulfur Isotopes in Archean Sediments: Strong Evidence for an Anoxic Archean Atmosphere, Astrobiology, 2, 27, doi: 10.1089/153110702753621321

Pepin, R. O. 1997, Evolution of Earth's Noble Gases: Consequences of Assuming Hydrodynamic Loss Driven by Giant Impact, Icarus, 126, 148, doi: 10.1006/icar.1996.5639

Perez-Becker, D., & Chiang, E. 2013, Catastrophic evaporation of rocky planets, Monthly Notices of the Royal Astronomical Society, 433, 2294, doi: 10.1093/mnras/stt895

Pettai, H., Oja, V., Freiberg, A., & Laisk, A. 2005, The long-wavelength limit of plant photosynthesis, FEBS Letters, 579, 4017, doi: 10.1016/j.febslet.2005.04.088

Pierrehumbert, R. T. 2010, Principles of Planetary Climate, 3rd edn. (Cambridge, UK: Cambridge University Press)

Pizzolato, N., Maggio, A., Micela, G., Sciortino, S., & Ventura, P. 2003, The stellar activity-rotation relationship revisited: Dependence of saturated and non-saturated X-ray emission regimes on stellar mass for late-type dwarfs, Astronomy & Astrophysics, 397, 147, doi: 10.1051/0004-6361:20021560

Planavsky, N. J., Asael, D., Hofmann, A., et al. 2014, Evidence for oxygenic photosynthesis half a billion years before the Great Oxidation Event, Nature Geoscience, 7, 283, doi: 10.1038/ngeo2122

Prokopenko Maria G., Pauluis Olivier M., Granger Julie, & Yeung Laurence Y. 2011, Exact evaluation of gross photosynthetic production from the oxygen triple-isotope composition of O2: Implications for the net-to-gross primary production ratios, Geophysical Research Letters, 38, doi: 10.1029/2011GL047652

Ramirez, R. M., & Kaltenegger, L. 2016, Habitable Zones of Post-Main Sequence Stars, The Astrophysical Journal, 823, 6, doi: 10.3847/0004-637X/823/1/6

Raven, J. A., Kübler, J. E., & Beardall, J. 2000, Put out the light, and then put out the light, Journal of the Marine Biological Association of the United Kingdom, 80, 1. https://www.cambridge.org/core/journals/journal-of-the-marine-biological-association-of-the-united-kingdom/article/put-out-the-light-and-then-put-out-the-light/09EC3FBA96958AA2FCCAC2E8405AC375

Raymond, S. N., & Cossou, C. 2014, No universal minimum-mass extrasolar nebula: evidence against in situ accretion of systems of hot super-Earths, Monthly Notices of the Royal Astronomical Society: Letters, 440, L11, doi: 10.1093/mnrasl/slu011

Reinhard, C. T., Planavsky, N. J., Gill, B. C., et al. 2016, Evolution of the global phosphorus cycle, Nature, 541, 386, doi: 10.1038/nature20772

Ribas, I., Guinan, E. F., Güdel, M., & Audard, M. 2005, Evolution of the Solar Activity over Time and Effects on Planetary Atmospheres. I. High-Energy Irradiances (1-1700 Å), The Astrophysical Journal, 622, 680, doi: 10.1086/427977

Rimmer, P., Shorttle, O., & Rugheimer, S. 2019, Oxidised micrometeorites as evidence for low atmospheric pressure on the early Earth, Geochemical Perspectives Letters, 38, doi: 10.7185/geochemlet.1903

Ritchie, R. J. 2010, Modelling photosynthetic photon flux density and maximum potential gross photosynthesis, Photosynthetica, 48, 596, doi: 10.1007/s11099-010-0077-5

Ritchie, R. J., Larkum, A. W., & Ribas, I. 2017, Could photosynthesis function on Proxima Centauri b?, International Journal of Astrobiology, 17, 147, doi: 10.1017/S1473550417000167

Robinson, T. D., & Catling, D. C. 2012, AN ANALYTIC RADIATIVE-CONVECTIVE MODEL FOR PLANETARY ATMOSPHERES, The Astrophysical Journal, 757, 104, doi: 10.1088/0004-637X/757/1/104

Rogers, L. A. 2015, Most 1.6 Earth-radius Planets are Not Rocky, The Astrophysical Journal, 801, 41, doi: 10.1088/0004-637X/801/1/41

Rosing, M. T., & Frei, R. 2004, U-rich Archaean sea-floor sediments from Greenland – indications of >3700 Ma oxygenic photosynthesis, Earth and Planetary Science Letters, 217, 237, doi: 10.1016/S0012-821X(03)00609-5

Ross, R. T., & Calvin, M. 1967, Thermodynamics of Light Emission and Free-Energy Storage in Photosynthesis, Biophysical Journal, 7, 595, doi: 10.1016/S0006-3495(67)86609-8

Rushby, A. J., Claire, M. W., Osborn, H., & Watson, A. J. 2013, Habitable Zone Lifetimes of Exoplanets around Main Sequence Stars, Astrobiology, 13, 833, doi: 10.1089/ast.2012.0938

Ruttenberg, K. 2014, in Treatise on Geochemistry (Elsevier), 499–558, doi: 10.1016/B978-0-08-095975-7.00813-5

Sagan, C., & Mullen, G. 1972, Earth and Mars: Evolution of Atmospheres and Surface Temperatures, Science, 177, 52, doi: 10.1126/science.177.4043.52

Sagan, C., Thompson, W. R., Carlson, R., Gurnett, D., & Hord, C. 1993, A search for life on Earth from the Galileo spacecraft, Nature, 365, 715, doi: 10.1038/365715a0

Sanchez-Lavega, A. 2011, An Introduction to Planetary Atmospheres (CRC Press)

Satkoski, A. M., Beukes, N. J., Li, W., Beard, B. L., & Johnson, C. M. 2015, A redox-stratified ocean 3.2 billion years ago, Earth and Planetary Science Letters, 430, 43, doi: 10.1016/j.epsl.2015.08.007

Schubert, G., Anderson, J. D., Spohn, T., & McKinnon, W. 2004, in Jupiter: The Planet, Satellites and Magnetosphere, ed. F. Bagenal, T. Dowling, & W. McKinnon (Cambridge, UK: Cambridge University Press), 281–301

Schwieterman, E. W., Kiang, N. Y., Parenteau, M. N., et al. 2018, Exoplanet Biosignatures: A Review of Remotely Detectable Signs of Life, Astrobiology, 18, 663, doi: 10.1089/ast.2017.1729

Seager, S. 2013, Exoplanet Habitability, Science, 340, 577, doi: 10.1126/science.1232226

Seager, S., Turner, E., Schafer, J., & Ford, E. 2005, Vegetation's Red Edge: A Possible Spectroscopic Biosignature of Extraterrestrial Plants, Astrobiology, 5, 372, doi: 10.1089/ast.2005.5.372

Selsis, F., Kasting, J. F., Levrard, B., et al. 2007, Habitable planets around the star Gliese 581?, Astronomy & Astrophysics, 476, 1373, doi: 10.1051/0004-6361:20078091

Shields, A. L., Ballard, S., & Johnson, J. A. 2016, The habitability of planets orbiting M-dwarf stars, Physics Reports, 663, 1, doi: 10.1016/j.physrep.2016.10.003

Shields, A. L., Meadows, V. S., Bitz, C. M., et al. 2013, The Effect of Host Star Spectral Energy Distribution and Ice-Albedo Feedback on the Climate of Extrasolar Planets, Astrobiology, 13, 715, doi: 10.1089/ast.2012.0961

Sleep, N. H., & Zahnle, K. 2001, Carbon dioxide cycling and implications for climate on ancient Earth, Journal of Geophysical Research: Planets, 106, 1373, doi: 10.1029/2000JE001247

Slipski, M., Jakosky, B. M., Benna, M., et al. 2018, Variability of Martian Turbopause Altitudes, Journal of Geophysical Research: Planets, 123, 2939, doi: 10.1029/2018JE005704

Smirnov, V. N. 2008, Rate constant of the gas-phase reaction between Fe atoms and CO2, Kinetics and Catalysis, 49, 607, doi: 10.1134/S0023158408050017

Smith, M. L., Claire, M. W., Catling, D. C., & Zahnle, K. J. 2014, The formation of sulfate, nitrate and perchlorate salts in the martian atmosphere, Icarus, 231, 51, doi: 10.1016/j.icarus.2013.11.031

Som, S. M., Buick, R., Hagadorn, J. W., et al. 2016, Earth's air pressure 2.7 billion years ago constrained to less than half of modern levels, Nature Geoscience, 9, 448, doi: 10.1038/ngeo2713

Som, S. M., Catling, D. C., Harnmeijer, J. P., Polivka, P. M., & Buick, R. 2012, Air density 2.7 billion years ago limited to less than twice modern levels by fossil raindrop imprints, Nature, 484, 359, doi: 10.1038/nature10890

Stevenson, D. J. 1999, Life-sustaining planets in interstellar space?, Nature, 400, 32, doi: 10.1038/21811

Stolen, S., Glöckner, R., Gronvold, F., Atake, T., & Izumisawa, S. 2015, Heat capacity and thermodynamic properties of nearly stoichiometric wüstite from 13 to 450 K, American Mineralogist, 81, 973, doi: 10.2138/am-1996-7-819

Stomp, M., Huisman, J., Stal, L. J., & Matthijs, H. C. P. 2007, Colorful niches of phototrophic microorganisms shaped by vibrations of the water molecule, The ISME Journal; London, 1, 271, doi: http://dx.doi.org/10.1038/ismej.2007.59

Stüeken, E., Kipp, M., Koehler, M., et al. 2016, Modeling pN2 through Geological Time: Implications for Planetary Climates and Atmospheric Biosignatures, Astrobiology, 16, 949, doi: 10.1089/ast.2016.1537

Stüeken, E. E., Catling, D. C., & Buick, R. 2012, Contributions to late Archaean sulphur cycling by life on land, Nature Geoscience, 5, 722, doi: 10.1038/ngeo1585

Takizawa, K., Minagawa, J., Tamura, M., Kusakabe, N., & Narita, N. 2017, Red-edge position of habitable exoplanets around M-dwarfs, Scientific Reports, 7, doi: 10.1038/s41598-017-07948-5

Tian, F. 2009, THERMAL ESCAPE FROM SUPER EARTH ATMOSPHERES IN THE HABITABLE ZONES OF M STARS, The Astrophysical Journal, 703, 905, doi: 10.1088/0004-637X/703/1/905

Tianrui, S., Zhengjun, H., Yusheng, W., & Yanxue, L. 2007, A Study of Mesoproterozoic Iron Cosmic Micro-spherules from 1.8 Ga and 1.6 Ga Old Strata in the Ming Tombs District, Beijing, Acta Geologica Sinica - English Edition, 81, 649, doi: 10.1111/j.1755-6724.2007.tb00988.x

Tinetti, G., Rashby, S., & Yung, Y. L. 2006, Detectability of Red-Edge-shifted Vegetation on Terrestrial Planets Orbiting M Stars, The Astrophysical Journal, 644, L129, doi: 10.1086/505746

Tolstikhin, I. N., & O'Nions, R. K. 1994, The Earth's missing xenon: A combination of early degassing and of rare gas loss from the atmosphere, Chemical Geology, 115, 1, doi: 10.1016/0009-2541(94)90142-2

Tomkins, A. G., Bowlt, L., Genge, M., et al. 2016, Ancient micrometeorites suggestive of an oxygen-rich Archaean upper atmosphere, Nature, 533, 235, doi: 10.1038/nature17678

Tsiganis, K., Gomes, R., Morbidelli, A., & Levison, H. F. 2005, Origin of the orbital architecture of the giant planets of the Solar System, Nature, 435, 459, doi: 10.1038/nature03539

Turbet, M. 2019, Two examples of how to use observations of terrestrial planets orbiting in temperate orbits around low mass stars to test key concepts of planetary habitability, Proceedings of the Annual meeting of the French Society of Astronomy and Astrophysics, SF2A-2019, pp. 341

Tyrrell, T. 1999, The relative influences of nitrogen and phosphorus on oceanic primary production, Nature, 400, 525, doi: 10.1038/22941

van Grondelle, R., & Boeker, E. 2017, Limits on Natural Photosynthesis, The Journal of Physical Chemistry B, doi: 10.1021/acs.jpcb.7b03024

Vidal-Madjar, A., Désert, J.-M., Etangs, A. L. d., et al. 2004, Detection of Oxygen and Carbon in the Hydrodynamically Escaping Atmosphere of the Extrasolar Planet HD 209458b, The Astrophysical Journal Letters, 604, L69, doi: 10.1086/383347 von Paris, P., Selsis, F., Kitzmann, D., & Rauer, H. 2013, The Dependence of the Ice-Albedo Feedback on Atmospheric Properties, Astrobiology, 13, 899, doi: 10.1089/ast.2013.0993

Walker, J. C. G. 1993, in Biogeochemistry of Global Change: Radiatively Active Trace Gases Selected Papers from the Tenth International Symposium on Environmental Biogeochemistry, San Francisco, August 19–24, 1991, ed. R. S. Oremland (Boston, MA: Springer US), 3–28, doi: 10.1007/978-1-4615-2812-8_1

Walker, J. C. G., Hays, P. B., & Kasting, J. F. 1981, A negative feedback mechanism for the long-term stabilization of Earth's surface temperature, Journal of Geophysical Research: Oceans, 86, 9776, doi: 10.1029/JC086iC10p09776

Wang, J., Davis, A. M., Clayton, R. N., & Mayeda, T. K. 1994, in 25th Lunar and Planetary Science Conference, Houston, TX, 1459–1460

Watson, A. J., Donahue, T. M., & Walker, J. C. G. 1981, The dynamics of a rapidly escaping atmosphere: Applications to the evolution of Earth and Venus, Icarus, 48, 150, doi: 10.1016/0019-1035(81)90101-9

Weiss, L. M., & Marcy, G. W. 2014, The Mass-Radius Relation for 65 Exoplanets Smaller than 4 Earth Radii, The Astrophysical Journal Letters, 783, L6, doi: 10.1088/2041-8205/783/1/L6

Wexler, A. 1977, Vapor pressure formulation for ice, Journal of Research of the National Bureau of Standards. http://archive.org/details/jresv81An1p5

Whewell, W. 1853, Of the Plurality of Worlds: An Essay (London : J.W. Parker and Son)

Winnick, M. J., & Maher, K. 2018, Relationships between CO2, thermodynamic limits on silicate weathering, and the strength of the silicate weathering feedback, Earth and Planetary Science Letters, 485, 111, doi: 10.1016/j.epsl.2018.01.005

Wit, M. J. d., & Furnes, H. 2016, 3.5-Ga hydrothermal fields and diamictites in the Barberton Greenstone Belt—Paleoarchean crust in cold environments, Science Advances, 2, e1500368, doi: 10.1126/sciadv.1500368

Wolf, E. T., Shields, A. L., Kopparapu, R. K., Haqq-Misra, J., & Toon, O. B. 2017, Constraints on Climate and Habitability for Earth-like Exoplanets Determined from a General Circulation Model, The Astrophysical Journal, 837, 107, doi: 10.3847/1538-4357/aa5ffc

Wolfgang, A., & Lopez, E. 2015, HOW ROCKY ARE THEY? THE COMPOSITION DISTRIBUTION OF KEPLER'S SUB-NEPTUNE PLANET CANDIDATES WITHIN 0.15 AU, The Astrophysical Journal, 806, 183, doi: 10.1088/0004-637X/806/2/183

Wolstencroft, R., & Raven, J. 2002, Photosynthesis: Likelihood of Occurrence and Possibility of Detection on Earth-like Planets, Icarus, 157, 535, doi: 10.1006/icar.2002.6854

Wordsworth, R., Kalugina, Y., Lokshtanov, S., et al. 2017, Transient reducing greenhouse warming on early Mars, Geophysical Research Letters, 44, 665, doi: 10.1002/2016GL071766

Yang, J., Boué, G., Fabrycky, D. C., & Abbot, D. S. 2014, Strong Dependence of the Inner Edge of the Habitable Zone on Planetary Rotation Rate, The Astrophysical Journal Letters, 787, L2, doi: 10.1088/2041-8205/787/1/L2

Yoshioka, K., Yoshikawa, I., Tsuchiya, F., Kagitani, M., & Murakami, G. 2011, Hot electron component in the Io plasma torus confirmed through EUV spectral analysis, Journal of Geophysical Research: Space Physics, 116, A09204, doi: 10.1029/2011JA016583

Zahnle, K., & Buick, R. 2016, Atmospheric science: Ancient air caught by shooting stars, Nature, 533, 184, doi: 10.1038/533184a

Zahnle, K., Claire, M., & Catling, D. 2006, The loss of mass-independent fractionation in sulfur due to a Palaeoproterozoic collapse of atmospheric methane, Geobiology, 4, 271, doi: 10.1111/j.1472-4669.2006.00085.x

Zahnle, K. J., & Catling, D. C. 2017, The cosmic shoreline: the evidence that escape determines which planets have atmospheres, and what this may mean for Proxima Centauri b, arXiv:1702.03386 [astro-ph]. `http://arxiv.org/abs/1702.03386`

Zahnle, K. J., Gacesa, M., & Catling, D. C. 2019, Strange messenger: A new history of hydrogen on Earth, as told by Xenon, Geochimica et Cosmochimica Acta, 244, 56, doi: `10.1016/j.gca.2018.09.017`

Zeng, L., Sasselov, D. D., & Jacobsen, S. B. 2016, Mass–Radius Relation for Rocky Planets Based on PREM, The Astrophysical Journal, 819, 127, doi: `10.3847/0004-637X/819/2/127`

Zeng, L., Jacobsen, S. B., Hyung, E., et al. 2017, in Terrestrial Planet Differentiation: Everywhere Every Way, 1576, The Woodlands, Texas

Zsom, A., Seager, S., Wit, J. d., & Stamenković, V. 2013, Toward the Minimum Inner Edge Distance of The Habitable Zone, The Astrophysical Journal, 778, 109, doi: `10.1088/0004-637X/778/2/109`

VITA

Owen R. Lehmer
Dept. Earth and Space Sciences & Astrobiology Program
University of Washington, Seattle, WA
olehmer@uw.edu

Education

- **University of Washington, Seattle, WA**. PhD candidate, Department of Earth and Space Sciences & Astrobiology Program. 2015 - present.
- **Goucher College, Baltimore, MD**. BA, mathematics and computer science. 2009 - 2013.

Peer reviewed publications

- **Lehmer, O. R.**, Catling, D. C., Zahnle, K. J. (2017). The Longevity of Water Ice on Ganymedes and Europas around Migrated Giant Planets. *The Astrophysical Journal*, DOI: `10.3847/1538-4357/aa67ea`.
- **Lehmer, O. R.** and Catling, D. C. (2017). Rocky Worlds Limited to ∼1.8 Earth Radii by Atmospheric Escape during a Star's Extreme UV Saturation. *The Astrophysical Journal*, DOI: `10.3847/1538-4357/aa8137`.
- **Lehmer, O. R.**, Catling, D. C., Parenteau, M. N., Hoehler, T. M. (2018). The Productivity of Oxygenic Photosynthesis around Cool, M Dwarf Stars. *The Astrophysical Journal*, DOI: `10.3847/1538-4357/aac104`.
- **Lehmer, O. R.**, Catling, D. C., Buick, R., Brownlee, D. E., Newport, S. (2020). Atmospheric CO_2 levels from 2.7 billion years ago inferred from micrometeorite oxidation. *Science Advances*, DOI: `10.1126/sciadv.aay4644`.

White papers

- Krissansen-Totton, J., Arney, G. N., Catling, D. C., Felton, R., Fortney, J., Garland, R., Irwin, P., Kopparapu, R., **Lehmer, O. R.**, Lustig-Yaeger, J., Meadows, V., Molaverdikhani, K., Olson, S., Schwieterman, E. W., Taylor J. (2019). Atmospheric disequilibrium as an exoplanet biosignature: Opportunities for next generation telescopes. *2020 Decadal Survey, National Academies of Sciences Astronomy and Astrophysics.*

- Arney, G. N., Batalha, N., Britt, A. V., Cowan, N., Domagal-Goldman, S. D., Dressing, C., France, K., Fujii, Y., Kopparapu, R., Kane, S., Krissansen-Totton, J., Lincowski, A., **Lehmer, O. R.**, Lopez, E., Lustig-Yaeger, J., Meadows, V. S., Olson, S., Paranteau, M. N., Pascucci, I., Ramirez, R., Reinhard, C., Roberge, A., Robinson, T. D., Schwieterman, E., Stark, C., Wolf, E. T., Youngblood, A. (2019). The Sun-like Stars Opportunity. *Bulletin of the American Astronomical Society.*

Invited talks

- Detecting Biospheres and the Habitable Zone - Uncertainties Abound, (2019). *UC Santa Cruz Astronomy and Astrophysics Department*, Santa Cruz, CA.

- Life is Present but Not Detectable: The Productivity of Oxygenic Photosynthesis Around Cool M Dwarf Stars, (2019). *Sagan Summer Workshop*, Pasadena, CA.

Conference talks

- Atmospheric CO_2 Levels from 2.7 Billion Years Ago Using Micrometeorite Oxidation, (2019). *Goldschmidt*, Barcelona, Spain.

- Atmospheric CO_2 Levels from 2.7 Billion Years Ago Using Micrometeorite Oxidation, (2019). *AbSciCon*, Bellevue, WA.

- The Productivity of Oxygenic Photosynthesis Around Cool Stars, (2018). *LPSC*, The Woodlands, TX.

- Early hydrodynamic escape limits rocky planets to ∼1.6 Earth radii, (2017). *AbSciCon*, Mesa, AZ.